Sensitivity Enhancement in Micro-electromechanical Systems for Sensor Applications

Ross Turnbull, Linacre College

University of Oxford

Trinity Term, 2010

Supervised by Dr Steve Collins

This thesis is submitted to the Department of Engineering Science, University of Oxford, in fulfillment of requirements for the degree of Doctor of Philosophy.

Abstract

Micro-mechanical sensors are typically fabricated both in large numbers and economically using the photolithographic processes that were originally developed in the integrated circuit industry. The magnitude of a change in resonant frequency of a micro-mechanical structure can be used to quantify a change in mass of such a device. Hence, when packaged with integrated measurement, actuation and control electronics, it is possible to deliver a low-cost and small system in a package using fabrication techniques that are both mature and widely available. A micro-mechanical resonator has been designed for this project and samples of the prototype resonator were used to investigate various methods for detecting a change in resonant frequency using discrete electronic components. The system that has been designed can eventually be integrated with a small micro-mechanical structure to create a mass sensor. Resonators have been fabricated at QinetiQ as part of the Europractice Foundry Access Program and characterisation of typical devices is described in this thesis.

A popular method for controlling the behaviour of resonant micro-mechanical sensors is a force feedback technique designed to increase the effective quality factor of the resonant system. In this thesis, an increase in the effective quality factor of the prototype system has been demonstrated. When the resonator operates in air at atmospheric pressure, an improvement in the effective quality factor of two orders of magnitude was achievable. This meant that it was possible to assess the potential benefits offered by the force feedback technique by testing the various detection schemes that have been implemented at the natural quality factor and also at a high effective quality factor. A prototype control system has been built using simple digital electronics, a key component of which is a direct digital frequency synthesis chip used to provide a stable and accurate driving frequency. Methods for determining a change in the resonant frequency of a micro-mechanical resonator using this control system have been investigated. A method has been developed for determining the magnitude of a shift in resonance when the frequency of the excitation force is fixed. This thesis contains a description of the technique and also results demonstrating the corresponding detection capability of the prototype sensor.

Acknowledgements

People

Steve Collins, Marko Bacic, Sunay Shah, Bhaskar Choubey, Chenchen Deng, Mike Ward, Carl Anthony, Xueyong Wei, Nor Saad, Simon Pyatt, David Lowe, Gabriele Migliorini, Michel Randrianandrasana, Rita Gupta, Richard Gaskell, Jez Bowles, Anthony Cooper, Pete Hastings, Paul Pattinson, Christopher Rabson, Gerald Morgan, Paul Tidy, other friends and my family all helped me to realise my doctorate.

Thank you to Marko, for the valuable guidance, encouragement and inspiration during the final year of my undergraduate degree and subsequent application for study at DPhil level. Without this support and confidence, my doctorate would not have been possible. Thank you also to Bhaskar for the humour, advice and wide-ranging technical input that has assisted me in every aspect of my research and personal development. Above all, I would like to thank Steve for his supervision, expertise, guidance, accessibility and his continuing patience with my impatience. My time in his research group has been both pleasurable and productive.

Sponsors

Thank you to the Engineering and Physical Sciences Research Council for funding my DPhil and to the Defence Science and Technology Laboratory for additional funding for equipment. I would also like to thank the University of Oxford for employing me during the final stages of my DPhil and to Marko Bacic for writing letters of reference.

Once again I must especially thank Steve Collins, Mike Ward and David Lowe, who together successfully applied for funding from the Engineering and Physical Sciences Research Council. This grant paid for equipment, foundry access via the Europractice IC Service and for my participation in two international conferences.

Publications

Publications arising from this work:

- C. Anthony, R. Turnbull, M. Ward, and S. Collins. A mems resonator with linear differential drive. *Proceedings of the 19th Micro-Mechanics Europe Workshop (MME 2008)*, 2008

- R. Turnbull, M. Ward, S. Collins, and C. Anthony. A simple technique to increase the quality factor of micro-mechanical resonators. *Micro- and Nanotechnology Sensors, Systems, and Applications*, 7318(1):73181G, 2009

- C. Anthony, R. Turnbull, X. Wei, M. Ward, and S. Collins. Fabrication and quality factor control of a microelectromechanical system resonator with linear differential drive. *IET Science, Measurement & Technology*, pages 206–213, 2010

- C. Deng, R. Turnbull, C. Anthony, M. Ward, and S. Collins. A non-linear resonator for sensing applications. *Proceedings of Eurosensors XXIV*, 2010 (accepted)

- B. Choubey, C. Anthony, N. Saad, M. Ward, R. Turnbull, and S. Collins. Characterization of coupled micro/nano resonators using inverse eigenvalue analysis. *Applied Physics Letters*, 2010 (accepted)

- B. Choubey, M. Ward, C. Anthony, R. Turnbull, and S. Collins. On inverse eigenvalue analysis and characterisation of coupled micro/nano resonators. *The 9th Annual IEEE Conference on Sensors*, 2010 (submitted)

- R. Turnbull, M. Ward, C. Anthony, and S. Collins. Detection of changes in the resonant frequency of a mems resonator using a dds-based system. *IET Science, Measurement & Technology*, 2010 (submitted)

Additional publications related to this work are listed below. These publications contain results obtained using the printed circuit board designed for testing micro-mechanical devices, described in this thesis:

- N. Saad, X. Wei, C. Anthony, H. Ostadi, R. Al-Dadah, and M. Ward. Impact of manufacturing variation on the performance of coupled micro resonator array for mass detection sensor. *Procedia Chemistry*, 1(1):831–834, 2009

- X. Wei, M. Ward, C. Anthony, and D. Lowe. A preliminary study of a nonlinear micro vibro-impact system impact. *35th International Conference on Micro & Nano Engineering (MNE)*, 2010 (accepted)

Contents

List of Figures

List of Tables

Chapter 1

Micro-mechanical resonant sensors

1.1 Introduction to micro-mechanical systems

In 1959 the American physicist Richard Feynman delivered a lecture at the annual meeting of the American Physical Society entitled 'There's plenty of room at the bottom' [10]. In this classic talk, Feynman highlighted that very little work had been done in the field of miniaturisation. Whilst it was possible in 1959 to fabricate an electric motor that was the size of a fingernail, Feynman realised that common manufacturing processes such as writing, drilling, moulding or cutting could be attempted on an even smaller scale. Everything theoretically could be miniaturised, yet Feynman could see no physical reason why there had not been further progress, concluding that mankind had not 'yet gotten around to it'. Feynman's lecture, considered by many to be the first in the field of micro-technology, opened the door to a new field in which there has since been a great deal of work.

One success in the field of miniaturisation has been the emergence of Micro Electro Mechanical Systems (MEMS) [11]. MEMS technology exploits modern fabrication techniques in order to manufacture mechanical structures, sensors and actuators with feature sizes ranging from a millimetre in size down to a micrometre. In addition, Nano Electro Mechanical Systems (NEMS) can also be manufactured with feature sizes approaching the nanometre scale [12]. The first application of MEMS technology came with the birth of the Resonant Gate Transistor in 1967, in which an oscillating micro-cantilever was the key component [13]. However it was not until the 1980's when ink-jet printing companies and then automobile manufacturers (keen to develop airbag-deployment systems), saw the advantages of silicon micro-mechanics [14]. These developments were the first major application of MEMS technology and the market has since grown considerably with current applications in the aerospace, medical, automotive, military and consumer electronics industries [15–17]. As the photolithographic and other processes used to manufacture MEMS devices are similar to those used in the Integrated Circuit (IC) industry, sophisticated devices can be manufactured in MEMS foundries in high volume and at low cost. Consequently the technology has become increasingly available and attractive to a wide market.

1.2 Resonant sensors

Various chemical or physical phenomena can be detected by monitoring the resonant frequency of a MEMS mass-spring-damper system. When the micro-mechanical mass is coated with a receptive layer, such a system can be used as the key component in a sensor capable of detecting a specific measurand. For example, a change in relative humidity and the presence of mercury vapour have both been detected by measuring the corresponding change in resonant frequency of a MEMS resonator [18]. There is also increasing interest in employing micro-machined technology for use as biological sensors [19, 20]. Since MEMS devices can be combined with control electronics and packaged together, it is possible to create a cheap, mass-producible and compact sensor.

To describe the behaviour of a MEMS mass sensor, a device is modelled as a simple mass-spring-damper system, with equation of motion

$$\ddot{x} + \frac{c}{m}\dot{x} + \frac{k}{m}x = \frac{F_0}{m}e^{j\omega t}, \tag{1.1}$$

where x is displacement, m is mass, F_0 is the driving force, c and k are the damping and spring constants respectively [21]. The resonant frequency, Quality Factor (Q) and normalised driving force are then respectively defined as

$$\omega_0 = \sqrt{\frac{k}{m}}, \tag{1.2}$$

$$Q = \frac{m\omega_0}{c}, \tag{1.3}$$

$$F_D = \frac{F_0}{m}, \tag{1.4}$$

hence

$$\ddot{x} + \frac{\omega_0}{Q}\dot{x} + {\omega_0}^2 x = F_D e^{j\omega t}. \tag{1.5}$$

When a measurand binds to the surface of the MEMS structure, the mass (m) increases by Δm and the corresponding change in resonant frequency from ω_0 is $\Delta\omega_0$

$$\frac{\Delta\omega_0}{\omega_0} \approx -\frac{\Delta m}{2m}. \tag{1.6}$$

Equation (1.6) shows that to a first approximation, the percentage change in resonant frequency is therefore approximately equal to half of the percentage change in mass.

To detect a change in sensor mass by monitoring the resonant frequency, it must be possible to excite the mass-spring-damper system and detect the resulting movement. A simple method of generating driving signals for actuation of devices, with a controllable and stable frequency is therefore desirable. To achieve this, it is sensible to exploit the flexibility and low-cost of Direct Digital Synthesis (DDS) systems [22–24]. Furthermore, as DDS systems can be fabricated using microelectronics, it is possible to build a sensor comprising a MEMS resonant device packaged together with integrated DDS-based control electronics and readout electronics.

Common methods for actuation and readout of MEMS devices include electromagnetic, ohmic heating, optical, piezoelectric and electrostatic techniques [25]. The electromagnetic interaction in magnetic MEMS is usually based upon micro-coils or micro-permanent magnets [26]. However, to generate useful field strengths high currents are typically needed. Furthermore, the construction of micro-coils or micro-permanent magnets from large permanent magnets is time consuming, expensive and can not be manufactured using a standard foundry process.

A scheme based upon thermal expansion of an ohmically heated beam is an alternative method for actuation of MEMS devices. This technique is particularly useful if the development of a large force is a more significant concern than power consumption or operating frequency, which is typically limited to a few kHz [27]. Instead of ohmic heating, a laser beam can be used to cause a thermal expansion in the micro-cantilever, however an optical system such as this can not be easily fabricated in microelectronics and contained in an IC package [28].

Piezoelectric and electrostatic techniques for excitation of MEMS devices are suitable for creating a system that can be easily packaged, however the processing required to fabricate a piezoelectric actuator is typically the most complicated of the two methods [29]. It is important that the techniques developed for monitoring MEMS devices are compatible with the structures that can be produced at a typical MEMS foundry. However, designs based upon piezoelectric techniques are not compatible with the fabrication processes available, for example, at QinetiQ as part of the Europractice Foundry Access Program. Consequently, the design of the prototype resonator for this investigation is based upon electrostatic actuation and measurement.

Using electrostatic actuation and readout will enable the production of a sensor that is easy to package, does not consume a significant amount of power and can be fabricated at typical MEMS foundries. The corresponding control electronics must also be contained in the same IC package, however an integrated circuit typically takes approximately one year to design, fabricate and test. Since a high cost and risk is therefore associated with fabricating a prototype electronic control system in microelectronics, electronic circuits were constructed using discrete components. Despite this, the prototype drive, readout and control architectures that have been implemented, could be translated into a microelectronic design.

1.3 Fabrication process

Whilst the IC industry typically fabricates low-profile electronic devices, the MEMS industry is interested in three-dimensional movable structures. To produce such devices, two primary processes, either surface micro-machining or bulk micro-machining can be used. During a surface micro-machining process, device features are realised by depositing material layer by layer upon the surface of a substrate and selectively etching different layers. The substrate itself does not form part of the micro-machined device and silicon, glass or plastic can all be used as the substrate material [11].

Unlike surface micro-machining, when a bulk micro-machining process is used device features are formed in the substrate, which is typically silicon. Recently a method known as the Bosch Deep Reactive Ion Etch (DRIE) process has been developed which is a now a popular technique for bulk micro-machining [30–35]. For this project, devices were fabricated using the Integram Silicon-On-Insulator (SOI) High Aspect Ratio Micro-machining (HARM) process (an implementation of the Bosch process), available at QinetiQ on a multi-project wafer run provided as part of the Europractice Foundry Access Program of the European Commission. The minimum feature size for this process is 3μm and the minimum distance between neighbouring features is also 3μm.

Figure 1.1 shows a schematic diagram of a silicon substrate with a thin ($\sim 1\mu$m) layer of silicon dioxide on the surface. A further 20μm layer of silicon has also been grown upon the oxide. To define structures in this thin top layer of silicon, the HARM process cycles between etch and polymer deposition steps. Fluorine-based plasma chemistry is used to etch the silicon, using sulphur hexafluoride (SF_6) to provide fluorine for etching. A mask is used

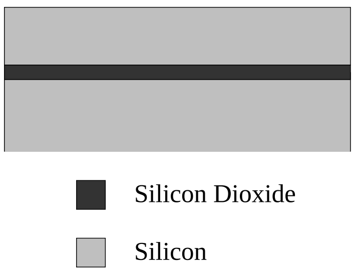

Figure 1.1: A silicon substrate with layers of silicon dioxide and silicon deposited upon the surface.

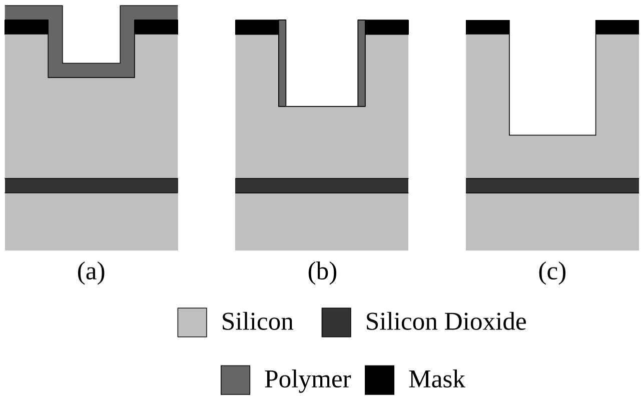

Figure 1.2: Deep vertical etching using the Bosch process.

to resist the etch process, thus defining features in the silicon which are defined by the mask layout. During each cycle, material is removed from the top layer of silicon, however polymer deposition steps are used to control the lateral etch, creating a deep vertical profile through the top layer of silicon.

During the polymer deposition step, a polymer, octofluorocyclobutane (c-C_4F_8), breaks to form radicals such as CF_2 which deposit on the sample. Figure 1.2a shows a partially-etched structure coated in this polymer. The polymer coats the entire sample, however during the etch process the polymer is removed far quicker in the vertical direction than on the side walls. This protects the side wall from the etch process and controls the lateral etch. Figure 1.2b shows the small amount of polymer remaining on the side walls during an etch cycle. In Figure 1.2c, the side walls have been exposed and the etch is halted to avoid removing material from the side walls. A new layer of polymer is then deposited before etching recommences.

Successive etch and polymer deposition steps are used to create a deep vertical etch through the entire surface layer of silicon until the thin layer of silicon dioxide is reached (which is resistant to the SF_6 plasma) and the etch process stops. Movable structures are released by using HF in a wet etch process to attack the oxide, which is gradually removed by the acid, undercutting the silicon above. Large areas of oxide require a longer etch than a small area, hence small structures can be released while larger areas remain attached to the substrate. This behaviour is exploited in order to anchor structures to the bulk substrate.

1.4 System response

When a MEMS resonator is moving, variations in the amplitude or phase of vibration can be used to detect a change in the characteristics of the resonant system [36, 37]. To calculate the magnitude and phase response of a mass-spring-damper system, the transfer function is obtained from the equation of motion (Equation (1.5)) describing the system

$$G(j\omega) = \frac{X}{F_D} = \frac{1}{{\omega_0}^2 - \omega^2 + \frac{j\omega\omega_0}{Q}}, \tag{1.7}$$

where X is the amplitude of the displacement. The magnitude and phase are

$$|G| = \frac{1}{\sqrt{({\omega_0}^2 - \omega^2)^2 + (\frac{\omega\omega_0}{Q})^2}}, \tag{1.8}$$

$$\angle G = \phi = -\arctan\left(\frac{\alpha}{Q(1-\alpha^2)}\right), \tag{1.9}$$

where α is defined as the frequency ratio $\frac{\omega}{\omega_0}$. Equations (1.8) and (1.9) show that the behaviour of the system is determined by the value of the resonant frequency and also the Q. Recall from

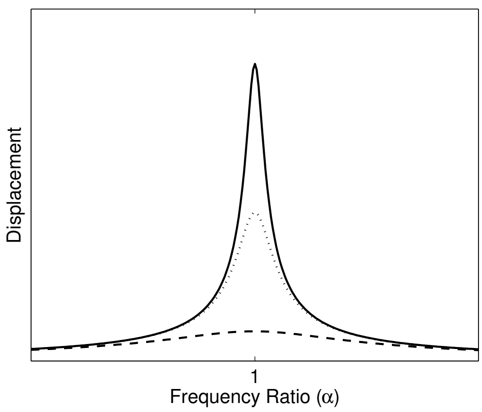

Figure 1.3: Amplitude response at high (dashed), medium (dotted) and low (solid) damping levels.

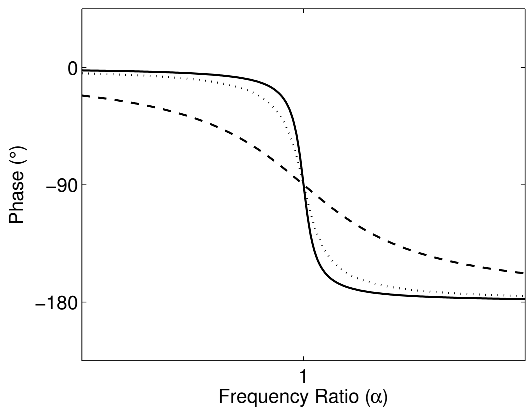

Figure 1.4: Phase response at high (dashed), medium (dotted) and low (solid) damping levels.

Equation (1.3) that the quality factor of a resonant system is determined by the damping level. Figure 1.3 shows the solution of Equation (1.8) over a wide range of driving frequencies (ω) and at various values of Q. In a high-Q system, the energy losses through damping are low and a narrow response with a clear peak is seen. In a lower-Q system, energy losses through damping are more significant, reducing the magnitude of the output and broadening the peak. Figure 1.4 shows the corresponding phase responses. Low values of quality factor result in a wide linear region of phase change around the natural frequency, whereas at high-Q the phase changes very quickly and rapidly saturates at zero or -180°.

1.5 Mass detection

1.5.1 Amplitude response

When a measurand binds to a functionalised resonant sensor, the resulting change in mass of the system causes a change in its resonant frequency. If the frequency of the driving force remains constant at, for example, the original resonant frequency of the system then the change in mass leads to a reduction in the amplitude of vibration. Since the amplitude response is at a maximum at the resonant frequency, the rate of change of amplitude with respect to frequency is zero. This results in a small change in amplitude after a small increase in mass. To operate in the region of highest sensitivity, the driving frequency should ideally correspond to the section of the resonant peak where the gradient is largest [36]. This occurs when the driving frequency is

$$\omega \approx \omega_0 \left(1 \pm \frac{1}{\sqrt{8}Q}\right), \tag{1.10}$$

where the slope is approximately

$$\frac{dX}{d\omega} = \pm \frac{4}{3\sqrt{3}} \frac{QX}{\omega_0} \approx \pm \frac{F_0 Q^2}{k\omega_0}. \tag{1.11}$$

Equation (1.11) shows that the rate of change of amplitude with respect to frequency is critically dependent upon the value of the system quality factor. Therefore to maximise the detection resolution of a system that monitors the amplitude of vibration, ideally the Q should be large. A significant problem with this technique, however, is that the required driving frequency is different to the resonant frequency. A method for automatically determining the frequency where the slope of the resonant peak is a maximum is therefore necessary.

1.5.2 Phase response

Alternatively, instead of monitoring the amplitude of vibration, measuring changes in the phase of a resonator's displacement can also be used to identify any change in its resonant frequency. The phase of a resonant sensor with respect to the driving force is shown in Figure 1.5. The key feature of the response is that at the resonant frequency (α =1), the phase angle is a constant value of -90°. This is independent of the value of the quality factor, driving force or the spring constant. Similarly, because velocity leads displacement by 90°, if the motion

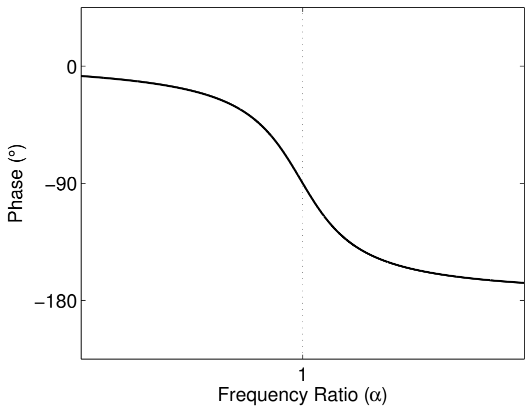

Figure 1.5: Phase difference between displacement and driving force for a mass-spring-damper system as a function of the frequency ratio (α).

sensor measures the velocity then the phase difference at the resonant frequency will always be 0°. This makes a detection scheme based upon monitoring phase particularly attractive as simple electronics such as a Phase-Locked Loop (PLL) can be used to identify the resonant frequency. After an increase in mass occurs due to the presence of a measurand, the change in the resonant frequency can then be tracked.

Alternatively, the phase of the resonator's displacement or velocity could be measured. Figure 1.5 shows that the maximum rate of change of phase occurs at the resonant frequency. As the rate of change of phase angle (ϕ) around resonance is approximately linear with respect a change in driving frequency (ω)

$$\frac{d\phi}{d\omega} \approx -\frac{2Q}{\omega_0}, \tag{1.12}$$

when combined with Equation (1.6), Equation (1.12) can be used to quantify any increase in mass (Δm) of the micro-mechanical structure

$$\Delta\phi \approx Q\frac{\Delta m}{m}. \tag{1.13}$$

Equation (1.13) shows that to ensure that a small percentage change in mass causes a significant change in phase of vibration, the Q of the system should ideally be large. Therefore the detection resolution of a mass sensor monitored by measuring either amplitude or phase is improved by increasing the Q of the system. Monitoring the phase, however, offers numerous benefits over monitoring amplitude. Primarily, the phase difference between the driving force and the displacement (or velocity) at the resonant frequency is fixed and is independent of the Q-value, or other system parameters. In addition, the maximum rate of change of phase occurs around resonance and the sensitivity of the resonant sensor is therefore maximised when driven at this frequency.

1.6 Quality factor control

1.6.1 Background

To monitor the resonant frequency of a sensor by measuring the phase of the displacement or velocity, a large quality factor is required in order to improve the detection resolution. Since the Q is inversely proportional to the damping present in the system (Equation (1.3)), a low damping level is desirable. In practice, detecting a change in resonant frequency is often limited by the inherently low Q observed in micro-mechanical systems. This is because a MEMS structure is generally subject to high viscous damping effects due to the surrounding gas (or liquid) that is necessarily present in a chemical or biological sensor application [38, 39]. In a vacuum where such effects do not exist, the Q-value is far higher. Consequently, a technique designed to increase the Q artificially to approaching the levels observed in a vacuum is desirable. The simplest conceptual method of increasing the Q is to directly cancel the large damping force by providing an external feedback force proportional to the velocity of the resonator.

1.6.2 Velocity feedback

Since the quality factor of a resonant system is inversely proportional to the damping level, the effective Q can be modified by generating a feedback force proportional to the instantaneous velocity of the moving structure. This can be modelled by modifying the equation of motion (Equation (1.5)) describing a simple mass-spring-damper system as follows,

$$\ddot{x} + \frac{\omega_0}{Q}\dot{x} + {\omega_0}^2 x = F_D e^{j\omega t} \pm \lambda \frac{\omega_0}{Q}\dot{x}, \tag{1.14}$$

where λ is the feedback fraction. The modified transfer function is $\hat{G}\left(j\omega\right)$

$$\hat{G}\left(j\omega\right) = \frac{1}{{\omega_0}^2 - \omega^2 + \frac{j\omega\omega_0}{\hat{Q}}}, \tag{1.15}$$

where the effective quality factor is $\hat{Q} = \frac{1}{1 \mp \lambda}$. To increase $\hat{Q}$, the feedback force is summed with the primary driving force. When $0 < \lambda < 1$ the effective quality factor is given by

$$\hat{Q} = \frac{1}{1 - \lambda}. \tag{1.16}$$

Equation (1.16) shows that when $\lambda \rightarrow 1$, $\hat{Q}$ increases rapidly. Furthermore, when $\lambda > 1$, the natural damping force is completely cancelled and energy is continually added to the system, resulting in a self-sustained oscillation. Consequently, careful control of the feedback fraction is essential due to the rapid increase in quality factor as the feedback fraction approaches one.

1.6.3 Previous work

Mertz, Tamayo and Nguyen have previously implemented velocity feedback (Q-control) to modify the Q of a micromechanical device. Mertz implemented the technique to vary the Q of a MEMS micro-cantilever for use in Atomic Force Microscopy (AFM) [28]. To drive the system, a laser beam was used to cause a thermal expansion in the micro-cantilever and the magnitude of the resulting force was a linear function of the intensity of the laser. The optical readout technique delivered a measure of the displacement of the resonator, as required for AFM. For Q-control, a force proportional to velocity is required, hence the displacement signal was differentiated to obtain a velocity-dependent signal. A similar technique was also employed by Tamayo [40, 41]. Tamayo used magnetic excitation and optical detection to measure the instantaneous displacement of the cantilever. The measured displacement signal was then phase shifted by 90° and amplified to generate the feedback force.

Another method used to increase the Q of a MEMS sensor has also been described by Tamayo [42]. The approach is based upon a digital implementation of the force-feedback technique described in section 1.6.2. The signal from an optical displacement detector was sampled using an Analogue-to-Digital Converter (ADC). A single driving signal was then generated in software and the amplitude controlled such that it was always equal to the output resulting from analogue electronics under the action of Q-control. A significant disadvantage of this approach is the requirement of a Personal Computer (PC) to perform the Fast Fourier Transform (FFT) for calculating the amplitude and phase of the sampled displacement signal.

An electrostatic feedback technique for implementing Q-control was implemented by Nguyen [43, 44]. A three-port comb structure was used, the first of which was for excitation of the resonator. To generate a velocity-dependent feedback voltage, the output current from a second port, which was proportional to the velocity of the moving structure, was converted into a voltage using a transimpedance amplifier circuit. The resulting voltage was then applied to the remaining electrode, generating a feedback force that was proportional to velocity and increasing the Q of the resonant system. Modifying the quality factor of a resonant system using this technique is appealing due to the simplicity of the feedback loop.

Any electronics designed to increase the effective Q of a resonant MEMS sensor should ideally be as simple as possible. Mertz and Tamayo used electronics to generate a velocity-dependent signal from the measured displacement, which complicate the feedback loop. However Nguyen measured the velocity directly, which facilitated a simple feedback loop without the requirement for any electronics. It is therefore desirable to build a readout system that measures velocity and not displacement. Similarly, an actuator with a linear voltage-force characteristic is desirable. This is because a velocity-dependent force must be generated from the velocity-dependent feedback voltage. If an actuator with a non-linear voltage-force characteristic were to be used, additional electronics would be required to compensate.

1.6.4 Noise considerations

In section 1.5.2 the benefits of detecting a change in mass of a MEMS sensor by observing the phase of the system were identified. In a system designed to measure the velocity of a moving resonator, the phase difference between the readout signal and the driving force at resonance is always 0°. As the phase difference is fixed, a PLL can be used to easily identify and track the resonant frequency. Alternatively, the phase of the system can be measured. The limit of detection of either of these approaches must be determined by the amount of phase noise present in the velocity-dependent output signal.

A study of the noise present in a mass-spring-damper system [45] was conducted by Tamayo. In the study, Tamayo shows that the phase noise of a resonator is proportional to $1/Q^{1/2}$ if the dominant noise source is thermal vibrations of the resonator, or $1/Q$ if noise in the motion sensor dominates. Therefore, due to this reduction in phase noise, the frequency stability of a closed-loop system designed to track the resonance using a PLL is expected to improve with increasing natural Q. Alternatively, when the phase is measured, the benefits of having a high natural Q are twofold. This is because in addition to reducing any noise present in the signal, a greater change in phase occurs for a given change in mass. Tamayo defines sensitivity as the ratio between $\frac{d\phi}{d\omega}$ and the phase noise, hence depending upon the source of the dominant noise the sensitivity is proportional to $Q^{3/2}$ or Q^2.

Tamayo also argues that when the Q is increased using velocity feedback, the sensitivity does not increase by the same amount as when the Q is naturally high. This is because the analysis shows that phase noise remains constant under the action of Q-control, suggesting that the only benefit will be an increase in sensitivity when measuring the phase. The increase in sensitivity will be determined by the ratio of $\frac{d\phi}{d\omega}$ before and after Q-enhancement. Practical considerations, however, often limit the absolute magnitude of the driving force. Tamayo's model shows that if the primary driving force is decreased when Q-control is implemented then the phase noise will increase. The conclusion of the study conducted by Tamayo is that due to the effect of noise, any benefit obtained by increasing the effective Q of a resonant system by velocity feedback could be reduced or eliminated.

1.7 Summary

In this chapter, the possibility of using a micro-mechanical mass-spring-damper system as a mass sensor has been described. Changes in the resonant frequency of such a mass sensor are often detected by monitoring amplitude or phase. Of these two approaches, phase detection offers more advantages. The most important benefit of phase detection is the fixed phase difference between the driving force and the resulting output signal when the system is resonating. This phase difference is either -90° or 0°, when monitoring displacement or velocity, respectively. In addition, the maximum rate of change of phase with respect to frequency occurs at the resonant frequency, maximising the signal observed after a small change in resonant frequency.

The damping forces present in a resonant system that forms the key component in a mass sensor play a critical role in determining the detection resolution of the overall sensor. Consequently increasing the Q of such a system is desirable. The simplest conceptual method for enhancing the Q is by the generation of a feedback force directly proportional to the velocity of the resonator. Such a force acts to cancel the instantaneous damping force acting on the moving structure and hence increases the effective Q of the system. Because a velocity signal is required to perform Q-enhancement, phase detection by monitoring velocity and not displacement should therefore be implemented. If the voltage-force characteristic of the actuator is linear, the only additional hardware required to implement Q-control is a simple electronic circuit to sum the velocity-dependent feedback voltage with the primary driving voltage. The possible benefit obtainable by increasing the effective Q can then be investigated without significantly complicating the electronic design.

It is desirable to build a prototype system that can eventually be optimised for manufacture in microelectronics. In addition to a linear drive and readout characteristic required to investigate the possible benefit gained by implementing Q-control, the architecture of the prototype resonator must be compatible with fabrication techniques commonly used in the microelectronics industry. Various common methods for actuation and readout of MEMS devices have been considered and an electrostatic technique was identified as the preferred technique for this investigation.

1.8 Thesis overview

The motivation for this thesis is to investigate various methods for determining the change in resonant frequency of a MEMS structure using discrete electronic components. Discrete electronics are used because of the high cost and risk associated with fabricating a prototype system using microelectronics. However, the readout and control architectures described in this thesis have been designed such that the system can be optimised for implementation in microelectronics. Hence the electronic design could then be packaged together with a MEMS device to create the hardware required for a mass sensor.

Using a simple feedback loop designed to amplify the measured velocity of a prototype resonator, it is possible to increase the effective Q of the resonant system. As the implementation of Q-control is conceptually simple, it is possible to do this without significantly complicating the electronic system. Consequently it will be feasible to operate schemes for determining the size of a change in resonant frequency at a higher effective Q than the natural Q and hence to investigate the benefits of Q-control.

Chapters 2 and 3 of this thesis contain a description of the design and characterisation, respectively, of a prototype MEMS resonator. The prototype resonator has been designed for use with discrete electronic drive and readout components. The resonator is relatively large however if the electronic design were to be implemented in microelectronics, a significantly smaller resonator could be used. Chapter 4 contains results showing the response of a typical resonator under the action of Q-control. The design of an automated system for determining and tracking the resonant frequency of a resonator is described in chapter 5. Chapter 6 contains results showing the performance of the system that has been designed and built, both when the resonant system operates at its natural quality factor and also when Q-control is implemented. In chapter 7, alternative methods for monitoring the resonant frequency of the prototype sensor are described. The techniques are based upon driving the resonator at a fixed driving frequency, even when the resonant frequency of the system changes. Finally, chapter 8 contains conclusions and a description of some areas of further work arising from this investigation.

Chapter 2

MEMS actuation and measurement

2.1 Introduction

A MEMS sensor should be easy to package and it must be possible to fabricate the mechanical structure using processes available at typical MEMS foundries. An architecture based upon capacitive actuation and readout is best suited to meet these requirements. By developing a system that uses capacitive actuation and readout in conjunction with simple discrete analogue and digital electronics, it is theoretically possible to eventually build a full sensor with integrated electronics in a single package, based upon the design of the discrete system.

To build a sensor with a good detection resolution, the mass of the sensor should be small. However, it must be possible to excite and detect movement of the prototype MEMS structure designed for this investigation using discrete electronic components and this will effectively limit its minimum size. An actuator with a linear voltage-force dependency and a readout system designed to deliver a voltage proportional to the resonator velocity should be implemented to facilitate Q-control. It will then be possible to investigate the potential benefit in artificially increasing the system Q on the overall sensitivity. In this chapter, the design of a resonator to meet these specifications and also the electronics required to detect motion are both described.

2.2 Actuation and measurement

2.2.1 Capacitive actuation

The electrostatic force between two plates, formed from a fixed driving port and a movable mechanical structure, is a function of both the applied voltage and the rate of change of capacitance with respect to displacement $\left(\frac{dC}{dx}\right)$,

$$F = \frac{V^2}{2}\frac{dC}{dx}. \tag{2.1}$$

This shows that the geometry of the capacitor used for actuation is critical in controlling the properties of the overall driving force experienced by the MEMS resonator. Figure 2.1 shows a parallel plate capacitor which is the simplest design for a drive capacitance. The fixed plate is connected to electrical ground and the movable plate is suspended on a flexible beam to form an initial gap (d) between the plates. The supporting beam is anchored to the underlying substrate at either end. The movable plate is also connected to the excitation voltage, V. For small displacements, $\frac{dC}{dx}$ is approximately

$$\frac{dC}{dx} \approx \frac{\epsilon_0 \epsilon_r A_p}{d^2}\left(1 + \frac{2x}{d}\right), \tag{2.2}$$

where A_p is the area of each plate, ϵ_0 and ϵ_r are the permittivity of free space and the relative permittivity, respectively. Equation (2.2) shows that $\frac{dC}{dx}$ is a linear function of the instantaneous displacement for small x. Therefore the resulting electrostatic force is a function of not only the applied voltage but also displacement. A more satisfactory arrangement yields an electrostatic force that is independent of displacement. This has been demonstrated previously

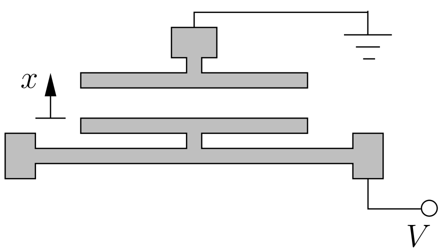

Figure 2.1: Parallel plate capacitor arrangement for actuation of a MEMS device.

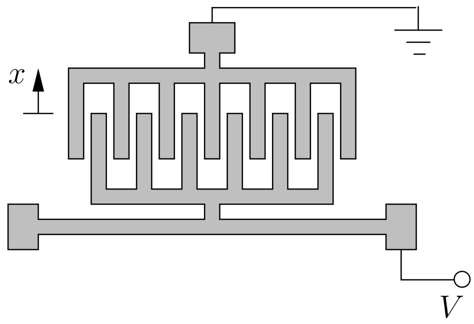

Figure 2.2: A MEMS comb structure.

by using an interdigitated finger (or comb) structure [46, 47].

Figure 2.2 shows a simple comb structure. The key feature of an electrostatic comb is that $\frac{dC}{dx}$ is ideally a constant. To demonstrate this, consider the capacitance formed between the fixed driving comb with n_f fingers and the movable comb, when the fingers initially overlap by a distance o,

$$C = \frac{n_f \epsilon_0 \epsilon_r t_h (x + o)}{g}. \tag{2.3}$$

In the equation above, t_h is the thickness of the structure and g is the gap between overlapping fingers which means that $\frac{dC}{dx} = \frac{n_f \epsilon_0 \epsilon_r t_h}{g}$. Consequently, the electrostatic drive force is linear with respect to the square of the applied voltage

$$F = V^2 \left(\frac{n_f \epsilon_0 \epsilon_r t_h}{2g} \right). \tag{2.4}$$

There are three logical configurations for generating the electrostatic force (Equation (2.1)) for excitation. In the first case the driving voltage is sinusoidal,

$$V = V_{AC} \cos(\omega t), \tag{2.5}$$

$$F = \frac{V^2}{2} \frac{dC}{dx} = \frac{V_{AC}^2}{2} \left(\frac{1 + \cos(2\omega t)}{2} \right) \frac{dC}{dx}. \tag{2.6}$$

The significant feature of this technique is that the resulting electrostatic force consists of a static component and a component at a frequency that is twice the frequency of the excitation voltage, hence this technique is referred to as *frequency doubling*. This technique is not compatible with the implementation of Q-control using a simple feedback technique, due to the non-linear relationship between voltage and the resulting force (in both magnitude and frequency). However, in an extension to this method, the driving voltage can also contain a DC component,

$$V = V_{DC} + V_{AC}\cos(\omega t), \tag{2.7}$$

$$F = \frac{1}{2}\left(\left(V_{DC}^2 + \frac{V_{AC}^2}{2}\right) + 2V_{AC}V_{DC}\cos(\omega t) + \frac{V_{AC}^2\cos(2\omega t)}{2}\right)\frac{dC}{dx}. \tag{2.8}$$

This approach, which is referred to as *direct drive*, is used by Nguyen to generate a driving force that is at the same frequency as the frequency of the applied voltage [43, 44]. A benefit of this technique (over frequency doubling) is that complicated electronics are not required to halve the frequency of the feedback signal used to enhance the Q. However, there is also a frequency component at twice the frequency of the excitation voltage and an undesirable static force. The relative contribution of the undesirable frequency component can be minimised by using a small AC driving component superimposed upon a large DC bias.

It is possible to cancel the undesirable terms by using two combs arranged in a push-pull configuration such that the fingers of each comb are in opposing directions [47]. When the voltage applied to one comb is $V_{DC} + V_{AC}$ and the voltage applied to the opposing comb is $V_{DC} - V_{AC}$ the overall electrostatic force experienced by the mechanical structure is

$$F = 2V_{AC}V_{DC}\cos(\omega t)\frac{dC}{dx}. \tag{2.9}$$

This technique, *differential drive*, is similar to direct drive in that the overall driving force is at the same frequency as the applied voltage, however one benefit is that the undesirable constant term and the term at twice the frequency of the driving voltage are removed by differential drive [1]. Hence a system designed with two opposing electrostatic combs, offers the maximum flexibility as it is possible to implement any of these schemes.

2.2.2 Capacitive readout

Various capacitive readout techniques could be employed to measure the movement of a MEMS resonator. Figure 2.3 shows one configuration, suggested by Ghavanini [48]. The

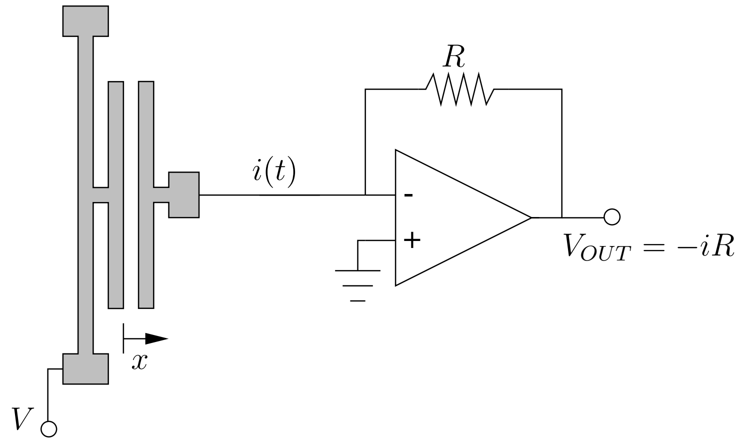

Figure 2.3: Simultaneous excitation and readout using a parallel plate capacitor.

technique uses the same parallel plate capacitor for both actuation and readout purposes. A voltage is applied to the resonant device, which itself is one plate of the parallel plate capacitance. The remaining plate of the capacitor is at zero volts and by observing the current delivered from the capacitor at this node, the movement of the structure can be measured. When the excitation voltage ($V = V_{AC}\cos(\omega t)$) is applied, the frequency of the resulting force is at twice the frequency of the driving voltage (from Equation (2.1)). Therefore the instantaneous displacement and capacitance are given by

$$x = X\cos(2\omega t + \phi), \tag{2.10}$$

$$C = \frac{\epsilon_0 \epsilon_r A_p}{d - X\cos(2\omega t + \phi)}, \tag{2.11}$$

where X is the amplitude and ϕ is the phase difference between the movement and driving force at ω. The current at the the readout node is given by

$$i(t) = V\frac{dC}{dt} + \frac{dV}{dt}C, \tag{2.12}$$

hence

$$i(t) = -\frac{\epsilon_0 \epsilon_r \omega V_{AC} A_p}{d - X\cos(2\omega t + \phi)}\left[\frac{X\sin(\omega t + \phi) + X\sin(3\omega t + \phi)}{d - X\cos(2\omega t + \phi)} + \sin(\omega t)\right]. \tag{2.13}$$

When X is much smaller than d, the third harmonic frequency in the output current can be written as

$$i(t) \approx -\frac{\epsilon_0 \epsilon_r A_p}{d} \frac{X}{d} \omega V_{AC} \sin(3\omega t + \phi), \tag{2.14}$$

which is proportional to the velocity of the moving plate. An attractive feature of this approach is that only one electrode is used for excitation as well as for detection, which is desirable for simple fabrication. A number of factors render this approach less attractive. Firstly, the linear relationship between current and velocity described in Equation (2.14) is an approximation which is only true at small displacements. At larger displacements the relationship becomes non-linear which is undesirable. Secondly, the output current is at a frequency that is three times higher than the frequency of oscillation of the device. This means that generating a feedback signal for Q-control, which must be at at the same frequency as the velocity, is complicated as a frequency divider must be incorporated into the feedback loop.

Figure 2.4 shows another simple configuration for capacitive readout which is described by Baxter [49]. This method requires two identical capacitors, driven with AC voltages. Simple analysis shows that the output is independent of the excitation frequency and is proportional to the difference in capacitance between them,

$$V_{OUT} = -V_{AC} \frac{C_1 - C_2}{C_f}. \tag{2.15}$$

Assuming that C_1 and C_2 are parallel plate capacitors, the resulting output signal using this

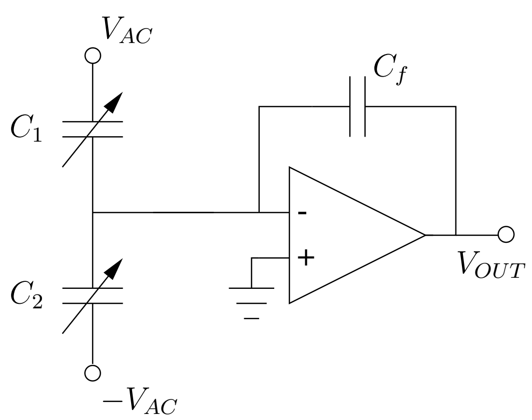

Figure 2.4: Capacitance bridge circuit.

readout configuration is linear only for small, static, displacements

$$V_{OUT} = -\frac{V_{AC}\epsilon_0\epsilon_r A_p}{C_f}\left[\frac{2x}{d^2 - x^2}\right]. \tag{2.16}$$

A similar op-amp based circuit has been suggested by Tang, which is not limited to small, static, displacements and delivers a measure of velocity as desired [47]. In this approach a DC bias voltage (V_s) is connected to one side of a comb capacitance and the other to electrical ground. The current developed at the readout capacitance is

$$i(t) = V_s\frac{dC}{dt} + \frac{dV_s}{dt}C = V_s\frac{dC}{dx}\frac{dx}{dt}. \tag{2.17}$$

A transimpedance amplifier can be used to convert the velocity-dependent current into a voltage and also to provide the DC bias voltage. Figure 2.5 shows this configuration.

Equation (2.17) shows that using this technique, the current delivered to the transimpedance amplifier is not affected by the presence of any undesirable static parasitic capacitances. Further, the output is not a function of the absolute value of C, because V_s is a DC voltage $\left(\frac{dV_s}{dt} = 0\right)$. If the readout capacitance is designed as an interdigitated comb structure, it is possible to take advantage of the linear relationship between capacitance and displacement to produce a current (and hence voltage) that is directly proportional to the velocity of the moving structure. The ability to measure the velocity of a resonator, using simple electronic components, with immunity to the magnitude of any fixed capacitances present, makes this approach for monitoring the movement of the sensor particularly attractive.

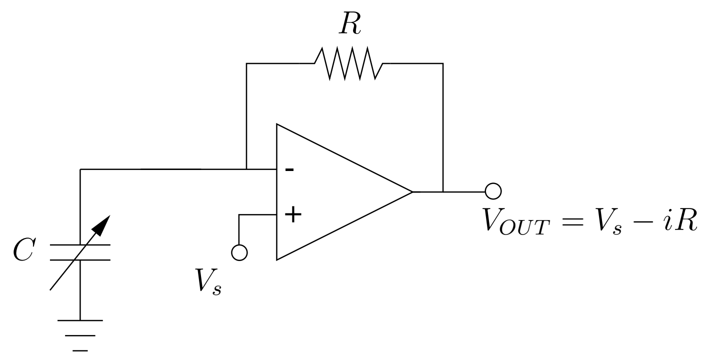

Figure 2.5: Readout capacitance and transimpedance amplifier configuration.

2.3 Resonator architecture

In sections 2.2.1 and 2.2.2 the advantages and disadvantages of various drive and readout architectures were discussed. In section 2.2.1 it was noted that differential drive, using interdigitated comb structures, offers the most benefits for excitation of a resonant sensor. In particular, the frequency of the resulting electrostatic force is the same frequency as the applied voltage. This is desirable for the construction of a feedback loop to increase the Q using simple electronic components.

In section 2.2.2, a number of methods of capacitive readout were considered. The most appropriate technique is the application of a DC voltage connected across a comb capacitance followed by current-to-voltage conversion of the resulting current, which is proportional to the resonator velocity. This method can be converted quite simply into a differential readout architecture which theoretically rejects any common mode interference present in the velocity signal. To do this a second readout comb capacitance orientated to oppose the direction of the first comb capacitance can be used. A second current-to-voltage conversion circuit yields a voltage proportional to the instantaneous velocity, 180° out of phase with the output of the primary channel. An instrumentation amplifier can be used to amplify the difference between the two voltages and to reject common-mode noise and interference.

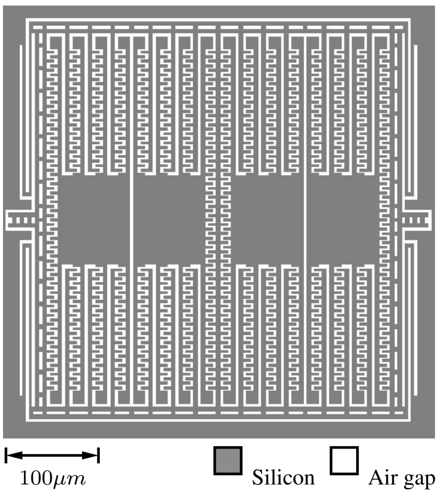

Figure 2.6: The proposed prototype structure layout, which can be used as a single element or the repeated element in a larger test structure.

Figure 2.6 shows the layout of a resonator with the required capacitances that has been designed by colleagues at Birmingham University. The device comprises four fixed comb

Table 2.1: Parameter values for estimate of output voltage when the resonator is moving in air at the natural frequency.

Parameter	Value	Units
k	25.4	Nm^{-1}
m	3.6	μg
f_0	13	kHz
$\frac{dC}{dx}$	13.4	$\mathrm{fF}\mu\mathrm{m}^{-1}$
Q	10	-

structures and a movable shuttle with combs attached to form capacitances with the fixed combs. The resonator is supported by four 3μm wide and 178μm long folded flexure springs at each corner and the thickness of the silicon membrane is 20μm. Electrical connections are made to four central bond pads and each pad is connected to one side of a set of opposing combs. It is possible to connect several prototype resonators. To facilitate this, a small stub is attached to each end of the movable frame to which a coupling spring can be attached. The resulting chain can then be used to investigate the behaviour of coupled resonators, however this is the subject of a separate investigation [5, 6].

Table 2.1 contains a summary of the key design parameters. When modelled using Comsol Multiphysics the overall stiffness of the prototype device was calculated to be 25.4Nm^{-1}. The mass is 3.6μg and eigen-mode analysis calculates the fundamental mode of the resonator to be approximately 13kHz. Estimated values for the capacitance and $\frac{dC}{dx}$ of each port are 250fF and 13.4$\mathrm{fF}\mu\mathrm{m}^{-1}$ respectively. The damping force a MEMS resonator experiences (usually a combination of squeeze film and slide film damping) is primarily determined by the geometry of the sensor and the ambient air pressure [50–54]. Colleagues at Birmingham University have investigated the primary sources of damping, concluding that squeeze film damping is the dominant source of damping. The estimated Q value at atmospheric pressure is approximately 10 [1].

[1]Calculations performed by colleagues at Birmingham University are given in appendix A.

2.4 Electronics

2.4.1 Drive electronics

The only requirement for the drive electronics is the ability to produce two signals, $V_{DC} \pm V_{AC}$. Figure 2.7 shows the simple electronic circuit formed from three OPA404 precision op-amps, used to generate the two drive signals. By supplying AC and DC voltages, the signals for differential driving are generated. Alternatively, if frequency doubling is required a DC bias of zero volts can be used and the driving signal taken from one of the two outputs of the circuit.

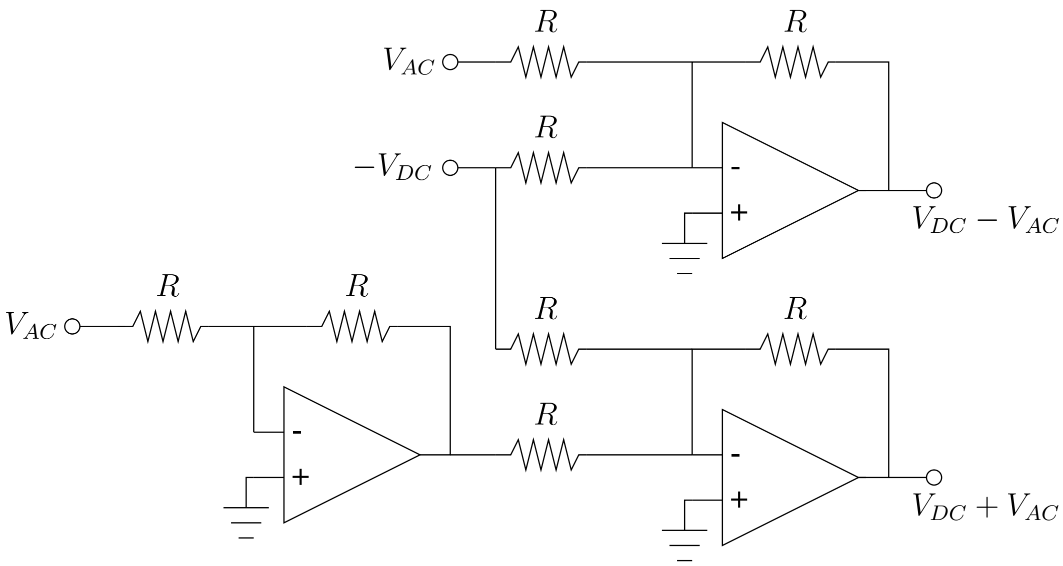

Figure 2.7: Simple electronic circuits required to generate driving signals.

2.4.2 Readout electronics

To test single resonators and chains of resonators coupled together, a Printed Circuit Board (PCB) with current-to-voltage conversion and amplification stages has been designed and manufactured. Figure 2.8 shows the electronics contained on the PCB for generating a velocity-dependent voltage. In section 2.3 it was suggested that two opposing comb capacitances, each biased to generate a current proportional to the instantaneous velocity of the resonator structure, can be used to implement a differential readout architecture. To convert the output currents into voltages for a differential readout architecture, two transimpedance amplifiers can be used followed by an instrumentation amplifier stage. The instrumentation amplifier removes

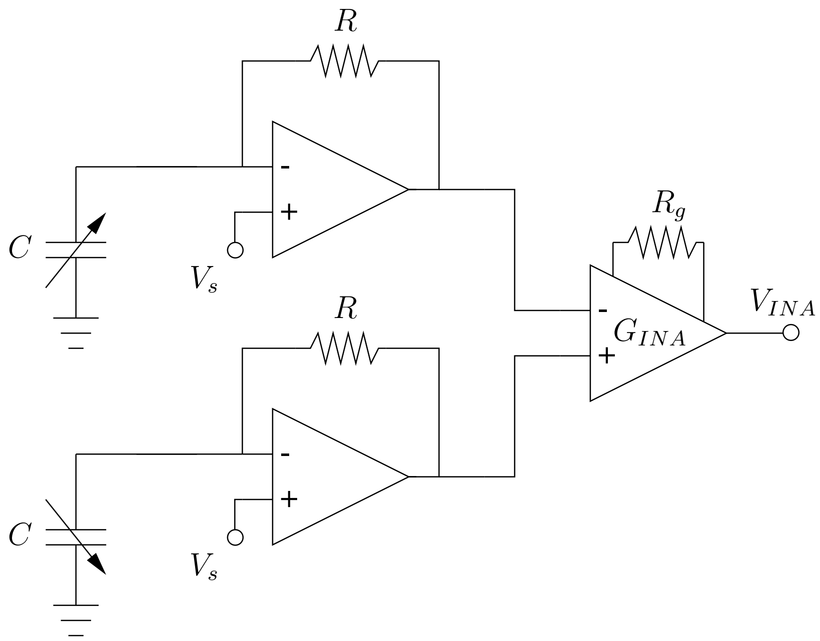

Figure 2.8: Differential readout architecture using two readout capacitances and two transimpedance amplifiers followed by an instrumentation amplifier stage (G_{INA}) with external gain control resistor (R_g).

the DC bias in the output voltage and also to provides a further gain stage. The output from the instrumentation amplifier is

$$V_{INA} = 2G_{INA}V_sR\frac{dC}{dx}\frac{dx}{dt}. \tag{2.18}$$

To estimate the output current from a readout comb capacitance and the overall output voltage from the instrumentation amplifier, the expected velocity at typical driving voltages is calculated. From Equation (1.8) the magnitude of the velocity at the resonant frequency is

$$\dot{X} = \frac{F_0Q}{\sqrt{mk}}. \tag{2.19}$$

The magnitude of the driving force when using differential drive is $F_0 = 2V_{AC}V_{DC}\frac{dC}{dx}$ and from Equation (2.17) the resulting current is

$$I = 2V_sV_{AC}V_{DC}\frac{Q}{\sqrt{mk}}\left(\frac{dC}{dx}\right)^2. \tag{2.20}$$

The voltage at the output of the instrumentation amplifier stage is given by substituting Equation (2.19) into Equation (2.18)

$$V_{INA} = 4G_{INA}V_sV_{AC}V_{DC}R\frac{Q}{\sqrt{mk}}\left(\frac{dC}{dx}\right)^2. \tag{2.21}$$

These expressions can be used to estimate the expected operating conditions of the MEMS resonator and the output from the test PCB, when the driving frequency is close to the resonant frequency of the device under test. Using values from Table 2.2 for typical maximum working voltages and amplifier gains, and values for physical constants from Table 2.1 gives a typical displacement of approximately 100nm. This corresponds to a peak current per channel of approximately 1nA and an output voltage from the instrumentation amplifier stage of 20mV$_{\text{rms}}$ when the resonator is operating at ambient pressure.

Table 2.2: Typical maximum voltages and amplifier gains for detecting motion of a resonator.

Parameter	Value	Units
G_{INA}	10	-
V_s	8	V
V_{AC}	5	V$_{\text{pp}}$
V_{DC}	5	V
R	1	MΩ

When the test resonator is placed in a vacuum, for characterisation at low pressure, the quality factor is expected to be several orders of magnitude higher than in air. Consequently, from Equations (2.21) and (2.19) the PCB output voltage and the displacement are expected to be larger than when the device moves in air. This is a potential problem as it is theoretically possible to damage the resonator by over excitation, causing a displacement large enough (approximately 5μm) to bring the finger ends of the moving combs into contact with the stationary combs. Therefore the driving voltage levels should be significantly lower than those used at atmospheric pressure, to ensure that the displacement does not exceed approximately 1μm.

2.4.3 PCB specifications

After manufacture, the silicon wafer containing resonators was diced and the resulting die fixed into the cavity of a 24-pin Dual-In-Line (DIL) header (CSB02488-024), manufactured by Spectrum Semiconductor Materials, Inc. Electrical connections were then made by wire bonding between the contact pads on the resonator and the header. Figure 2.9 shows a plan view of a section of the test PCB where the header is located. The header containing test

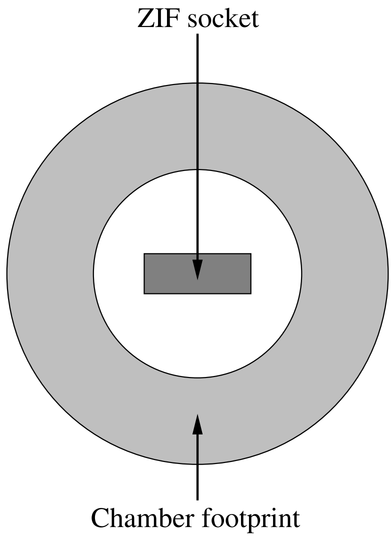

Figure 2.9: Plan view of a section of the test PCB, showing the ZIF socket and contact zone for vacuum test head.

devices is attached to the PCB with a Zero-Insertion-Force (ZIF) socket. Around the ZIF socket there is a clear annulus on the top layer of the board to allow a vacuum test head to be placed over the resonator chip for vacuum testing. The vacuum test chamber is formed from a Caburn MDC CF40D-KF-V flange with a bleed valve for pressure control and is sealed to the board using a rubber o-ring seal. The vacuum chamber is in turn linked to an Aidxen vacuum pump via a metal bellows hose and pressures down to 10mPa are obtainable. Figure 2.10 shows the arrangement of the vacuum chamber and the test PCB to form a vacuum chamber. Figure 2.11 shows a photograph of the PCB, which was manufactured by Würth Electronik GmbH.

In the previous section, analysis shows that the readout current is expected to be approximately 1nA. This current will be converted into a voltage using a transimpedance amplifier with a 1MΩ resistor in the feedback loop to a give a gain of 1mVnA^{-1}. This relationship is

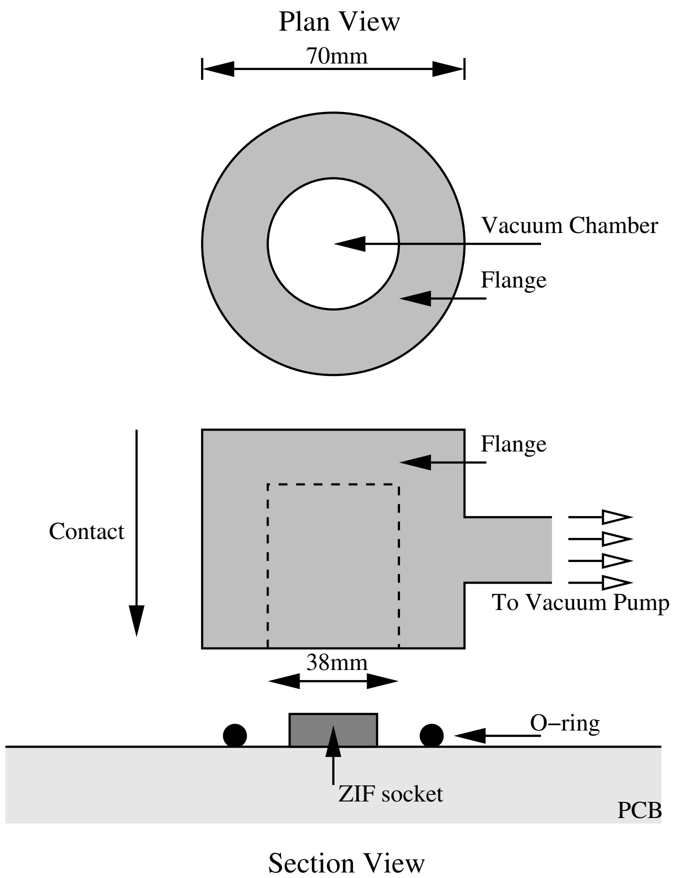

Figure 2.10: Arrangement of vacuum test chamber and PCB showing vacuum chamber encapsulating the test sample.

based upon the analysis of an ideal op-amp and one significant assumption is that both inputs to the op-amp draw zero current. To ensure that the model of the op-amp is valid it is important that the input bias current is significantly smaller than the current under conversion to a voltage, National Semiconductor LMC6084 op-amps which have an ultra low input bias current of 10fA are used. For the instrumentation amplifier stage, a general purpose AD620A with a programmable gain set with an external resistor has been chosen.

The PCB has 12 drive connections and 12 readout channels which means that it will be possible to differentially drive and readout six different single or coupled resonators contained in the same header. As the frequency of driving signals will be the same as the frequency of the readout signals when using differential driving, inputs and outputs are isolated to different sides of the PCB. This minimises crosstalk between drive signals and the readout electronics. Further, the top and bottom copper layers of the PCB are used to provide power rail voltages and are flooded to shield the two internal layers where drive and readout signals are routed.

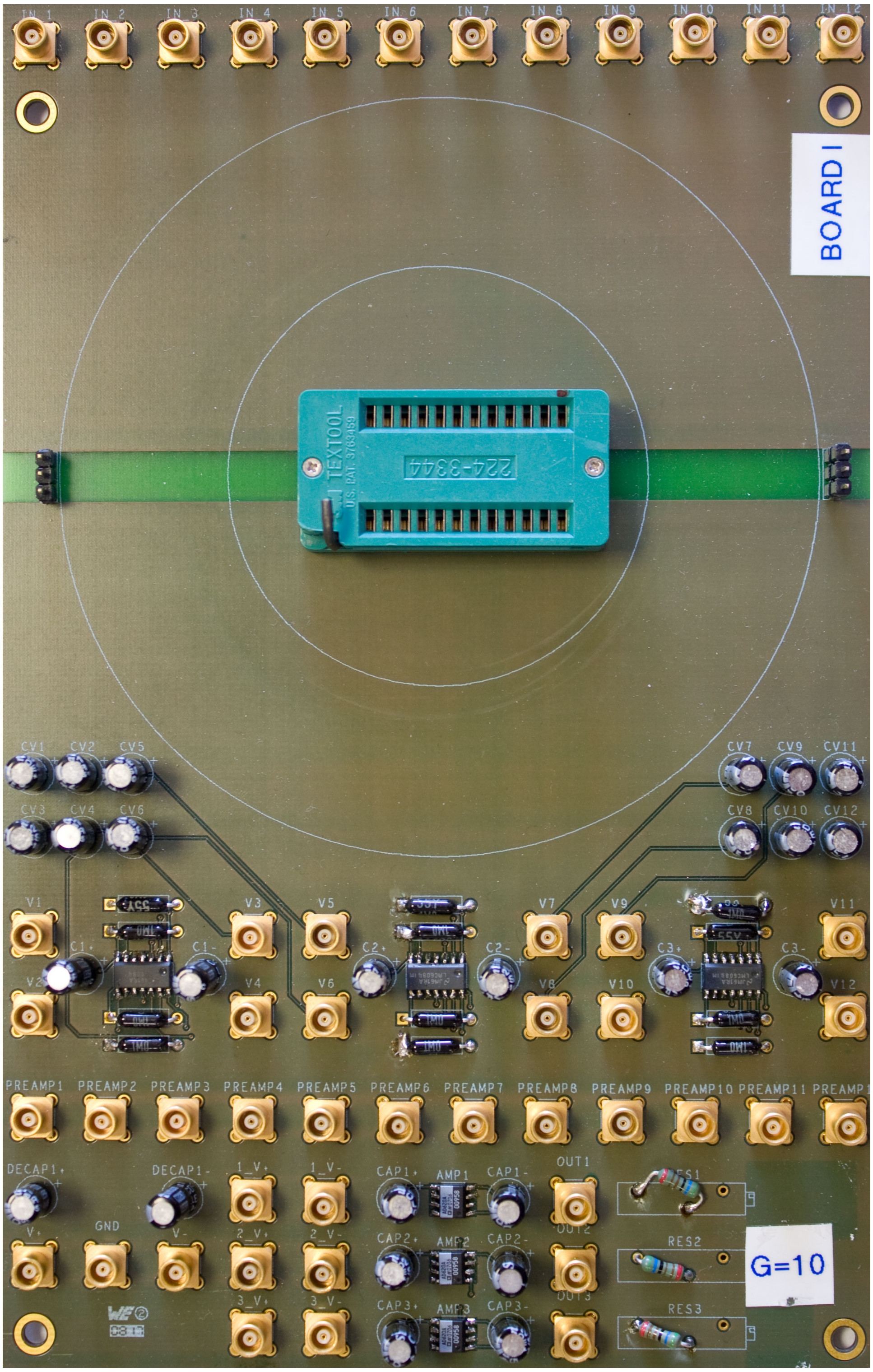

Figure 2.11: A photograph of the PCB manufactured for testing resonators.

2.4.4 PCB Characterisation

After population, the PCB was characterised to confirm that the design is suitable for testing the prototype resonator. To characterise the crosstalk between the input channels and output channels of the PCB, test voltages were applied to each input channel in turn. The transient response at the output of the instrumentation amplifier was recorded and processed in order to calculate the power at a test frequency of 10kHz. Tests were performed using a PC and a National Instruments PCI-6133 DAQ. The PCI-6133 DAQ has 14-bit ADC resolution and the Least Significant Bit (LSB) corresponds to approximately 150μV. Noise sources in the readout electronics result in a noise floor of approximately 10mV$_{\mathrm{pp}}$ at the output of the final amplification stage of the test PCB. This corresponds to a displacement of approximately 50nm. Because a displacement of only 100nm is expected when the resonator operates at atmospheric pressure, it will therefore be necessary to filter the output voltage from the PCB in order to recover the velocity-dependent signal when the resonator operates at this pressure.

Figure 2.12 shows the measured crosstalk signal level at the output of the PCB readout electronics, when a test signal is applied to an input channel. The figure shows that the measured crosstalk is proportional to the voltage of the applied test signal. When a test signal of 20V$_{\mathrm{pp}}$ is applied, the measured voltage at the output of the readout electronics is approximately 1mV, which is significantly smaller than the expected output voltage when resonators are tested. This shows that in this voltage range, the crosstalk signal will not interfere with the signal due to the movement of the MEMS structure.

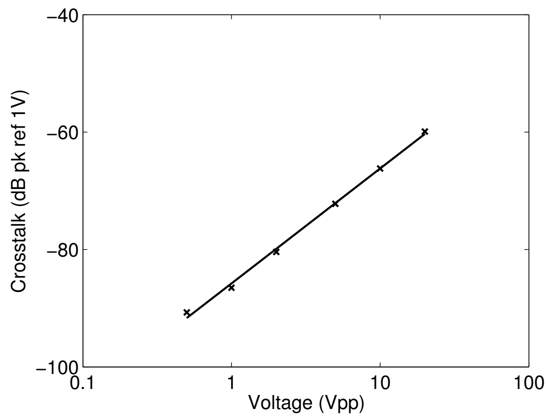

Figure 2.12: Measured output of the readout electronics at various input voltages.

2.5 Summary

In this chapter a prototype MEMS resonator with an electrostatic actuation and readout architecture has been described. Using an electrostatic actuator formed from two opposing MEMS comb drives creates a flexible driving architecture. The driving force that will be generated is linear with respect to the magnitude of the applied driving voltages. For monitoring the movement of the device, measuring the velocity is sensible as this facilitates a simple investigation into the possible benefits of implementing Q-control. To readout the velocity of the MEMS device, readout capacitances are formed from comb structures. When a DC bias voltage is applied across one of these comb capacitances a current proportional to the velocity of the resonator will be generated. This current can then be processed by simple analogue electronics to generate a voltage proportional to the velocity of the resonator.

A PCB has been designed and manufactured containing readout electronics and drive connections for testing single and coupled chains of MEMS resonators. On the PCB there are 12 drive connections and 12 independent readout channels. This means that six different resonators contained within the same header can be connected to the PCB using differential drive and readout. To readout the velocity of a resonator, a transimpedance amplifier is used to convert the current produced by a readout comb capacitance into a voltage. Two transimpedance amplifiers are used to form a differential readout channel. In addition to transimpedance amplifier stages, the PCB also contains the instrumentation amplifiers required to process the output of each transimpedance amplifier stage and produce a voltage proportional to the velocity of the resonator. Finally, to minimise crosstalk between drive and readout electronics, signals are separated to opposite sides of the PCB. Measurements show that using this arrangement, the observed crosstalk signal is insignificant in comparison to the expected output voltage when the resonator is moving in air at atmospheric pressure.

Chapter 3

Device characterisation

3.1 Introduction

In the previous chapter, a prototype resonator for investigating methods of detecting changes in resonant frequency of a MEMS sensor was described. The resonator was designed by colleagues at Birmingham University and fabricated by QinetiQ. A key feature of the resonator design is the use of interdigitated comb structures to create actuation and readout capacitances. The rate of change of capacitance with respect to displacement is ideally a constant for a comb structure. Because of this, the current generated by the readout comb capacitances will be proportional to the velocity of the moving micromechanical structure.

To test resonators, a PCB with readout electronics and connections for driving signals has been designed and manufactured. The electronic circuits on the PCB convert the velocity-dependent current generated by readout capacitances into a voltage. The prototype MEMS resonator has been fully characterised using this PCB to measure its velocity and results of these experiments are presented in this chapter. The following section contains a description of the manufactured prototype resonator. In the remainder of this chapter, results showing the amount of capacitive coupling between drive and readout ports are presented. Furthermore, results of the characterisation of the drive and readout architectures are also given. Finally, unexpected characteristics of the resonator are explained by modelling the manufactured resonant system.

3.2 Prototype resonator

Figure 3.1 shows a Scanning Electron Microscope (SEM) image of the prototype MEMS resonator that has been designed by Dr Carl Anthony at Birmingham University and manufactured by QinetiQ. The manufacturing variability associated with MEMS fabrication techniques is the subject of separate research by colleagues at Birmingham University. As part of that investigation, the resonator geometry was measured using an SEM and compared with design values. This revealed that, in addition to the expected sample-to-sample variability, the design is under-etched by approximately 250nm. This means that the manufactured mass of the resonator is larger than the design value. The mass of a typical resonator has been estimated to be 4μg, a 10% increase from the design value.

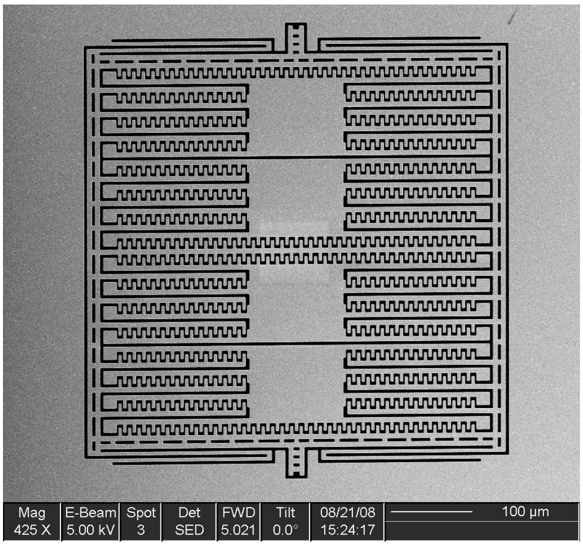

Figure 3.1: SEM image showing the MEMS resonator fabricated by QinetiQ and bond pads used for making electrical connections to the drive and readout electronics.

3.3 Feedthrough

In section 2.4.4, crosstalk between driving signals and readout electronics on the test PCB was characterised. Results showed that a small (1mV) signal was recorded when a driving voltage of $20V_{pp}$ was applied to a drive channel. The conclusion of the experiments described in section 2.4.4 is that the magnitude of any crosstalk signal between drive and readout channels on the PCB will be small in comparison to the expected velocity-dependent output signal.

When a header containing a resonator is installed on the PCB, driving signals and readout channels will be necessarily in very close proximity. This means that increased capacitive coupling between drive and readout channels is expected. In the remainder of this thesis, the effect of capacitive coupling between drive and readout channels when the prototype is in place on the PCB will be referred to as *feedthrough*. The effect of feedthrough will only be a significant problem if the frequency of the driving signals is the same as the frequency of readout signals. For example, when differential driving is used, both signals are at the same frequency and therefore could interfere with each other. Any feedthrough signal present should therefore be significantly smaller than the desired velocity-dependent signal.

Recall that when using differential drive to excite the resonator, the voltages applied to the driving combs are $V_{DC} \pm V_{AC}$. Using this approach, the feedthrough signal due to $+V_{AC}$ is theoretically partially cancelled by the feedthrough signal due to $-V_{AC}$. Moreover, the feedthrough signals will cancel completely if the coupling capacitances are identical. In practice this is not expected to be the case, due to the presence of bonding wires and also the close proximity between the innermost combs dominating the characteristics of the feedthrough signal.

The level of feedthrough present when the header containing a prototype MEMS resonator is fitted on the PCB was characterised. To measure the feedthrough level, the differential readout voltage was recorded when drive signals were applied to the test resonator. During this test, any output from the electronics due to movement of the resonator could be mistaken for a feedthrough signal. A simple method of ensuring that there is no signal due to movement of the resonator is to set the DC bias voltage (V_s) at the readout combs to 0V. Therefore any signal observed must be due to the effect of feedthrough. Figure 3.2 shows the measured signal for a typical resonator as a function of the applied voltage in both frequency doubling and differential driving modes. The solid line in Figure 3.2 shows that when frequency doubling is used, the feedthrough signal is larger than the previously-measured crosstalk signal. When differential driving is used the dotted line in Figure 3.2 shows that this feedthrough signal is not completely cancelled. In fact, the signal is only reduced by approximately a factor of three when compared to the frequency doubling architecture. Practical experience has shown

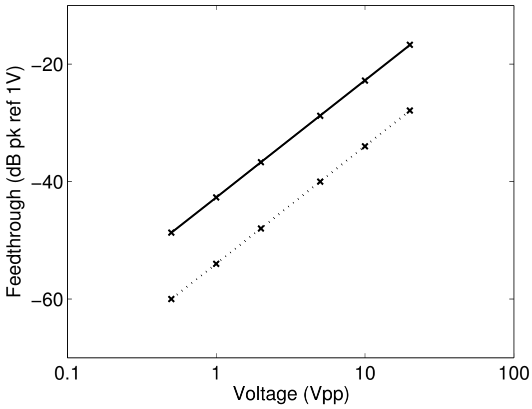

Figure 3.2: Feedthrough levels for frequency doubling mode (solid) and differential mode (dotted) driving configurations.

that the configuration of the bond wires plays a large part in determining the relative strengths of each feedthrough signal and the probable reason for this disappointing result is lack of symmetry in the configuration of bonding wires.

When the resonator is driven in air at atmospheric pressure, it is expected that the AC component of the driving force will be approximately 5V$_{\text{pp}}$, in order to maintain a detectable output signal of approximately 20mV$_{\text{rms}}$. Figure 3.2 shows that at this drive level, the feedthrough is approximately 20mV$_{\text{pp}}$. Because the feedthrough and velocity signals will be comparable when the resonator is driven using differential drive in air at atmospheric pressure, a compensation technique will be needed in order to reduce the feedthrough component (section 4.3.3).

3.4 Velocity and phase response

3.4.1 Vacuum

Electrical connections were made to the test PCB to differentially readout the velocity of the prototype resonator. To identify its resonant frequency, an oscilloscope was used to monitor the output from the instrumentation amplifier on the PCB. The FFT mode of the oscilloscope was used to monitor the frequency content of this output voltage. When frequency doubling is used and the driving frequency is far from the resonant frequency, the structure does not move and a small peak due to feedthrough is seen in the spectrum. The driving frequency can then

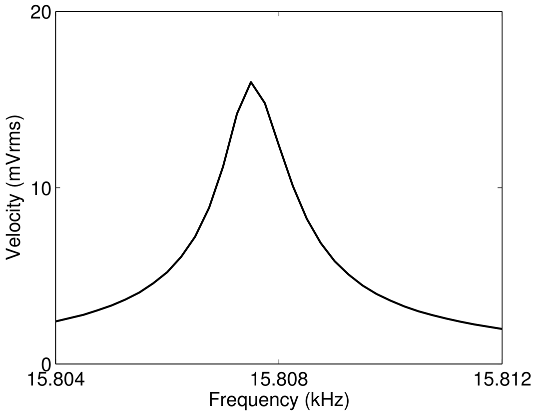

Figure 3.3: Velocity response at a pressure of 500mPa using frequency doubling with an AC drive voltage of $500mV_{pp}$.

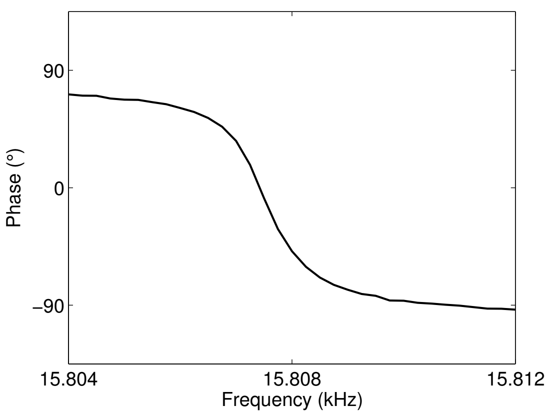

Figure 3.4: Phase response at a pressure of 500mPa using frequency doubling with an AC drive voltage of $500mV_{pp}$.

be slowly swept until the driving force is near the resonant frequency of the sample and the structure starts to move significantly. A second peak is then identifiable in the output spectrum at a frequency that is twice the frequency of the driving voltage. This is a reliable method for identifying the resonant frequency of a previously untested sample. Consequently, a single electrical connection was made to the driving channel to facilitate single-ended driving using frequency doubling. The remaining drive comb was unconnected.

Figures 3.3 and 3.4 show the velocity and phase responses respectively when the resonator was placed in a vacuum level of 500mPa. Due to the uncertainty of the value of the Q and its variation with pressure, a small AC driving voltage of $500mV_{pp}$ was used to excite the resonator. The figures show that the resonant frequency was detected at approximately 15.808kHz, which is higher than the design value. The -3dB bandwidth was measured to calculate the Q, yielding a value of approximately 10^4. The magnitude of the velocity response at the resonant frequency was approximately 10mV when typical driving voltages were used. Figure 3.4 shows that around the resonant frequency, the phase difference between the driving force and the measured velocity is the expected value of 0°. Further, also in-line with the theoretical result, the asymptotic values of the phase response approach ±90°.

3.4.2 Atmospheric pressure

The Q of the resonant system is expected to reduce to approximately 10 when the air pressure is increased to atmospheric pressure. Because a significant reduction in Q will result in a corresponding reduction in the observed velocity, it is necessary to increase the driving force. Consequently, when the resonator was operated in air a much larger driving voltage of $10V_{pp}$ was used. So that the velocity signal was separated from the significant feedthrough signal that occurs when large driving voltages are used, the resonator was again driven by frequency doubling. In this way, it was possible to recover the required velocity signal by post-processing the measured data, despite the presence of a relatively large feedthrough signal.

The velocity and phase responses for a frequency sweep at atmospheric pressure are given in Figures 3.5 and 3.6 respectively. The maximum velocity occurs at a frequency that is below

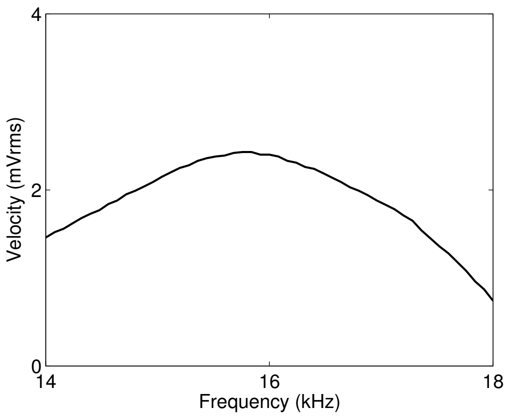

Figure 3.5: Velocity response at pressure of 100kPa using frequency doubling with an AC drive voltage of $10V_{pp}$.

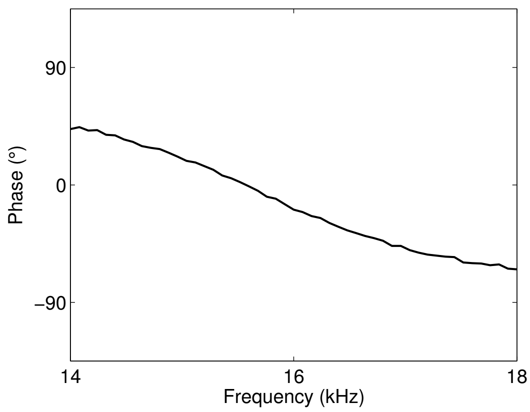

Figure 3.6: Phase response at pressure of 100kPa using frequency doubling with an AC drive voltage of $10V_{pp}$.

16kHz, however Figure 3.5 demonstrates that it has become difficult to determine the exact resonant frequency. As expected, the peak is broad and low. The measured Q-value is only five, lower than the estimated value of 10. Figure 3.6 shows a slowly changing phase response which crosses the 0° point at a frequency corresponding to the frequency of the maximum velocity. Once again due to the low Q it is difficult to determine the exact frequency. The most important conclusion of the results in this section is that the resonator behaves largely as expected, however parameters such the Q-value and resonant frequency are different to the expected values.

3.5 Resonant system parameters

To understand the relationship between ambient air pressure and Q is not trivial. Newell divides the air pressure into three regions to model the effect of varying the pressure [39,55]. In the first region the pressure is low and consequently air damping is negligible when compared to internal damping within the resonator. In the second region, air molecules interact with the resonator but not with each other. These interactions determine the damping in this region and consequently the Q-value is expected to be inversely proportional to the pressure ($Q \propto P_r^{-1}$). Finally, in the third region, the pressure is sufficiently high that air molecules interact with each other and viscous damping dominates. This means that in the third region the Q-value will be a function of the ambient air pressure and also the geometry of the resonator.

The relationship between the air pressure and the corresponding Q of the prototype resonator was characterised. Tests were performed at various pressure levels and the frequency swept to record the velocity response in each case. The Q-value was then calculated from the -3dB bandwidth. Twelve different pressure levels were used, spanning the seven orders of magnitude from 100kPa down to approximately 10mPa. Figure 3.7 shows the observed relationship between the Q and the ambient air pressure.

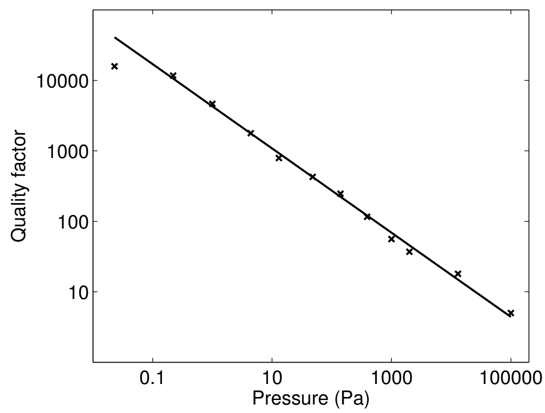

Figure 3.7: Relationship between natural quality factor and ambient air pressure.

The figure shows that the logarithm of the Q-value is directly proportional to the logarithm of the pressure. A best fit line has been drawn on the plot to indicate this relationship

$$Q = 4.3 \times 10^3 P_r^{-0.6}. \tag{3.1}$$

The data point at the lowest pressure was excluded from the data set used to determine the equation of the best fit line as it does not follow the same trend as the other points. It is probable that the equation describing the Q in Equation (3.1) is related to the resonator operating in the third region of pressure, where due to the complex relationship between geometry and damping levels the exact relationship is difficult to describe [51].

A small number of the prototype resonators were damaged while attaching bond wires for making electrical connections to the central bond pads. Therefore due to the risk and complexity associated with the bonding process and also the limited number of prototype samples available, only three resonators were available for this investigation. In section 3.4.1, the resonant frequency of one resonator was identified as 15.808kHz. The remaining samples were subsequently tested and Table 3.1 contains the values of the resonant frequencies of each of the available resonators. Table 3.1 shows that because of sample-to-sample manufacturing

Table 3.1: Measured resonant frequency for three test resonators, R_1, R_2 and R_3.

Resonator	Resonant frequency (kHz)
R_1	15.8
R_2	17.1
R_3	16.6

variations, the range of the resonant frequencies is 1.3kHz. The most important conclusion from the results in Table 3.1 is that the resonant frequency of each of the resonators is higher than the design frequency which is 13.4kHz. This can be explained by taking into account the over-sizing of the resonators by 250nm during the manufacturing process. The calculated mass of the resonator is 10% larger than designed because of this over-sizing, suggesting that the resonant frequency should be lower than expected. However, the spring constant is critically dependent upon the width of the folded beams and the over-size causes it to increase significantly, resulting in an overall rise in resonant frequency from the design value.

Another consequence of the over-sizing of features during the manufacturing processes is that the gaps between fingers of opposing combs are smaller than designed. The effect of this is that the actuation and readout capacitances formed from these fingers are larger than expected. A significant benefit of this is that there will be higher rate of change of capacitance with respect to displacement ($\frac{dC}{dx}$). To estimate the manufactured value of $\frac{dC}{dx}$, k is eliminated from (2.21) and rearranged to give

$$\frac{dC}{dx} = \sqrt{\left(\frac{V_{INA}}{4G_{INA}V_sV_{AC}V_{DC}R}\right) \times \left(\frac{m}{\omega_0 Q}\right)}. \tag{3.2}$$

To estimate $\frac{dC}{dx}$, the resonator was tested again to obtain the output voltage from the PCB, together with the resonant frequency, Q-value and the relevant test conditions. For the mass of the resonator, the estimated value of 4μg was used. The rate of change of capacitance with respect to displacement could then be calculated by solving Equation (3.2), giving a value of 16.2fFμm^{-1}.

Table 3.2 contains the parameter values that have been estimated and also the corresponding design values. Due to the over-sizing of resonator features during the manufacturing process the mass and the spring constant are larger than the design values, however they can not be measured directly. The only parameter that can be measured is the resonant frequency ($\omega_0 = \sqrt{k/m}$). The spring constant and not the mass is particularly sensitive to the small changes in geometry between samples, therefore to estimate m and k it was assumed that any variation in resonant frequency between samples was attributed entirely to changes in the spring constant. Sample-to-sample variation in both the Q-value and $\frac{dC}{dx}$ was not significant.

Table 3.2: Estimated and designed system parameters.

Parameter	Design value	Estimated value
m	3.6μg	4μg
k	25.4Nm^{-1}	$\sim$39$\rightarrow$47Nm^{-1}
$\frac{dC}{dx}$	13.4fFμm^{-1}	16.2fFμm^{-1}
Q	-	4.3$\times$10^{3}P$_r^{-0.6}$

3.6 Characterisation of driving schemes

To avoid feedthrough, the resonator was testing using frequency doubling ($F = \frac{V_{AC}^2}{2}\frac{dC}{dx}$). Results of these tests did not expose any unexpected behaviour and when the magnitude of the AC driving voltage was increased by a factor of two, as expected this led to a fourfold increase in the velocity of the resonator. However, if the effective Q of the resonant system is to be increased by velocity feedback, differential driving will be needed.

Using differential driving, the magnitude of the resulting force ($F = 2V_{AC}V_{DC}\cos(\omega t)\frac{dC}{dx}$) is expected to be proportional to the magnitude of the AC and DC components of the overall driving voltage. The velocity and phase responses were recorded at various AC voltage levels. As expected, the measured velocity was directly proportional to the magnitude of the AC driving component. The effect of changing the magnitude of the DC driving component was then studied. Figure 3.8 shows that this caused the desired increase in the velocity-dependent output voltage, however as the size of the DC component was increased, the resonant frequency decreased. Due to this unexpected shift in resonant frequency, the corresponding phase responses shown in Figure 3.9 are also shifted in frequency. Any sensor designed to detect changes in mass by monitoring the resonance of a MEMS mass-spring-damper system would interpret any undesired decrease in resonant frequency as the presence of a measurand. Therefore it is important to understand the mechanism responsible for this unexpected variation in the resonant frequency.

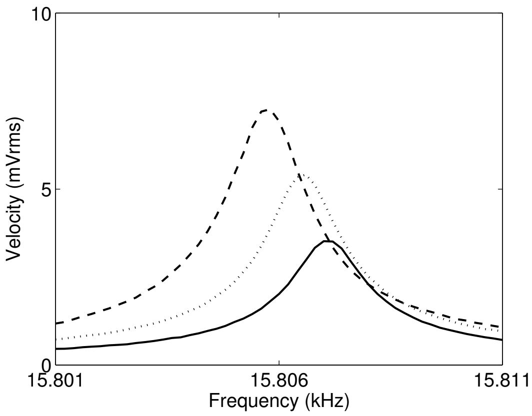

Figure 3.8: Velocity response at DC drive voltages of 1V (dashed), 750mV (dotted) and 500mV (solid).

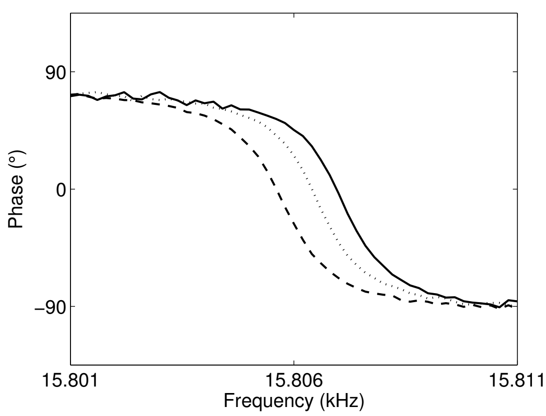

Figure 3.9: Phase response at DC drive voltages of 1V (dashed), 750mV (dotted) and 500mV (solid).

3.7 Voltage-controlled resonant frequency

3.7.1 Effect of DC bias voltage on resonant frequency

An unexpected relationship between the DC component of the differential driving voltage and the resonant frequency of the prototype MEMS structure has been observed. To confirm that this effect is related to the magnitude of the DC voltage applied to a comb capacitance and not some other nuance of the differential driving scheme, the resonator was tested using frequency doubling. This drive architecture leaves one of the two driving combs available for the application of a test DC bias voltage. In this way, tests can be performed to study the resulting effect on the resonant frequency of varying the test voltage.

For this test, the pressure was 500mPa and to drive the resonator an AC driving voltage of 500mV$_{pp}$ was applied. The velocity signal was recorded using differential readout. At the free drive comb, DC bias voltages of 0V (control), 2V, 4V and 8V were connected in turn and the frequency swept to record the corresponding velocity responses. Figure 3.10 shows that

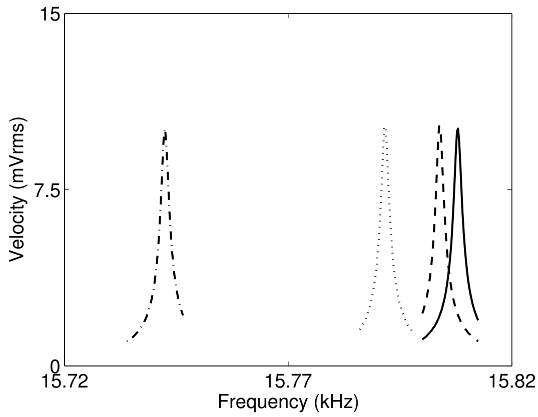

Figure 3.10: Relationship between resonant frequency and DC bias voltages, 0V (solid), 2V (dashed), 4V (dotted) and 8V (dash-dot), applied at free drive comb.

the effect of applying the DC bias was to reduce the resonant frequency of the resonator. This means that the observed change in resonant frequency is attributed solely to the application of the DC bias voltage.

3.7.2 Non-ideal comb capacitance

The application of a DC bias voltage causes a reduction in the observed resonant frequency of the prototype resonator. A relationship between the resonant frequency of a MEMS structure and the bias voltages that are applied to it can often be explained by taking into account undesirable electrostatic effects [56, 57]. In particular, the presence of any undesired parallel plate capacitances between the movable resonator and the fixed actuation and readout structures is likely to cause a voltage-dependent electrostatic force. The presence of these parasitic capacitances will contribute to the overall actuation and readout capacitances and hence the capacitance versus displacement profile ($\frac{dC}{dx}$). Recall that the ideal electrostatic comb drive has a linear capacitance versus displacement profile and consequently $\frac{dC}{dx}$ is fixed. This means that when a DC bias voltage is applied to a drive or readout comb capacitance the resulting force ($F_{stat} \propto \frac{V_{DC}^2}{2}\frac{dC}{dx}$) is ideally constant. Conversely, if $\frac{dC}{dx}$ is not a constant, then the force due to any applied DC bias will be a function of position. When a displacement-dependent force ($F_{E-spring}(x)$) is applied to the resonator in addition to the primary driving force, the equation of motion will be

$$\ddot{x} + \frac{c}{m}\dot{x} + \frac{k}{m}x = \frac{F_0}{m} + \frac{F_{E-spring}(x)}{m}. \tag{3.3}$$

If the displacement-dependent force is directly proportional to the displacement ($F_{E-spring} = k_{E-spring}x$), then this additional force will act to reduce the effect of the spring constant

$$\ddot{x} + \frac{c}{m}\dot{x} + \frac{k - k_{E-spring}}{m}x = \frac{F_0}{m}. \tag{3.4}$$

Equation (3.4) shows that if the electrostatic force generated by a comb capacitance in the manufactured resonator contains a component that is directly proportional to the displacement of the structure, the effective spring constant will be reduced. This apparent reduction in the spring constant will reduce the observed resonant frequency of the resonator. It is therefore possible that the observed voltage-dependence of the resonant frequency of the prototype system can be explained by taking into account the presence of any parasitic capacitances which could cause a non-linear relationship between capacitance and displacement.

To estimate the degree of any non-linearity in $\frac{dC}{dx}$ in the manufactured resonator, the dimensions of the resonator design were oversized by 250nm in order to account for under-etching during the manufacturing process. The comb capacitance was estimated by colleagues in Birmingham University (using COMSOL Multiphysics) over a wide range of displacements. Figure 3.11 shows the relationship between comb capacitance and displacement in the manufactured resonator. When the comb fingers are displaced such that the overlap is decreased (corresponding to a negative displacement), the predicted capacitance begins to increase. This simulated increase in capacitance when the finger overlap reduces is counter-intuitive. However, this result can be explained by taking into account the presence of parasitic parallel plate capacitors formed by the backs of the movable and static comb arms moving increasingly together as the comb teeth move apart. A small section of an SEM image of the resonator is shown in Figure 3.12, where is it possible to see the close proximity of the movable and static comb arms.

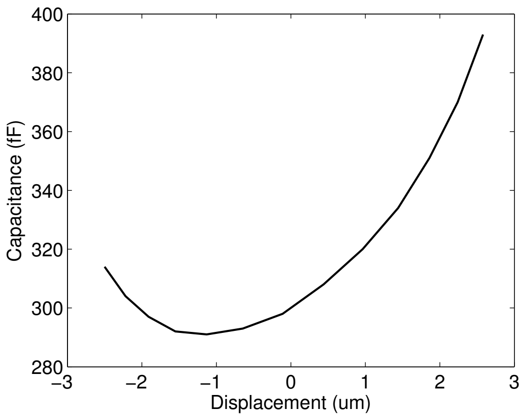

Figure 3.11: Comb capacitance versus displacement simulated using COMSOL Multiphysics.

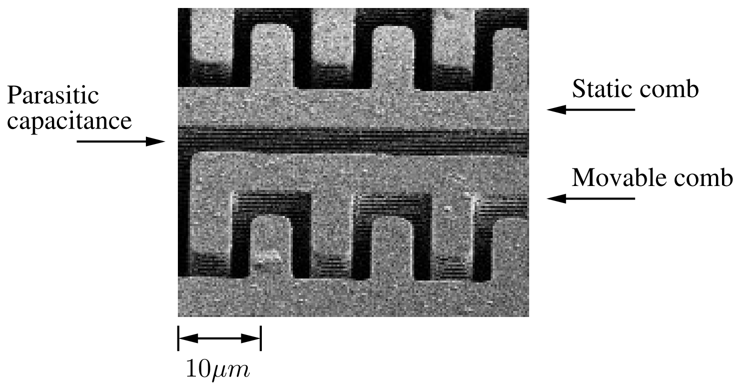

Figure 3.12: SEM image showing capacitor formed between backs of comb arms.

A polynomial was fitted to describe the relationship between capacitance and displacement shown in Figure 3.11. Differentiating the polynomial with respect to x gives

$$\frac{dC}{dx} = C_0' + C_1'x + C_2'x^2 + C_3'x^3. \tag{3.5}$$

Table 3.3 contains the COMSOL Multiphysics values for the coefficients C_0', C_1', C_2' and C_3'. The solid line in Figure 3.13 shows the capacitance versus displacement profile predicted by COMSOL Multiphysics plotted again. In addition, the dotted line in Figure 3.13 has been plotted using, for C_0', the value of $\frac{dC}{dx}$ that has been estimated from measured data in section 3.5. This is possible because in section 3.5 the resonator was characterised at a small displacement, which means that the estimated value of $\frac{dC}{dx}$ is approximately equal to C_0'.

Table 3.3: Parameter values for polynomial describing the estimated $\frac{dC}{dx}$.

Parameter	Value	Units
C_0'	14.7×10^{-9}	Fm^{-1}
C_1'	10.1×10^{-3}	Fm^{-2}
C_2'	-91.2	Fm^{-3}
C_3'	1.91×10^{9}	Fm^{-4}

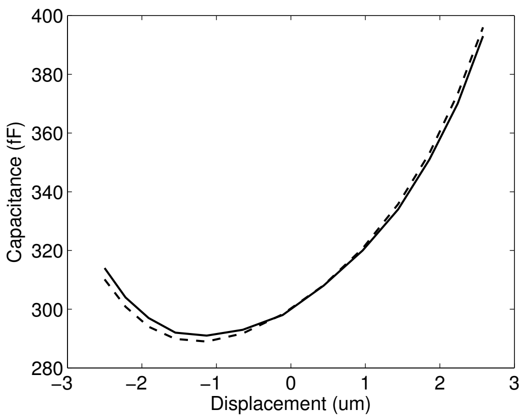

Figure 3.13: Simulated relationship between static comb capacitance and displacement using COMSOL Multiphysics (solid) and measured (dashed) values for C_0'.

The profiles in Figure 3.13 have very similar characteristics. This means that the extracted coefficients of the polynomial describing $\frac{dC}{dx}$ must be very sensitive to small changes in the capacitance versus displacement profile. The key consequence of this is that when COMSOL Multiphysics is used to model $\frac{dC}{dx}$, the validity of the extracted coefficients will be affected by small differences between the simulated and manufactured comb capacitances. This means that when the characteristics of a fabricated resonator are modelled using the coefficients calculated by COMSOL Multiphysics, a discrepancy between the measured and simulated behaviour of the system could occur.

With these parameters, it is possible to develop a model to describe the relationship between the observed resonant frequency of a test resonator and the corresponding DC bias voltage applied to a comb capacitance. When the resonator is operated with differential readout, the electrostatic forces due to readout bias voltages on the opposing comb capacitances ($C_{+,-}$) are

$$F_{E-spring+,-} = \frac{V_{DC}^2}{2}\frac{dC_{+,-}}{dx}. \quad (3.6)$$

Taking particular care to define the direction of displacement means that

$$\frac{dC_+}{dx} = C_0' + C_1'x + C_2'x^2 + C_3'x^3, \quad (3.7)$$

$$\frac{dC_-}{dx} = C_0' - C_1'x + C_2'x^2 - C_3'x^3. \quad (3.8)$$

When differential readout is used, the electrostatic forces generated by the DC bias voltages are in opposing directions. This means that the overall force is

$$F_{E-spring+} - F_{Epsring-} = V_{DC}^2[C_1'x + C_3'x^3]. \quad (3.9)$$

The most significant term in this expression at typical displacements is the term in x, therefore the overall force due to the application of the differential bias voltages is

$$F_{E-spring} = k_{E-spring} = V_{DC}^2 C_1' x. \tag{3.10}$$

Similarly, for the application of a single DC bias voltage the resulting force is

$$F_{E-spring} = \frac{V_{DC}^2 C_1' x}{2}. \tag{3.11}$$

The structure has four combs to which a DC voltage can be applied. The forces from these voltages will add to each other and so a more general expression for the electrostatic force due to the application of a number (n_{dc}) of bias voltages (V_{DCa}) is

$$F_{E-spring} = k_{E-sping} x = \left(\frac{C_1'}{2} \sum_{a=1}^{n_{dc}} V_{DCa}^2 \right) x, \tag{3.12}$$

where $n_{dc} \leq 4$. This shows that the native spring constant of the system will be reduced by an amount ($k_{E-spring}$) that is determined by the bias voltages applied to the comb capacitances. The equation of motion is updated to include this term which gives

$$\ddot{x} + \frac{c}{m}\dot{x} + \left(\omega_0^2 - \frac{C_1'}{2m} \sum_{a=1}^{n_{dc}} V_{DCa}^2 \right) x = \frac{F_0}{m}. \tag{3.13}$$

Therefore, the effective resonant frequency is described by the following equation

$$\omega_e = \sqrt{\omega_0^2 - k_e \sum_{a=1}^{n_{dc}} V_{DCa}^2}, \tag{3.14}$$

where $k_e = \frac{C_1'}{2m}$ and $n_{dc} = 4$.

A similar analysis was performed which models the effective resonant frequency when one of the combs is excited using frequency doubling. In the model, DC bias voltages are applied to the remaining three combs of the structure. Equation (3.15) describes the effective resonant frequency for this model

$$\omega_e = \sqrt{\omega_0^2 - k_e\left[\frac{V_{AC}^2}{2} + \sum_{a=1}^{n_{dc}} V_{DCa}^2\right]}. \tag{3.15}$$

In the equation above, because one comb capacitance is used to apply the driving voltage $n_{dc} \leq 3$. Surprisingly, Equation (3.15) shows that the effective resonant frequency (ω_e) is a function of both V_{DC} and V_{AC}. Previous results, however, do not expose this relationship as the contribution due to V_{AC} was significantly smaller than the contribution due to V_{DC}.

Similarly, Equation (3.16) describes the effective resonant frequency when differential driving is used

$$\omega_e = \sqrt{\omega_0^2 - k_e\left[2V_{DCb}^2 + V_{AC}^2 + \sum_{a=1}^{n_{dc}} V_{DCa}^2\right]}. \tag{3.16}$$

In the model of the differentially-driven system, V_{DCb} is the magnitude of the differential driving voltages. The bias voltages applied to the two remaining combs are represented by V_{DCa}.

To extract the pure resonant frequency (ω_0) and the softening constant (k_e), Equation (3.15) can be rearranged to give

$$\omega_e^2 = \omega_0^2 - k_e\left(\frac{V_{AC}^2}{2} + 2V_s^2\right). \tag{3.17}$$

The resonator was tested with differential readout and the magnitude of the readout bias voltage (V_s) and the AC driving voltage determined the effective resonant frequency of the resonant system. A small AC driving voltage of $1\mathrm{V_{pp}}$ was used and the readout bias voltage was systematically reduced from 8V to 1V and the corresponding resonant frequency was recorded. Figure 3.14 shows the observed relationship between V_s and the effective resonant frequency. One problem with this experiment was that when the readout bias voltage is small this limits the magnitude of the velocity-dependent output voltage, even when the velocity is large. Fortunately, it is still possible to record the resonant frequency with high accuracy using the FFT mode on an oscilloscope.

The line of best fit in Figure 3.14 was used to determine values for ω_0 and k_e. Extracted values are given in Table 3.4. Since k_e is defined as $\frac{C_1'}{2m}$, it is possible to determine if the

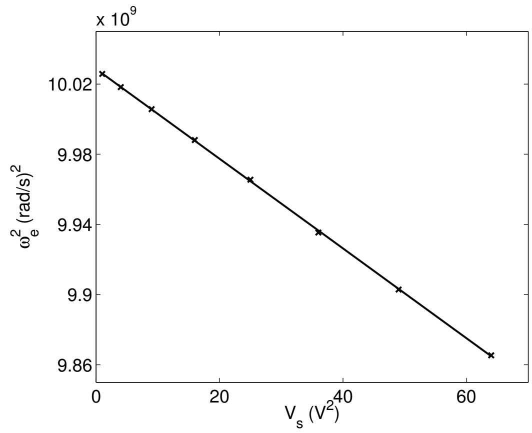

Figure 3.14: Relationship between the observed resonant frequency and the applied DC bias voltage.

extracted value in Table 3.4 is plausible by substituting simulated values for C_1' and m. Using the estimated value of 4μg for the mass and $C_1' = 10.1 \times 10^{-3} Fm^{-2}$ from Table 3.3, gives $\frac{C_1'}{2m} = 1.27 \times 10^6$. This corresponds to a discrepancy from the measured value in Table 3.4 of less than 1%. This suggests that the simulated form of $\frac{dC}{dx}$ used to extract C_1' is a good model and also that the estimate of the mass of the resonator is quite accurate.

Since the value of C_1' that has been measured is very similar to the value calculated by COMSOL Multiphysics, Equation (3.15) could be used to draw the line of best fit shown in Figure 3.14. This means that Equations (3.15) and (3.16) can be used to predict the effective resonant frequency of the system for the particular bias and driving conditions. It is therefore possible to vary the bias conditions applied to the resonator to create a predictable, repeatable and reversible change in the resonant frequency of the prototype resonator.

Table 3.4: Natural resonant frequency (f_0) and measured softening constant (k_e).

Parameter	Value	Units
f_0	15938	Hz
k_e	1.28×10^6	$N^2m^{-2}kg^{-2}V^{-2}$

3.8 Non-linear velocity and phase response

3.8.1 Background

Previously, when the resonator was tested at low pressure, a conservative driving force was used to characterise the response of the system at a typical estimated displacement of 100nm. The driving voltage was subsequently increased to cause a displacement of approximately 1μm and the system was tested at various vacuum levels. When the pressure is 13Pa and the displacement is above 100nm, the velocity response peak is seen to bend to the left and a jump is observed close to the resonant frequency. There is also a discontinuity in the phase response at the frequency corresponding to the jump in the velocity response. Experimental results showing the behaviour of the resonator are in Figures 3.15 and 3.16 for an estimated displacement of 1.2μm. Similarly, when the pressure was 170Pa and the driving force increased to

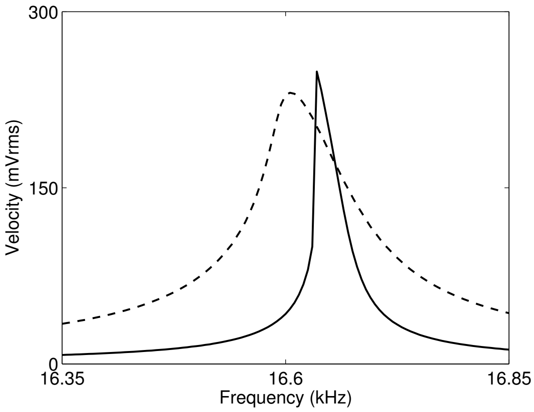

Figure 3.15: Velocity response at a pressure of 13Pa (solid) and 170Pa (dashed), showing non-linear behaviour.

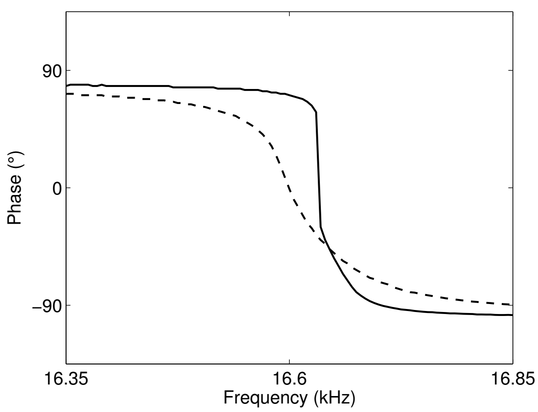

Figure 3.16: Phase response at a pressure of 13Pa (solid) and 170Pa (dashed), showing non-linear behaviour.

maintain a similar displacement, similar behaviour is observed. However, the key difference is that the discontinuity in the velocity and phase response does not appear.

To describe the behaviour, any new physical model must accurately represent the non-linear ‘shark’s fin’ peak shape, the presence of the discontinuity only when the Q is relatively high and also the corresponding phase responses. Various previous investigations show that non-linear effects in MEMS devices are a relatively common phenomenon [58]. In fact, evidence of a so-called ‘spring softening’ effect which is attributed to electrostatic effects has been described previously [59, 60]. In some cases this effect is exploited in order to cancel undesirable mechanical 'spring hardening' effects [61, 62].

3.8.2 Analysis

To investigate if electrostatic effects can explain the unexpected velocity and phase responses shown in Figures 3.15 and 3.16, consider the opposing electrostatic forces generated when a DC readout voltage is applied to opposing comb capacitances. The resulting electrostatic force is described by Equation (3.9),

$$F_{E-spring1} - F_{E-spring2} = V_{DC}^2[C_1'x + C_3'x^3].$$

In the analysis in the previous section, only the first term in Equation (3.9) was considered. However, when the displacement of the resonator is large the second term ($C_3'x^3$) can not be ignored. Consequently, the model of the system was updated to include the effect of this term. In this example, the primary driving force is generated by frequency doubling however a similar argument can be applied for a differential driving configuration. When frequency doubling is used the updated equation of motion is

$$\ddot{x} + \frac{c}{m}\dot{x} + \frac{k}{m}x = V_{AC}^2\left(\frac{1+\cos(2\omega t)}{4m}\right)[C_0' + C_1'x + C_2'x^2 + C_3'x^3] + \frac{V_s^2[C_1'x + C_3'x^3]}{m}. \quad (3.18)$$

Rearranging gives,

$$\ddot{x} + \frac{\omega_e}{Q}\dot{x} + \omega_e^2 x + \gamma x^3 = \frac{V_{AC}^2}{4m}\cos(2\omega t)[C_0' + C_1'x + C_2'x^2 + C_3'x^3] + \frac{V_{AC}^2}{4m}[C_0' + C_2'x^2], \quad (3.19)$$

where ω_e is given by Equation (3.15) and $\gamma = -\frac{C_3'}{m}\left(\frac{V_{AC}^2}{4} + V_s^2\right)$. The left hand side of Equation (3.19) is a Duffing equation [63–65]. The typical equation of motion for a Duffing resonator is

$$\ddot{x} + \frac{\omega_0}{Q}\dot{x} + \omega_0^2 x + \eta x^3 = \frac{F_0}{m}. \quad (3.20)$$

Equations (3.19) and (3.20) are similar, although Equation (3.19) contains terms in the driving force that vary with displacement. Since $\gamma < 0$ in Equation (3.19), this corresponds to a spring softening type non-linearity for a Duffing oscillator ($\eta < 0$). This means that it is possible that the model described by Equation (3.19) can be used to explain the observed spring softening effect that occurs when the displacement is large.

3.8.3 Frequency content of output voltage

If the prototype resonator behaves in a similar way to a Duffing resonator, the displacement and velocity will contain components at the fundamental (f) and 3rd harmonic frequencies (3f) [66]. The output voltage from the test PCB was measured when the resonator was operated in the non-linear regime. Figure 3.17 shows the frequency content of one of the differential readout channels. For this test the resonator was tested using frequency doubling and the feedthrough signal at the driving frequency (0.5f) was removed using a digital filter. Figure 3.17 shows the

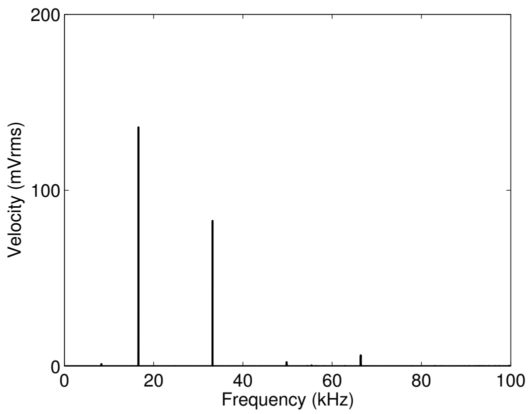

Figure 3.17: Frequency spectrum of the AD620A output voltage showing frequency content at the fundamental and 2nd harmonic frequencies for driving voltage of 16V_{pp} at pressure 170Pa.

presence of a very small peak at 3f and a slightly larger peak at the 4th harmonic frequency (4f). However, the observed power is largely at the fundamental and 2nd harmonic (2f) frequencies, which is unexpected.

Since the most significant higher-order peak in the frequency spectrum of the output voltage from a readout channel occurs at 2f and not 3f, the frequency content of the current generated in the readout capacitance has been investigated. The current is described by Equation (2.17),

$$i(t) = V_s \frac{dC}{dx}\frac{dx}{dt}.$$

Substituting Equation (3.5) for $\frac{dC}{dx}$ gives

$$i(t) = V_s \dot{x} \left[C_0' + C_1' x + C_3' x^3 \right]. \tag{3.21}$$

In Equation (3.21) the term in x^2 has been ignored because even when the displacement is large its contribution is insignificant. For a Duffing resonator, velocity and displacement contain power at f and 3f, hence Equation (3.21) contains many terms. Because of the non-ideal comb capacitance, the resulting current contains even harmonic frequencies in addition to the expected components at f and 3f.

The most significant frequency in a Duffing resonator will be at the fundamental frequency [66]. When the displacement is approximated as $x = X\sin(\omega t)$, the corresponding output current is

$$i(t) = \omega V_s \left[X C_0' \cos(\omega t) + \left(X^2 \frac{C_1'}{2} + X^4 \frac{C_3'}{4} \right) \sin(2\omega t) - X^4 \frac{C_3'}{8} \sin(4\omega t) \right]. \tag{3.22}$$

Equation (3.22) shows that due to the non-ideal comb capacitance, the measured current contains components at f and 2f. There will also be a smaller component at 4f. For completeness, a full analysis in appendix B includes the frequency content at 3f in velocity and displacement. Equations (3.19) and (3.22) were solved to calculate the output current (and hence voltage) as a function of time. Figure 3.18 shows the simulated and measured frequency spectrums. The

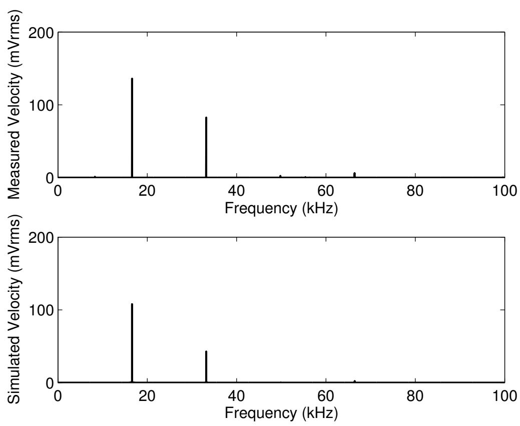

Figure 3.18: The measured frequency spectrum (top) and the simulated spectrum (bottom) of the AD620A output voltage, showing frequency content at the fundamental and 2nd harmonic frequencies, for a driving voltage of $16V_{pp}$ at pressure 170Pa.

simulation frequency was the frequency where the maximum velocity occurs for this sample. Figure 3.18 shows that in simulation the frequency content of the output voltage displays similar characteristics to the measured behaviour. A key feature of the these results is that the dominant higher-order peak occurs at 2f and the ratio of the heights of the peaks at f and 2f is approximately 2:1. Therefore the most important conclusion of these simulations and measurements is that because the comb capacitance is not ideal, a large term at 2f always occurs when the displacement is large. The significance of this result is that in a MEMS Duffing resonator with electrostatic drive and readout, a term at 3f can appear in the output current, however this is not necessarily the most significant higher order term.

3.8.4 Simulation of non-linear velocity and phase response

Transient simulations have been performed to calculate the velocity and phase response of the Duffing-like system. Equation (3.19) was solved using the MATLAB `ode45` solver [1]. To represent $\frac{dC}{dx}$, the values extracted in simulation for C_0', C_1' and C_3' (Table 3.3) were used. Results of these simulations are in Figures 3.19 and 3.20. Figure 3.20 shows that the simulated

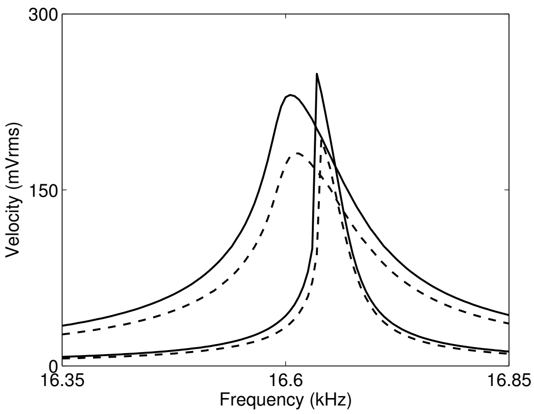

Figure 3.19: Simulated (dashed) and measured (solid) velocity responses at two pressure levels showing modelling of non-linear response.

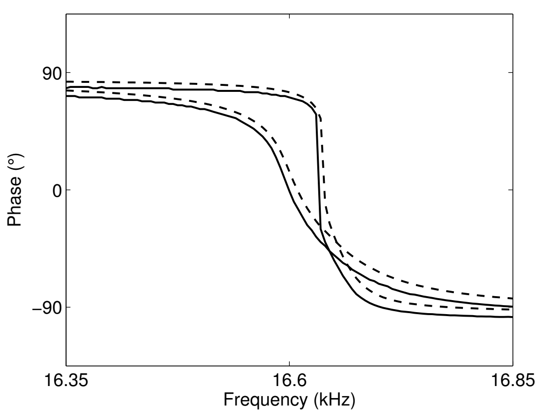

Figure 3.20: Simulated (dashed) and measured (solid) phase responses at two pressure levels showing modelling of non-linear response.

and measured phase responses are similar. However, the two sets of data in Figure 3.19 have the same shape but do not coincide. This suggests that the model (Equation (3.19)) is correct, but that the parameters may not be accurate.

[1]MATLAB code is given in appendix C

In the simulations shown in Figure 3.19, the value of C'_0 that was used has been generated from the capacitance versus displacement curve predicted by COMSOL Multiphysics (Figure 3.11). Since the magnitude of C'_0 governs the magnitude of both the driving force and the output current, the effect of any error in its value will be significant. In section 3.5, the resonator was characterised at a small displacement and $\frac{dC}{dx}$ was estimated from the measurements. As the displacement was small, $\frac{dC}{dx}$ will be equal to C'_0. This means that the estimated value of $\frac{dC}{dx}$ can be used for C'_0 to simulate the behaviour of the system. Because the value for C'_0 that has been estimated from measurements is more accurate than the design value calculated by COMSOL Multiphysics, the simulated behaviour of the system is expected to correspond more closely to the observed behaviour.

Further MATLAB simulations were subsequently performed using, for C'_0, the value of $\frac{dC}{dx}$ that has been estimated from measurement (section 3.5). Since varying C'_0 only affects the magnitude of the primary driving force and the velocity-dependent output current, as expected updating the value of C'_0 does not affect the observed phase response of the system. This is shown in Figure 3.22. Figure 3.21 shows a good match between simulation and measurement for the velocity peak. This means that the unexpected behaviour of the velocity peak has been explained simply by modelling the non-ideal comb capacitance.

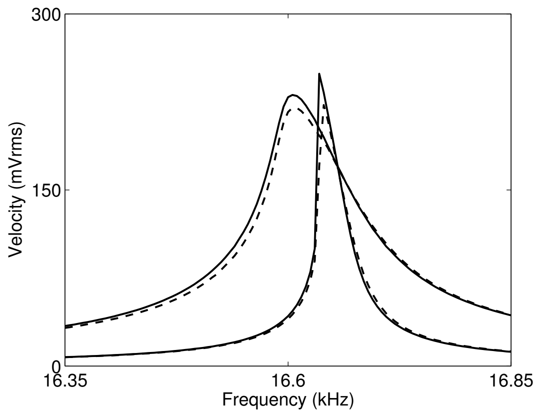

Figure 3.21: Simulated (dashed) and measured (solid) velocity responses at two pressures showing modelling of non-linear response, with updated value for fundamental component in $\frac{dC}{dx}$, C'_0.

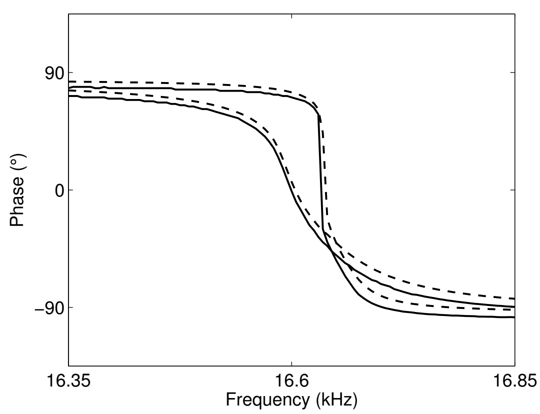

Figure 3.22: Simulated (dashed) and measured (solid) phase responses at two pressures showing modelling of non-linear response, with updated value for fundamental component in $\frac{dC}{dx}$, C'_0.

3.9 Summary

In this chapter the characterisation of a prototype MEMS resonator was described. The device was designed by colleagues at Birmingham University and fabricated at QinetiQ. As the resonator comprises four interdigitated comb structures creating a differential drive and readout architecture, any undesirable feedthrough signal from the drive electronics to the readout electronics is theoretically eliminated. Unfortunately, results show that the performance of the drive and readout configuration is poorer than expected. Practical experience has shown that the configuration of the electrical bond wires plays a significant role in determining the strength of the undesirable feedthrough signal. Measurements performed by colleagues at Birmingham University have shown that the geometry of the manufactured resonator differs from design values. The effect of this difference is to increase the mass and spring constant of the resonant system and also to increase $\frac{dC}{dx}$.

Experimental results indicate that when the DC component of the differential drive voltage is increased, the resonant frequency of the mass-spring-damper system reduces. Analysis has shown that this effect is caused by an unexpected non-linear relationship between the overall capacitance and displacement. This non-linear relationship is caused largely by the presence of undesirable parallel plate capacitors formed between the backs of neighbouring comb arms. The effect of the first order position-dependence has been characterised and equations are given to predict the effective resonant frequency as a function of the particular bias conditions. A possible benefit of this phenomenon is the resulting ability to control the resonant frequency of the system simply by varying the bias voltages applied to the structure.

In addition to the unexpected relationship between bias voltages and the resonant frequency, measurements show that when the displacement is large, the resonant peak bends towards the left. This suggests the presence of a ‘spring softening’ Duffing-type non-linearity. Analysis and simulation show that the third order position-dependent in $\frac{dC}{dx}$ explains the observed behaviour. Calculating the expected frequency content of the output current from a comb capacitance shows that when the displacement is large, a significant component appears at the second harmonic frequency. In this system, this 2f component dominates the small component at the third harmonic frequency that occurs for a Duffing type non-linearity.

Chapter 4

Quality factor control

4.1 Introduction

A resonator with differential drive and readout has been designed and manufactured. The differential driving architecture can be used to generate a driving force which is directly proportional to the applied AC and DC driving components. The differential readout system that has been implemented delivers a voltage proportional to the velocity of the resonator. Using this arrangement, it will be possible to generate a feedback force directly proportional to the velocity of the resonator. In this way, the effective quality factor of the resonant system can be increased using a feedback loop constructed from simple electronic circuits.

In the previous chapter, the prototype MEMS resonator manufactured for this project was fully characterised. A significant result of this characterisation is that a larger than expected feedthrough signal between the drive and readout electronics has been observed. When the resonator is moving in air at atmospheric pressure, the magnitude of this feedthrough signal is similar to the magnitude of the measured velocity signal. Consequently it is expected that it will be necessary to remove this feedthrough signal when Q-control is implemented at atmospheric pressure. In this chapter a technique for removing the undesirable feedthrough signal is described and the performance of the prototype resonator under the influence quality factor control is characterised.

4.2 Q-control at low pressure

4.2.1 Feedback electronics

To increase the Q of the prototype resonant system, a feedback force must be generated from the instantaneous velocity signal produced by the test PCB. The effect of this feedback force, when added to the primary driving force, will be to partially compensate for air damping and hence to increase the Q of the resonant system. To generate the required feedback voltage, the velocity-dependent voltage at the output of the AD620A instrumentation amplifier was amplified further. Figure 4.1 shows the electronics used to form the feedback loop. The circuit is only required to amplify the velocity signal and to add the resulting voltage to the primary driving voltage. In the amplification stage, an inverting amplifier with a variable resistor in its

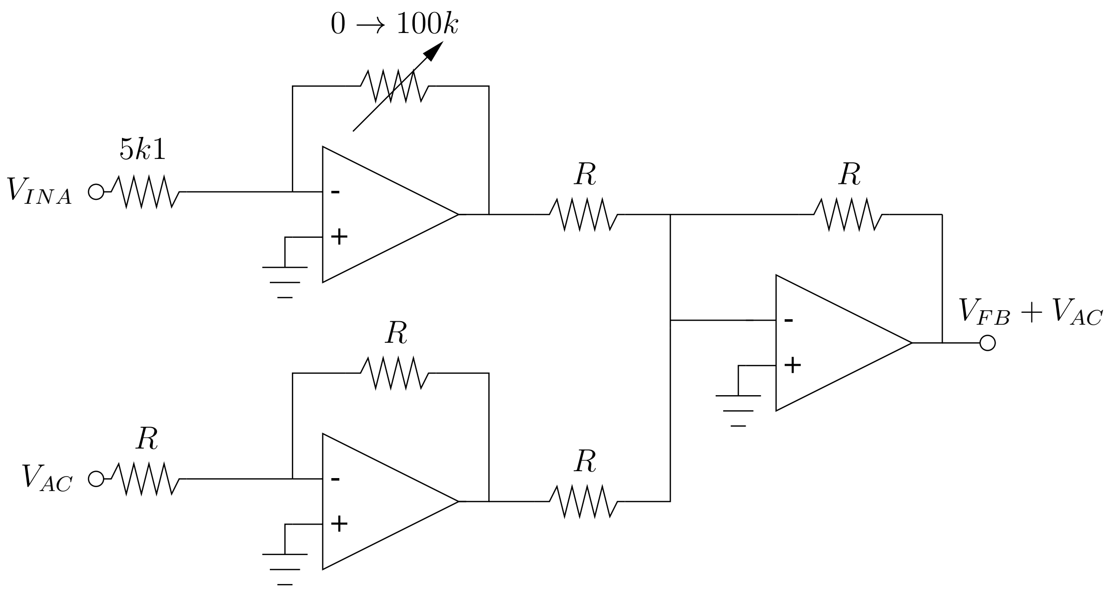

Figure 4.1: Electronic circuits required to generate feedback voltage and subsequently sum with primary driving voltage.

feedback loop has been used. This means that the feedback voltage can be attenuated as well as amplified. In order to preserve the phase of the velocity signal, which is shifted by -180° by the amplifier, a subsequent inverting amplifier is required. However instead of adding a further inverting stage, the inverting nature of the final summing stage has been exploited in order to change the phase of the velocity signal by a further 180°.

4.2.2 Low pressure testing

To test the performance of the resonator under the action of Q-control, the resonator was placed in a vacuum level of 30Pa and electrical connections made for differential driving and readout. A deeper vacuum, where the natural Q is higher, was not used in order to minimise the risk of damaging the resonator by causing a large displacement. Initially, the resonator was tested at the native Q for this pressure. A DC driving voltage of 1.6V and an AC driving voltage of 50mV$_{pp}$ were used. The solid lines in Figures 4.2 and 4.3 show the velocity and phase responses respectively and the natural Q is approximately 500 at this pressure level. The feedback loop was then closed and the loop gain increased until the effective Q reached approximately 3500. The dotted lines in Figures 4.2 and 4.3 show the corresponding responses for the Q-controlled system. Further Q-enhancement was not attempted in order to minimise

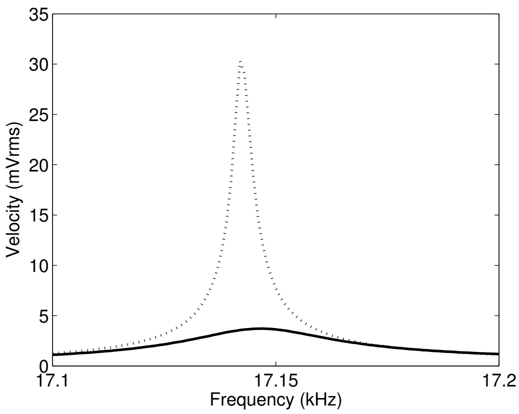

Figure 4.2: Velocity response at a medium vacuum level without Q-control (solid) and with Q-control (dotted).

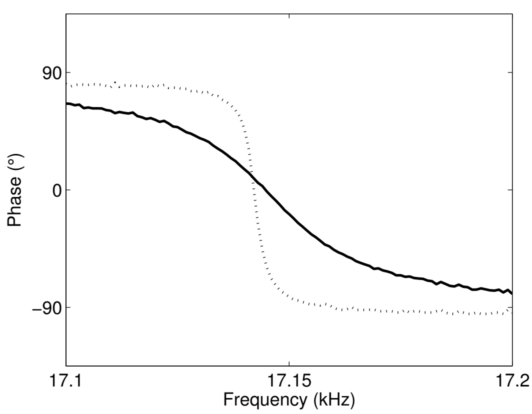

Figure 4.3: Phase response at a medium vacuum level without Q-control (solid) and with Q-control (dotted).

the risk of damaging the resonator by causing a displacement that is too large. A more critical appraisal of the results in Figures 4.2 and 4.3 suggests that the natural frequency of the Q-enhanced system is approximately 5Hz lower than before the implementation of Q-control. Whilst this unexpected effect is quite small, it is significant because the resonant frequency is normally stable when the bias voltages remain constant. This suggests that the effect is related to the action of Q-control and therefore it is expected that similar behaviour will be observed when the Q is controlled at atmospheric pressure.

4.3 Q-control at atmospheric pressure

4.3.1 Filter electronics

When the resonator operates at atmospheric pressure, the natural Q of the resonant system is five. Because of the low Q, the measured velocity signal at the output of the instrumentation amplifier on the test PCB is less than 10mV, even when relatively large AC and DC driving voltages are used. Due to this small output signal, the Signal-to-Noise Ratio (SNR) of the measured velocity signal will be low. This leads to the possibility of noise being amplified around the feedback loop resulting in a poor SNR of the Q-enhanced system [45].

To remove some of the noise from the velocity signal, it is desirable to place a filter in the feedback loop to significantly reduce out-of-band noise. An active bandpass filter using an op-amp circuit has been implemented. Op-amp circuits are frequently packaged as integrated circuits containing four amplifiers. Consequently, for this prototype system built from discrete electronic components, an 8^{th} order bandpass filter has been built by cascading four identical 2^{nd} order Sallen and Key circuits contained in a single OPA404 package [67, 68]. Figure 4.4 shows the schematic diagram for a single filter stage. The magnitude and phase responses for the filter are given in Figures 4.5 and 4.6. Each filter stage has a Q of 1.5 and a centre frequency of approximately 17kHz. These characteristics have been chosen to ensure that the filter is suitable for testing resonators with a typical variation in resonant frequency. The overall filter has a roll-off of 160dB per decade and a gain of approximately 30 in the passband.

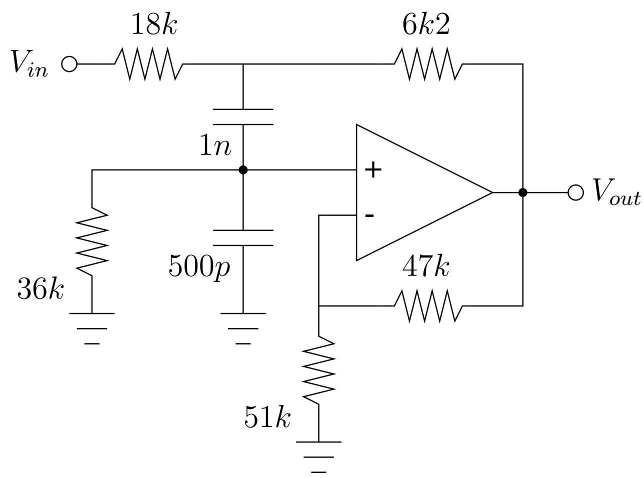

Figure 4.4: Circuit schematic for a 2^{nd} order Sallen and Key bandpass filter stage.

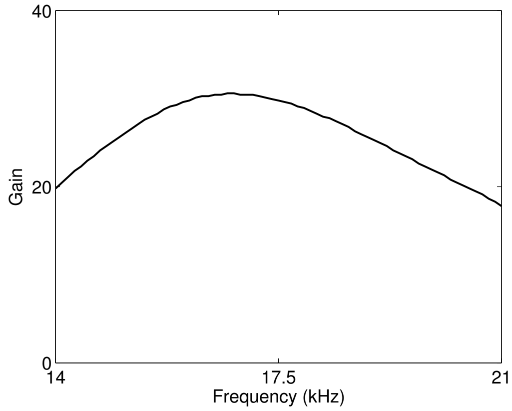

Figure 4.5: Magnitude response of 8th order bandpass filter.

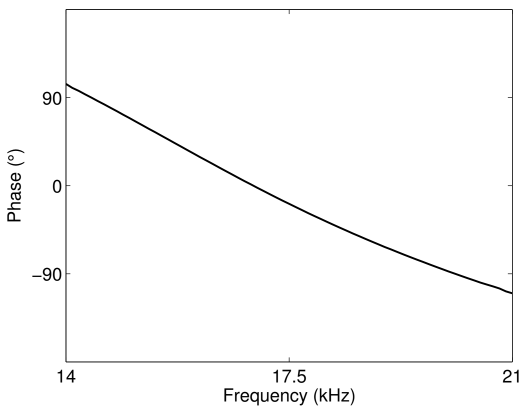

Figure 4.6: Phase change of signal due to 8th order bandpass filter.

For Q-control, the phase of the feedback signal must be in phase with the instantaneous velocity. Therefore the phase change between input and output signals introduced by the filter is designed to be 0° at the centre frequency. Measurements show that around the resonant frequency, the phase changes by ± 30m°Hz^{-1}. Consequently, when the filter centre frequency is close to the natural frequency of the MEMS resonator, the effect of the filter is to add only a small phase shift. Using this filter, it is possible to recover the small output signal from the readout electronics when the resonator is moving in air. This means that it will be possible to implement Q-enhancement in the absence of excessive noise.

4.3.2 Feedthrough analysis

In section 3.3, the feedthrough level observed when monitoring a typical sample was characterised. Results showed that despite the implementation of differential driving, feedthrough is only reduced by a factor of three when compared to the signal observed for the frequency doubling architecture. This poorer than expected result is due to the arrangement of bonding wires dominating the feedthrough characteristic. When the resonator is operated in air under the action of Q-control, the primary driving voltage and the corresponding feedthrough signal will be small. However, a large feedback voltage acting to cancel out the effect of damping and increase the effective Q of the system will also be present. Consequently, a large feedthrough signal will be attributed to this voltage.

A model has been developed to describe the behaviour of the system under the influence of velocity feedback in the presence of a feedthrough signal. In the model, two possible feedback configurations were considered. In the analysis below, the parameter $s = \pm 1$ is used to differentiate between the two possible situations. When s =1 the feedback is applied such that the feedback voltage is in phase with the primary driving voltage. The overall driving voltage is $V_{DC} + V_{AC} + V_{FB}$, leading to an increase in the effective Q. Conversely, when $s = -1$ the driving voltage is $V_{DC} + V_{AC} - V_{FB}$ and the feedback force will contribute to the damping force and the effective Q is expected to decrease.

The voltage at the output of the instrumentation amplifier stage of the test PCB is ideally proportional to the instantaneous velocity, $V_{INA} = 2G_{INA}RV_s\frac{dC}{dx}\frac{dx}{dt}$. The addition of a feedthrough signal due to the combination of both the primary driving voltage and the feedback voltage modifies the voltage at the output of the instrumentation amplifier as follows,

$$V_{INA} = 2G_{INA}R\left(V_s\frac{dC}{dx}\dot{x} \pm sV_{FB}j\omega C_{eff} \pm V_{AC}e^{j\omega t}j\omega C_{eff}\right). \tag{4.1}$$

C_{eff} models the effective capacitance between drive and readout channels. The polarity of the voltage contributions in Equation (4.1) is determined by the polarity of the primary driving voltage applied to the dominant bonding wire. In this example the feedthrough is dominated by the voltage applied to the negative driving comb, this means the the output voltage from the instrumentation amplifier will be

$$V_{FB} = 2G_{INA}RLe^{j\psi}\left(V_s\frac{dC}{dx}\dot{x} - sV_{FB}j\omega C_{eff} - V_{AC}e^{j\omega t}j\omega C_{eff}\right). \tag{4.2}$$

In this equation, the frequency-dependent gain around the feedback loop is L and $e^{j\psi}$ has been included to model the total frequency-dependent phase change in the readout and feedback electronics (ψ). Rearranging gives

$$V_{FB} = \frac{V_s\frac{dC}{dx}\bar{L}\dot{x} - V_{AC}e^{j\omega t}j\omega C_{eff}\bar{L}}{1 + sj\omega C_{eff}\bar{L}}, \tag{4.3}$$

where $\bar{L} = 2G_{INA}RLe^{j\psi}$. The final equation describing the voltage at the output of the instrumentation amplifier is obtained by multiplying Equation (4.3) by its complex conjugate

$$V_{FB} = \frac{V_s \frac{dC}{dx}\bar{L}\dot{x} + sV_s\frac{dC}{dx}C_{eff}\left(\omega\bar{L}\right)^2 x - V_{AC}e^{j\omega t}\left(j\omega C_{eff}\bar{L} + s\left(\omega C_{eff}\bar{L}\right)^2\right)}{1+\left(\omega C_{eff}\bar{L}\right)^2}. \tag{4.4}$$

Note that in the above equation, setting C_{eff} =0 restores the feedback voltage to the desired form. Under the action of feedback, the equation of motion is

$$\ddot{x} + \frac{\omega_0}{Q}\dot{x} + \omega_0^2 x = F_D e^{j\omega t} + sF_{FB}, \tag{4.5}$$

$$\ddot{x} + \frac{\omega_0}{Q}\dot{x} + \omega_0^2 x = F_D e^{j\omega t} + s\frac{2V_{DC}V_{FB}}{m}\frac{dC}{dx}. \tag{4.6}$$

Substituting Equation (4.4) into Equation (4.6) gives the equation of motion of the system under the influence of the feedthrough-dependent feedback voltage

$$\ddot{x} + \frac{\omega_0}{Q}\dot{x} + \omega_0^2 x = F_D e^{j\omega t}(1-\sigma) + \xi\dot{x} + \chi x, \tag{4.7}$$

where σ, ξ and χ are frequency-dependent constants,

$$\sigma = \frac{sj\omega C_{eff}\bar{L} + \left(\omega C_{eff}\bar{L}\right)^2}{1+\left(\omega C_{eff}\bar{L}\right)^2}, \tag{4.8}$$

$$\xi = \frac{2V_{DC}}{m}\frac{dC}{dx}\left(\frac{sV_s\frac{dC}{dx}\bar{L}}{1+\left(\omega C_{eff}\bar{L}\right)^2}\right), \tag{4.9}$$

$$\chi = \frac{2V_{DC}}{m}\frac{dC}{dx}\left(\frac{V_s\frac{dC}{dx}C_{eff}\left(\omega\bar{L}\right)^2}{1+\left(\omega C_{eff}\bar{L}\right)^2}\right). \tag{4.10}$$

Note once again that setting C_{eff} =0, sets σ and χ to zero and reduces ξ to the desired form. Finally, from Equation (4.7) the transfer function of the modified system is

$$\hat{\hat{G}} = \frac{j\omega(1-\sigma)}{\omega_0^2 - \chi - \omega^2 + j\omega\left(\frac{\omega_0}{Q} - \xi\right)}. \tag{4.11}$$

The model described by Equation (4.11) can be used to predict the behaviour of the system when the magnitude of the undesirable feedthrough signal is similar in magnitude to the velocity-dependent signal produced by the readout electronics. Equation (4.11) has been solved for typical parameter values over a wide frequency range. Figure 4.7 shows the predicted behaviour of the system under the action of velocity feedback in the presence of a feedthrough signal. The figure shows that when the feedback voltage is in phase with the

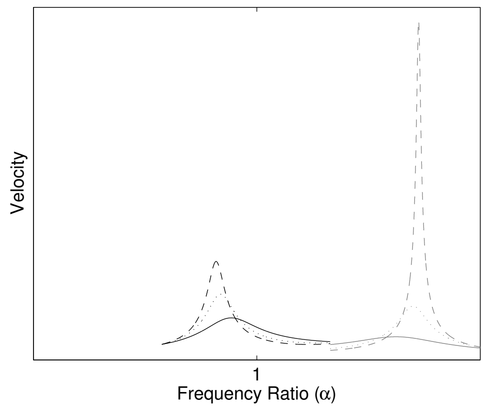

Figure 4.7: Simulation showing the effect of increasing the feedback level (low feedback fraction (solid) to high feedback fraction (dashed)) on the velocity response for s =1 (black) and $s = -1$ (grey).

primary driving voltage (s =1), the quality factor increases. However, the resonant frequency is also decreased which is an undesirable feature of the response. The simulation also shows that when the feedback voltage is 180° out of phase with respect to the primary driving voltage ($s = -1$), both the resonant frequency and the Q are increased. This result is counter-intuitive, as when the feedback is connected in this configuration the standard model for Q-enhancement predicts that a damping force is added to the system, resulting in a decrease in Q. These results show that due to the presence of a large feedthrough signal, the predicted response of the system under the action of force feedback is significantly different from the typical behaviour of a resonant system when the Q is increased.

Experiments were performed to confirm that the resonator behaves in the same way as predicted by Equation (4.11). The resonator was tested in both feedback configurations with a small AC driving voltage (60mV$_{pp}$). The DC component was 7.2V and for this resonator the resonant frequency is approximately 17kHz for these bias conditions. The phase of the

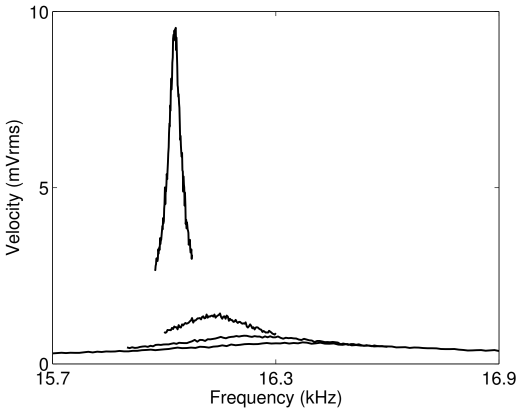

Figure 4.8: Velocity response in air, showing the effect of capacitive feedthrough on resonant frequency (s =1).

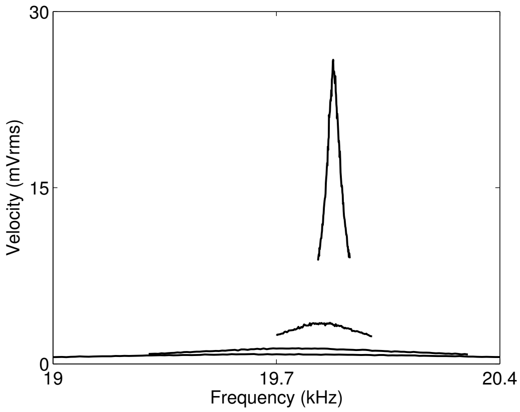

Figure 4.9: Velocity response in air, showing the effect of capacitive feedthrough on resonant frequency ($s = -1$).

feedback voltage was altered by 180° using an inverting amplifier to change the sign of s. Figures 4.8 and 4.9 show that when the feedback fraction was increased, the measured resonant frequency approached 16kHz when s =1 and 20kHz when $s = -1$. Furthermore, in both configurations the Q of the system was increased. These results show that the characteristics of the measured response are the same as those predicted by Equation (4.11) for the resonator under the influence of Q-control in the presence of a feedthrough signal.

4.3.3 Feedthrough compensation

Results in the previous section show that the effect of the feedthrough signal on Q-enhancement is to introduce a complex relationship between the feedback gain and the observed resonant frequency of the system. The significance of this is that the observed resonant frequency will be determined by the feedback level. This means that predicting the observed resonant frequency of a Q-enhanced mass sensor will be difficult. Therefore in this section a method for removing the undesirable feedthrough signal by direct cancellation is described [2, 69, 70].

To compensate for the coupling capacitance between the drive and readout channels, a voltage equal to $\pm(V_{AC} + sV_{FB})$ can be applied to a dummy capacitor (C_d) connected to each transimpedance amplifier in the readout electronics. By tuning the gain (G_d) of the compensation voltage, or the size of the dummy capacitor, it is possible to generate a current in each readout channel that is equal in magnitude to the undesirable current due to capacitive feedthrough. Figure 4.10 shows the electrical configuration for compensation of the full differential readout architecture. The variable capacitors in Figure 4.10 represent the moving comb

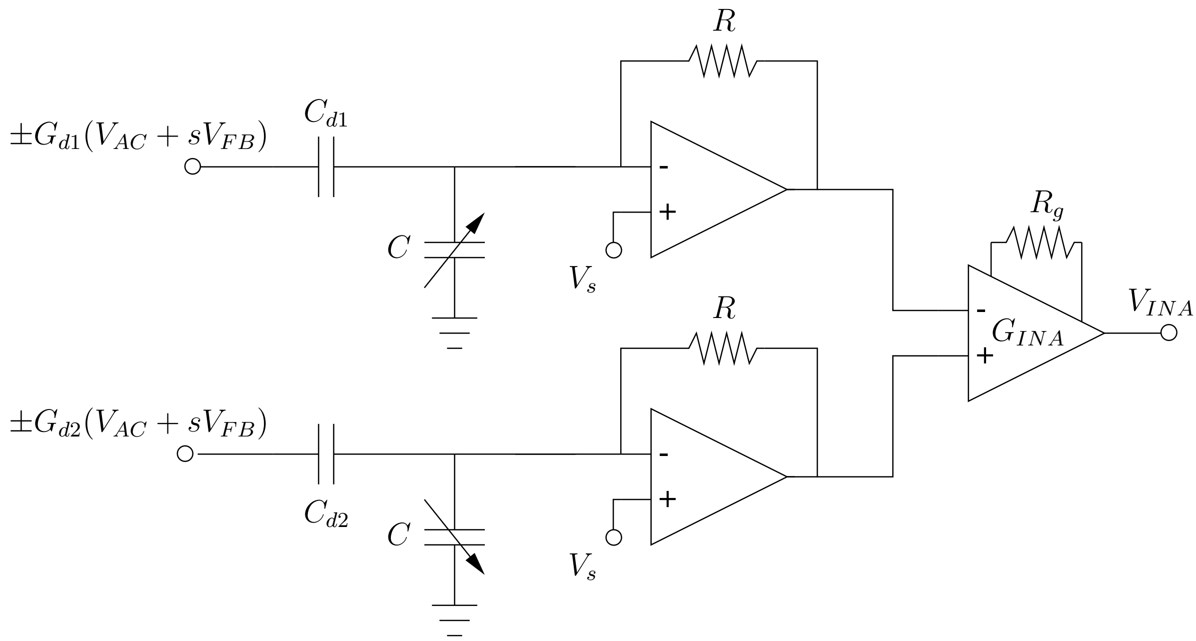

Figure 4.10: Circuit for direct cancellation of feedthrough current using dummy capacitances.

capacitors. To ensure that the current in the dummy capacitor acts to cancel the undesirable feedthrough current, the voltage applied to the dummy capacitor must be the opposite polarity to the voltage applied to the bonding wire that dominates the feedthrough characteristic. In this example the dominant bonding wire is connected to the negative driving voltage and the current generated in a single readout channel is

$$i = \pm V_s \frac{dC}{dx}\dot{x} + j\omega(V_{AC} + sV_{FB})(G_d C_d - C_{eff}). \tag{4.12}$$

In practice, tuning the compensation circuit is simpler to achieve by varying G_d as opposed to C_d. Because of this, the magnitude of dummy compensation capacitance was fixed. The dummy capacitance was formed between two adjacent copper tracks on a strip of Veroboard. The channel is compensated when $G_d C_d = C_{eff}$. To set the gain of the system the driving DC bias was removed to eliminate the driving force and to prevent the device from moving. A large differential AC voltage was then applied to the resonator. Each readout channel was independently tuned by varying the gain of the corresponding compensation circuit (G_d) until the feedthrough signal in the readout channel was removed. This is easy to achieve in practice by monitoring the FFT showing the frequency content of the readout current and monitoring the power at the applied test frequency.

Figure 4.11 shows that using this technique, the observed feedthrough signal is reduced by approximately two orders of magnitude. Consequently, the current due to capacitive feedthrough will now be significantly smaller than the typical current proportional to the resonator velocity. This means that Equation (4.11) effectively reduces to the ideal form ($C_{eff} \approx 0$) for a Q-enhanced resonant system. Equation (4.13) is the transfer function describing the compensated system

$$\hat{\hat{G}} = \frac{j\omega}{\omega_0^2 - \omega^2 + j\omega\left(\frac{\omega_0}{Q} - \xi\right)}. \tag{4.13}$$

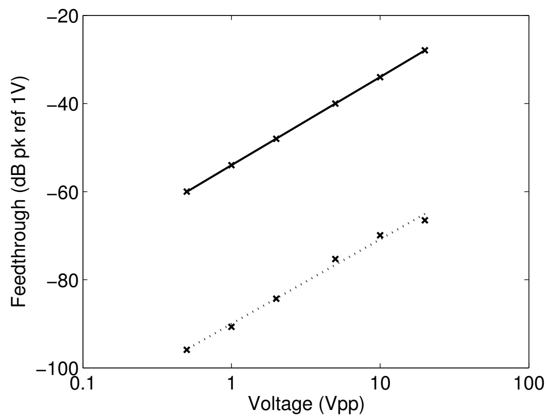

Figure 4.11: Feedthrough levels for differential mode driving configurations when the resonator is tested without feedthrough compensation (solid), with compensation (dotted).

4.3.4 Phase change introduced by the readout electronics

In the previous section a technique has been described that can be used to reduce the undesirable feedthrough signal that occurs when the AC component of the overall driving voltage applied to the resonator is large. Results have shown that the technique reduces the measured feedthrough voltage by two orders of magnitude. The resulting system is modelled by Equation (4.13), which describes the velocity response of the resonator under the action of force feedback after feedthrough compensation.

Equation (4.13) appears ideal for a Q-enhanced system because ξ will partially cancel the damping term ($\frac{\omega_0}{Q}$) resulting in a rise in the effective Q. However, any phase change in the readout electronics means that ξ will be both complex and frequency-dependent. To take this into account, Equation (4.13) was modified to give

$$\hat{\dot{G}} = \frac{j\omega}{\omega_0^2 + \omega\Im(\xi) - \omega^2 + j\omega\left(\frac{\omega_0}{Q} - \Re(\xi)\right)}, \tag{4.14}$$

where

$$\Re(\xi) \quad = \quad \frac{4sV_{DC}V_sG_{INA}RL}{m}\left(\frac{dC}{dx}\right)^2\cos\left(\psi(\omega)\right), \tag{4.15}$$

$$\Im(\xi) \quad = \quad \frac{4sV_{DC}V_sG_{INA}RL}{m}\left(\frac{dC}{dx}\right)^2\sin\left(\psi(\omega)\right). \tag{4.16}$$

Equation (4.14) shows that depending upon the sign of ψ the resonant frequency will be either increased or decreased by the action of Q-control when the phase shift around the feedback loop is finite. The significance of this result is that even though the feedthrough signal has been removed by the compensation technique described in the previous section, because of the phase change in the readout electronics the effect of Q-control will be to alter the resonant frequency of the prototype resonator.

The phase change introduced by the readout electronics and the bandpass filter in the feedback loop is frequency-dependent. In addition, because of the presence of the filter, the gain in the feedback loop is also determined by the operating frequency. To model the system by solving Equation (4.14), it is necessary to characterise this frequency-dependent gain and phase shift in the readout electronics. Figures 4.12 and 4.13 show the measured maximum loop gain (L_{max}) and phase shift (ψ) in the feedback loop respectively. From these figures the following equations describing L_{max} and ψ have been determined

$$L_{max} = 9.6\times10^{-12}\omega^3 - 3.6\times10^{-6}\omega^2 + 450\times10^{-3}\omega - 17\times10^3, \tag{4.17}$$

$$\psi = 610\times 10{-}12\omega^2 - 220\times10^{-6}\omega + 10. \tag{4.18}$$

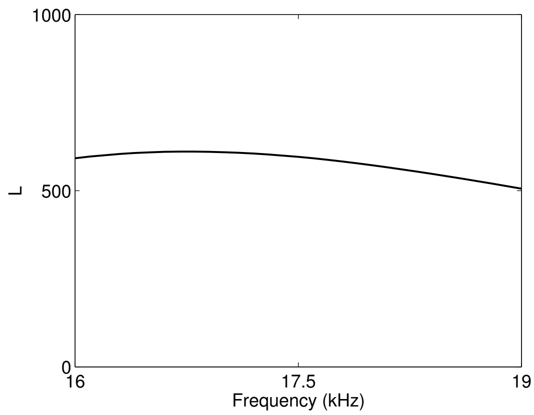

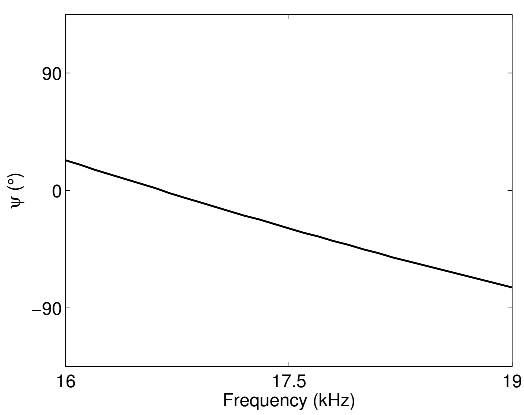

Figure 4.12: Variation of feedback loop gain (L) with frequency.

Figure 4.13: Variation of phase change in the feedback loop (ψ) with frequency.

The relationships described by Equations (4.17) and (4.18) can be used to evaluate Equation (4.14) over a wide range of operating frequencies. This means that it will be possible to test the performance of the system when Q-control is used and then to compare the observed response with the response predicted by (4.14).

4.3.5 Atmospheric pressure testing

The performance of Q-control was tested when the sensor was exposed to air at atmospheric pressure. Before applying the feedback force to increase the effective Q, the feedthrough signal was removed and a DC driving voltage of 7.2V was applied to the resonator. The AC component of the driving voltage was 60mV_{pp}. In the previous section, Equation (4.14) showed that the magnitude of the change in resonant frequency caused by Q-enhancement is controlled by $\Im(\xi)$. Solving Equation (4.18) shows that at the resonant frequency of the device under test, the total phase change around the feedback loop is approximately 15° lagging. This means that $\Im(\xi)$ is negative and will act to reduce the resonant frequency.

Figures 4.14 and 4.15 show the velocity and phase responses, respectively, of the resonator under the action of Q-control. The resonant peak was observed at 16770Hz. As predicted this value is lower than the theoretical resonant frequency for these bias conditions (17042Hz, from Equation (3.16)). Figure 4.14 shows that the effective Q has been increased to approximately 850 corresponding to λ =0.995 (from Equation (1.16)).

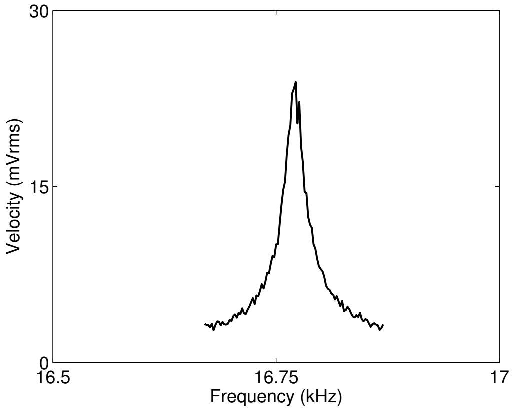

Figure 4.14: Velocity response of the feedthrough compensated system when the effective Q is 850.

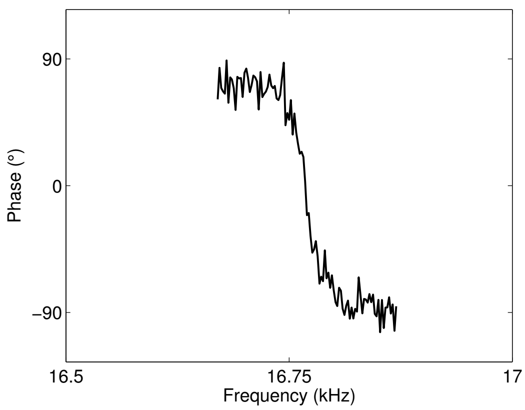

Figure 4.15: Phase response of the feedthrough compensated system when the effective Q is 850.

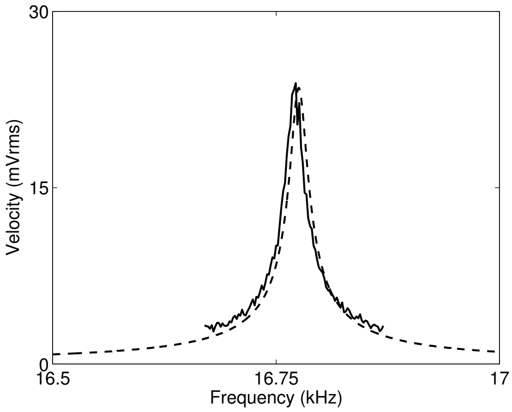

Figure 4.16: Observed (solid) and simulated (dashed) velocity response of the system under the action of Q-control.

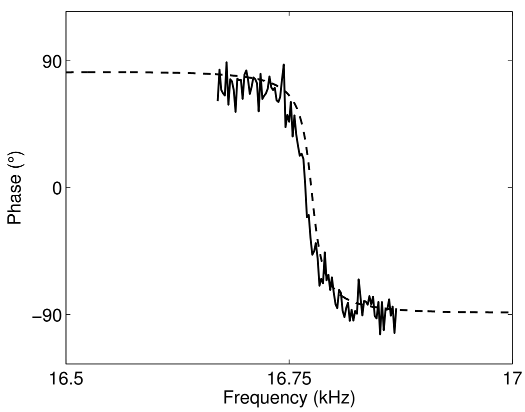

Figure 4.17: Observed (solid) and simulated (dashed) phase response of the system under the action of Q-control.

Equation (4.14) has been evaluated over a range of frequencies to simulate the observed response of the resonator. Figures 4.16 and 4.17 show comparisons between the measured and simulated responses of the velocity and phase of the resonant system. The figures show that there is a close match between the simulated (dashed) and measured (solid) responses of the resonator. This confirms that the model of the feedback system that has been developed (Equation (4.14)) accurately describes the behaviour of the system. The key conclusion of these experiments is that Q-control increases the effective Q of the system, however as predicted in the previous section the presence of any phase change in the readout electronics can alter the resonant frequency. The magnitude of the phase change in the readout electronics will determine the size of this change in frequency. At the resonant frequency of the resonator that has been tested, the phase change in the feedback loop is lagging. Because the phase of the feedback force lags the resonator's velocity, Q-enhancement has caused the resonant frequency of the resonator to reduce.

4.3.6 Limitations of Q-control

Q-control has been used to increase the effective Q of the prototype resonator by over two orders of magnitude when the resonator was exposed to air at atmospheric pressure. However, results and analysis have shown that the resonant frequency of the resonator is also influenced by Q-control. This is because of the finite phase shift in the feedback loop. The characteristics of the filter in the feedback loop determine the magnitude of this frequency-dependent phase shift. To minimise the phase shift, the characteristic frequency of the bandpass filter was set close to the typical resonant frequency of test samples. Unfortunately, a filter with a characteristic frequency very close to the resonant frequency of one test sample, will introduce a large phase shift when used with a sample with a different resonant frequency. Because of this, a problem with the system that has been developed is that variability in the resonant frequency between samples will affect Q-enhancement.

A further limitation of Q-control by velocity feedback is that practical experience has shown that the performance of the system is particularly susceptible to noise and interference from other electronic circuits. The effect of this is to generate amplitude noise in the observed velocity signal, which degrades the performance of the system. It is possible to significantly reduce this effect by shielding the test PCB and feedback electronics. Fortunately, integrating the architecture that has been developed in microelectronics is expected to significantly reduce this problem.

4.4 Summary

In this chapter, the quality factor of the prototype resonant system has been increased using feedback. The feedback force that has been generated is directly proportional to the velocity of the resonator and acts to cancel out the effect of air damping. Simple electronic circuits using op-amps were used to amplify the velocity-dependent signal at the output of the test PCB and add the resulting signal to the primary driving signal. When the MEMS resonator was operated in air at atmospheric pressure, a bandpass filter was used in the feedback loop to significantly improve the signal to noise ratio of the measured velocity signal.

The feedthrough signal caused by the large AC driving voltage component that is required to excite the resonator at atmospheric pressure was similar in magnitude to the observed velocity signal. A side effect of the presence of feedthrough is that the resonant frequency of the system is affected when Q-control is implemented. To remove the effect of feedthrough, the undesirable signal was cancelled using a dummy capacitance to generate a current equal and opposite to the feedthrough current contribution. Despite this, experiments and analysis show that due to the finite change in phase the feedback loop, the resonant frequency of the system is still altered in addition to the desired Q-enhancement.

Because the phase characteristic of the feedback loop is dominated by the bandpass filter, the centre frequency of the filter should ideally match the resonant frequency of the sample under test. In this way, the phase change experienced by the velocity-dependent feedback signal will be small. However, the bandpass filter that has been implemented comprises op-amp circuits and passive components. Consequently, the filter can not be easily tuned to accommodate the typical range of resonant frequencies of the prototype resonators. Furthermore, the system that has been developed can not be used to test resonators with different nominal resonant frequencies. This is because tuning the filter response requires changing resistor or capacitor values, which will not be possible in the eventual microelectronic system.

Chapter 5

Resonant frequency tracking hardware

5.1 Introduction

In the previous chapter, the use of velocity feedback to increase the effective Q of the prototype resonant system was described. A key component in the system that has been implemented is a filter in the feedback loop which is used to reduce the noise present in the relatively small velocity signal that occurs when the resonator operates at atmospheric pressure. Analysis and results show that when velocity feedback is implemented, feedthrough from the drive to readout electronics causes an undesirable relationship between the resonant frequency of the system and the feedback gain. Even when the feedthrough signal is removed by direct cancellation, analysis and experiments show that any change in phase experienced by the signal in the feedback loop also affects the resonant frequency.

In this chapter, hardware to automatically monitor the resonant frequency of a typical MEMS sample is described. To create a system that is compatible with Q-enhancement, one requirement of the hardware is the ability to tune the centre frequency of the filter in the feedback loop to match the resonant frequency of the particular resonator. Direct digital synthesis is used in order to generate accurate and programmable driving signals. To test the system that has been designed, it is possible to use a DC bias voltage in order to simulate a change in mass of the resonator by reducing its effective spring constant.

5.2 PLL-based resonance detection

To build a system designed to automatically monitor the resonant frequency of a MEMS resonator, a simple and convenient method can be implemented using a phase-locked loop circuit. A typical PLL consists of three basic functional blocks. A Voltage-Controlled Oscillator (VCO), a Phase Detector (PD) and a Loop Filter (LF) arranged as shown in Figure 5.1. The phases of the signal from the VCO and the input to the PLL are compared by the phase detector. The output of the PD is a function of the phase difference between its input signals and is subsequently filtered by the loop filter. When the loop is locked, the output of the LF will be a DC voltage and because this controls the VCO, the output frequency from the VCO will be constant and at the same frequency as the input frequency [71].

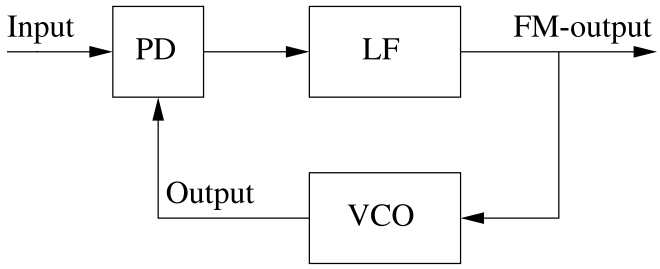

Figure 5.1: Block diagram showing the functional blocks in a simple phase-locked loop.

When monitoring the velocity of a resonant system, the phase difference between the driving signal and the velocity at the resonant frequency is always 0°. This means that the resonant frequency of a resonator can be tracked using a PLL that gives a zero phase error between the incoming signal and the output signal when the loop is locked. To do this, the output of the VCO will be amplified to form the AC component of the primary driving voltage. In addition, the measured velocity signal obtained from the readout electronics must be connected to the input of the PLL. In this way, the control voltage to the VCO can be used as a simple indicator for measuring and tracking changes in the resonant frequency of the system.

5.3 Tracking system hardware

5.3.1 Direct digital frequency synthesis

In a simple phase-locked loop circuit, the range of frequencies that can be tracked is largely determined by the rate of change of frequency with respect to the VCO input voltage. This relationship is the gain of the VCO. To enable accurate location of the resonant frequency of a resonator using a phase-locked loop circuit, ideally the VCO gain should be low. In this way a small change in frequency of the VCO requires a large change in control voltage, resulting in a good detection resolution. Unfortunately, due to the limited voltage range in any real system, the desire for a low VCO gain inevitably limits the range of frequencies that it is able to produce. This means that there is a trade-off between sensitivity and the ability to tolerate uncertainty in the resonant frequency of resonators.

Ideally, this tracking system should be compatible with a wide range of resonator designs and should also tolerate typical variations in resonant frequency between samples with the same nominal resonant frequency. This can be achieved using a VCO that produces a narrow range of frequencies and then tuning the frequency range to suit the particular resonator. A problem with this approach is that the frequency range of a VCO is often controlled by changing external resistors or capacitors which are connected to an integrated circuit containing the VCO. It is possible to change resistors or capacitors on a sample-by-sample basis, however in practice this is undesirable. Furthermore, if the system is to be implemented in a microelectronic design and packaged as a single integrated circuit, changing a component is impossible.

A convenient method of generating a variable frequency to a high accuracy is to use an integrated direct digital frequency synthesis chip. The key benefit offered by this approach is the ability to program the operating frequency digitally. This creates a very flexible solution that is inherently compatible with the requirement to design an electronic system that can be fully integrated. An AD9833 integrated circuit manufactured by Analog Devices has been used as the programmable VCO in this system. Figure 5.2 is a schematic diagram showing the arrangement of the AD9833 and its additional interface electronics. The data sheet for the

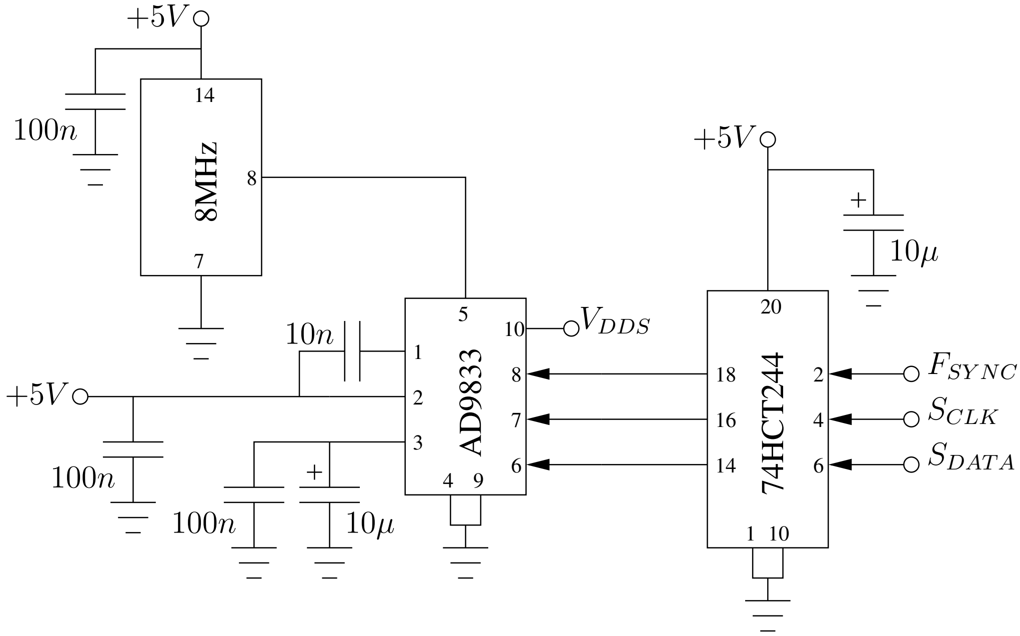

Figure 5.2: Schematic diagram showing configuration for using AD9833 programmable waveform generator with 74HCT244 line driver and clock.

AD9833 suggests the use of a 74HCT244 line driver integrated circuit to buffer logic signals which must be provided by a controller.

The AD9833 is a programmable waveform generator and the frequency and phase are software programmable which enables easy and precise tuning. The frequency register is 28-bits wide and when clocked with an 8MHz signal the frequency resolution is 30mHz. This means it is able to produce discrete frequencies spaced at 30mHz from DC up to 8MHz. The frequency and phase words are stored in internal registers in the AD9833. To program the waveform generator, these registers are updated using a 3-wire serial interface to a controller which provides the frequency, phase and timing signals. The serial interface supports clock speeds of up to 40MHz and it is theoretically possible to update the frequency and phase registers consecutively at a maximum rate of approximately 50 times per cycle of oscillation.

5.3.2 Analogue-to-digital conversion

The VCO that has been chosen for this system is programmed by supplying a 28-bit frequency word. To determine the frequency word, it is necessary to sample the analogue voltage at the output of the loop filter using an ADC and to map the resulting digital word to the frequency register in the VCO. It is possible to obtain ADCs with up to 24-bit resolution from suppliers such as Analog Devices, although there is a compromise on bandwidth or cost. However, it is possible to use a general purpose ADC with between 8-bit and 16-bit resolution and to map the output of the ADC to the LSBs of the VCO frequency control word. To illustrate this, consider mapping the 14-bit output from an AD7367 ADC integrated circuit (manufactured by Analog Devices) to the LSBs of the AD9833 frequency register. This number of bits addresses a bandwidth of approximately 500Hz. By appropriate choice of the Most Significant Bits (MSBs) of the frequency word, the output of the ADC can be mapped to any frequency window between DC and 8MHz.

The AD7367 has been chosen for this system because it is low-cost and has a maximum sample rate of 1MSs^{-1}. Furthermore, the AD7367 also uses a 3-wire serial interface and so it will be possible to use the same communications protocol for both the ADC and the VCO. Figure 5.3 is a schematic diagram showing the AD7367 configured to sample in the voltage range between 0V and 10V. Practical experience has shown that decoupling capacitors must be placed close to the AD7367 integrated circuit. To achieve this, a small PCB was fabricated to provide better layout flexibility than is possible when using Veroboard.

5.3.3 System controller

In sections 5.3.1 and 5.3.2, a programmable waveform generator and an analogue-to-digital converter which form the key components of a phase-locked loop tracking system have been described. Both components must be controlled using a 3-wire serial interface from a separate controller. The exact specifications for the system controller are not crucial, however the maximum serial clock frequency of the AD9833 of 40MHz means that ideally the clock frequency of the controller should be at least equal to this frequency.

The controller could be implemented using a Programmable Integrated Circuit (PIC), however a Field-Programmable Gate Array (FPGA) has the ability to process programs in parallel, offering increased flexibility over a PIC. Therefore to control the waveform generator and the ADC, a Xilinx Spartan-3 XC3S200 FPGA mounted on a Spartan-3 Starter Kit board was used. The clock speed of the FPGA is set by a 50MHz oscillator on the board, which is suitable for this application.

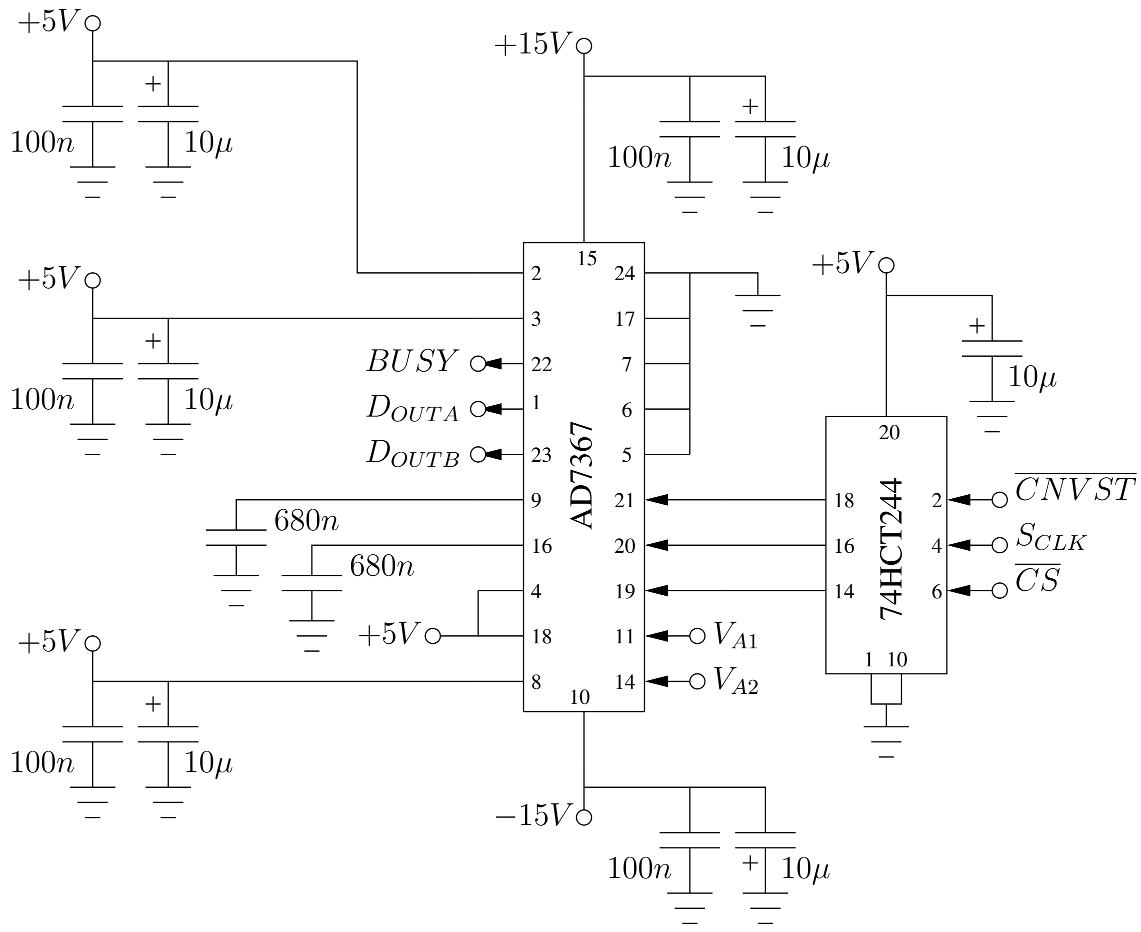

Figure 5.3: Schematic diagram showing the configuration for using the AD7367 ADC with a 74HCT244 line driver and arrangement of decoupling capacitors.

5.3.4 Phase detector

The choice of phase detector implemented in a PLL determines if the final phase error is reduced to zero or to a finite value. This tracking system is required to identify the resonant frequency of a MEMS resonator, corresponding to the frequency where the phase difference between the primary driving force and the measured velocity is 0°. Consequently, using a phase detector designed to reduce the final phase error to zero is paramount. Two obvious choices for consideration for use as the phase detector are an Exclusive Or (EXOR) gate and the Phase-Frequency Detector (PFD), both of which are included in the popular 4046B micro-power phase-locked loop integrated circuit.

The operation of the EXOR phase detector is simple, when both inputs are 90° out of phase, the output of the PD is a square wave whose frequency is twice the reference frequency and with a duty cycle of exactly 50%. After the loop filter, a DC voltage representing the average value of the PD output remains. It follows that when the two signals are exactly in phase the average value at the output of the LF is zero and that when there is a phase difference of 180° the output of the LF takes the maximum value. Hence the EXOR phase detector can maintain phase tracking when the phase error (ϕ_e) is in the range

$$0^\circ \leq \phi_e \leq 180^\circ. \tag{5.1}$$

The problem with the EXOR phase detector, however, is that the phase error is only reduced to zero when the VCO operates at its minimum frequency which will not necessarily match the exact resonant frequency of the MEMS structure.

To avoid the problem described above it is possible to use the phase-frequency detector, which reduces the phase error to zero over the entire frequency range of the VCO. The PFD is a digital memory network comprising four flip-flop stages, control gating and a tri-state output [67]. When the inputs are the same frequency and the primary input is lagging the secondary input, the output of the PFD is high between the positive edges of the signals. Similarly, when the primary input is leading the secondary input, the output of the PFD is low between the positive edges of the signals. At all other times the output of the PFD is in high-impedance mode. In this way, the voltage stored on a capacitor contained in the loop filter is constantly adjusted until the incoming signal and VCO output are the same frequency and exactly in phase. At this time the output of the PFD remains in high-impedance mode and the voltage on the capacitor in the loop filter will remain constant at value that is determined by the frequency of the incoming signal.

The PFD facilities the implementation of a PLL that stabilises with zero phase error over a wide range of frequencies. As the input signals to the PFD are always square waves, it is necessary to convert the incoming velocity signal from a sine wave into a square wave. Similarly, the output from the programmable VCO is a square wave and it can be connected directly to the input of the phase-frequency detector. In this system a 4046B integrated circuit has been used because it contains a PFD. In an integrated system, the PFD can be easily fabricated without the unused circuitry in the 4046B chip.

5.3.5 Tunable bandpass filter

In section 4.3.4, the effect of phase change in the readout electronics and feedback loop on Q-enhancement was described. Analysis showed that due to the finite change in phase incurred by the velocity signal, a side effect of force feedback is to alter the resonant frequency of the resonator under test. To eliminate the resulting complicated relationship between the resonant frequency and the level of feedback, the undesirable change in phase caused to the velocity signal by the electronics should ideally be removed. Therefore a key design requirement of this system is the ability to tune the centre frequency of the bandpass filter in the feedback loop, without the need to change components.

In the experiments described in chapter 4, an 8^{th} order bandpass filter was used to filter and amplify the small velocity signal to generate the feedback voltage required for Q-enhancement. The overall filter comprised four cascaded 2^{nd} order Sallen and Key circuits each containing an op-amp and passive components to determine the response of the filter stage. Component values were chosen in order to place the centre frequency of the bandpass filter close to the resonant frequency of a typical resonator. However, due to variations in the resonant frequency between the manufactured resonators, the output velocity signals for different samples experience a different change in phase. This causes the behaviour of a resonator to depend upon its resonant frequency when Q-control is implemented. Furthermore, the filter that has been implemented is not compatible with resonators that have a different nominal resonant frequency.

This problem can be avoided by replacing the Sallen and Key filter used previously, with an inexpensive and widely available switched-capacitor filter integrated circuit. The key advantage of a switched-capacitor filter for this application is the ability to tune the filter's characteristic frequency simply by changing the frequency of a clock input [67]. This provides the ability to tune the centre frequency of the bandpass filter to the exact frequency of the resonator under test, without the need to alter any component values. The MF10 manufactured by National Semiconductor is a popular switched-capacitor filter package. However the LMF100 integrated circuit, a pin-compatible device which is also manufactured by National Semiconductor, has a wider bandwidth and was used for this system.

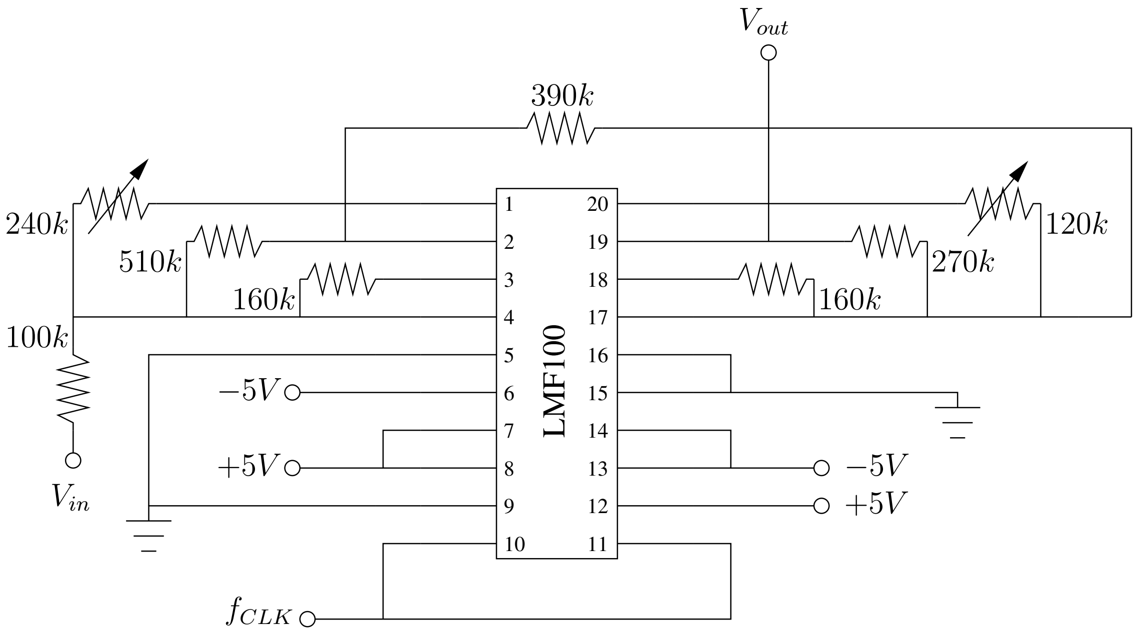

Figure 5.4: A 4$^{\text{th}}$ order bandpass switched-capacitor filter using a single LMF100 integrated circuit, with variable centre frequency of $f_{CLK}/50$.

The LMF100 consists of two independent general purpose switched capacitor filters. Various first-order and second-order filters can be implemented using each filter block and this means that a single LMF100 IC can be used to build a 4$^{\text{th}}$ order filter. Figure 5.4 shows a schematic diagram of a 4$^{\text{th}}$ order filter, higher order filters can be implemented by simply cascading additional packages and for this system two LMF100 ICs were used to build an 8$^{\text{th}}$ order filter. Using the resistor values shown in Figure 5.4, the gain of the overall 8$^{\text{th}}$ order filter is approximately five and its Q is approximately three, which is similar to the previous op-amp filter. Once again, a filter with a narrower passband was not implemented in order to limit the phase change introduced by the filter when the driving frequency is slightly different to the centre frequency of the filter. The resistors between pins 1(20) and 4(17) are variable to enable tuning of the filter response to give a maximally flat response in the passband. The output of the filter is further amplified by a series of simple op-amp circuits providing a maximum gain of approximately 200.

Figure 5.5 shows the phase change ψ_t in the feedback loop, with the filter set to its arbitrary centre frequency (f_{tc} =15.3kHz). Describing the phase change in the feedback loop requires care as it is a function of both the operating frequency and the current centre frequency, f_t, of the filter. The difference between the arbitrary centre frequency and the current centre

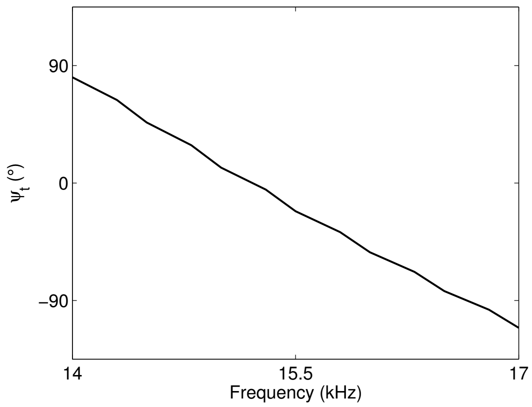

Figure 5.5: Variation of the phase change (ψ_t) in feedback loop with frequency.

frequency of the filter is $\Delta\omega_t$,

$$\Delta\omega_t = 2\pi \times (f_{tc} - f_t). \tag{5.2}$$

The expression for the phase change in the feedback loop is then given by

$$\psi_t = 1.6 \times 10^{-9}(\omega + \Delta\omega_t)^2 - 480 \times 10^{-6}(\omega + \Delta\omega_t) - 2.1 \times 10^{-6}\omega + 32. \tag{5.3}$$

Using the tunable filter that has been described in this section it is possible to limit the phase shift introduced by the readout electronics at resonance to less than 1° and this means that the impact on the resonator is negligible.

5.4 Phase-locked loop implementation

Figure 5.6 is a block diagram showing the configuration of the key components in the tracking system that has been designed. The inputs to the phase-frequency detector in this system must be digital signals. This means that it is necessary to transform the sinusoidal velocity signal from the output of the tunable bandpass filter and amplification stage into a square wave. A convenient method of achieving this is using an LM392 voltage comparator. For the other input to the PFD, the waveform generator was programmed to produce a square wave output. After scaling the square wave signal appropriately, this square wave also forms the AC component in the primary driving force (V_{AC}). The PLL loop filter is a simple first-order low-pass Resistor-Capacitor (RC) filter with a cut-off frequency off 100Hz. This characteristic

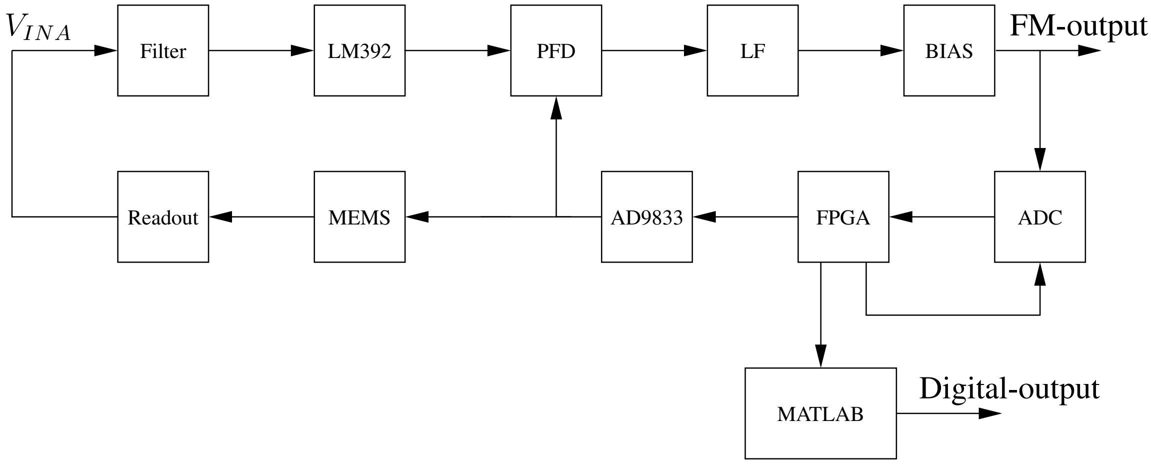

Figure 5.6: Block diagram showing the arrangement of hardware in the phase-locked loop tracking system.

frequency was chosen to give a compromise between noise rejection and transient response.

To control the system, a VHSIC Hardware Description Language (VHDL) program was programmed into the FPGA. The structure of the program comprises three main states, *run*, *reset* and *Espring_state*. Also implemented are processes running in parallel, used for secondary tasks such as streaming data through the serial port to MATLAB (for debugging and measurement purposes) or timing and filtering circuits. After receipt of a 'start' signal the system enters the reset state during which the control registers in the waveform generator are initialised. When the system is running, the 10 MSBs from the ADC are mapped to the 10 LSBs of the frequency control word. The appropriate frequency offset is set to the MSBs of the control word and the frequency register in the AD9833 is then updated. The four LSBs of the ADC output word corresponding to voltages less than 10mV are discarded. This is because below this level the voltage at the output of the loop filter is dominated by noise. The frequency control word is updated approximately once per cycle of the resonator and is digitally filtered with a 32-tap moving average filter. This digital filter has a characteristic frequency of approximately 500Hz, designed to remove digital noise artefacts.

5.5 Frequency control

To test the tracking system, a method for varying the resonant frequency of a resonator by a known amount is essential. It is possible to easily reduce the effective spring constant of the system by applying a DC bias voltage to a comb capacitance (as described in section 3.7). This is a sensible approach for testing the system because reducing the spring constant results in an apparent increase in resonator mass. Unfortunately, the differential driving and readout architecture requires the use of all four comb capacitances. Altering the bias applied to any of these combs will change either the driving force or the readout voltage. Furthermore, if Q-control is used, this will also be affected because the feedback force is a function of both V_{DC} and V_s (Equation (4.15)). This means that a free comb capacitance is required to facilitate independent control of the resonant frequency. The only methods of achieving this are either using a single drive comb and direct drive, or a single readout channel instead of differential readout.

The velocity signal measured at the output of the readout electronics is small when the resonator operates at atmospheric pressure and this means that reducing the magnitude of the driving force or the gain of the readout electronics is undesirable. Implementing either direct drive or single-ended readout will halve the output signal strength. Fortunately, it is possible to compensate for this by increasing the effective DC drive and readout bias voltages, V_{DC} and V_s. This was achieved by changing the bias voltage applied to the movable part of the resonator structure from 0V to -5V. The DC bias in the driving force was then set to 5V, giving V_{DC} =10V. The resonator was operated with a single readout channel and a DC voltage of 8V was applied at the input of the transimpedance amplifier to give a voltage across the capacitance used to sense motion of 13V. To allow the resonant frequency to be varied, 4V was applied to the remaining comb capacitance, giving an initial bias on this comb of 9V. Equation (3.16) was used to predict that under these bias conditions the resonant frequency of the sample (R_1) is expected to be 15.48kHz.

5.6 Tracking system testing

To test the PLL tracking system that has been built, the resonator was operated at a pressure of 100Pa. At this pressure the natural Q of the resonant system is 270. This Q-value was chosen because it represents a value of effective Q that can be achieved with relative ease using Q-control in air at atmospheric pressure. Operating at this vacuum level therefore provides an indication of the best-case performance of the tracking system. This can then be used to assess the relative performance of the tracking system when the resonator is operating under the action of Q-control at atmospheric pressure. Despite the relatively large velocity signal that is observed at this Q-value, the tunable filter remained in place in order to demonstrate that when the filter is tuned to the resonant frequency of the test sample, the tracking system stabilised at the the correct frequency.

Figure 5.7 shows the observed PLL frequency as a function of time. The critical results of this test are that the system stabilises at a frequency of 15478.780Hz and the root mean square variation in the detected resonant frequency is 67mHz (4 parts per million). This frequency

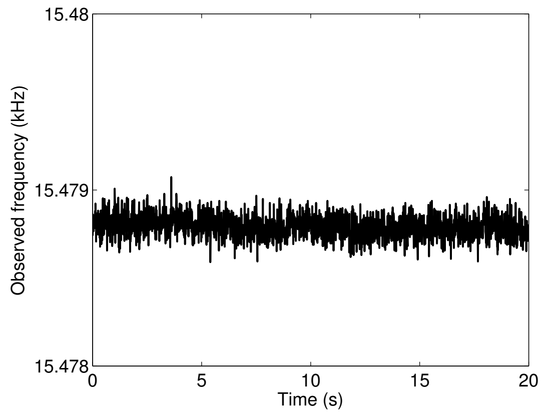

Figure 5.7: Phase-locked loop frequency as a function of time when the resonator is operated at a pressure of 100Pa.

variation is similar to the frequency variation observed in other modern PLL-based measurement systems [72]. The measured frequency variation is approaching the fundamental limit of 30mHz that is achievable with this DDS system at the chosen clock frequency. This measurement forms the benchmark for comparison with the system when the resonator is operated in air at atmospheric pressure.

5.7 Summary

In this chapter, the hardware required to build a system for automatically monitoring the resonant frequency of a MEMS resonator was described. The system is based upon a phase-locked loop architecture, however the key difference between a typical PLL and the PLL implemented in this system is the use of a programmable waveform generator as the VCO. This facilitates both high sensitivity and compatibility with a wide range of resonant frequencies. The key feature of the phase detector that has been used is that the phase error is reduced to zero when the system is locked. This means that when the resonant frequency of the resonator under test is within the range of frequencies that the DDS has been programmed to produce, the system can always locate its resonant frequency.

The system also includes a switched capacitor bandpass filter which can be used to eliminate the phase change introduced to the velocity signal by the readout electronics. The key feature of this filter is that it is possible to vary its centre frequency and resonators with a wide range of resonant frequencies can therefore be accommodated by altering the frequency of an external clock signal applied to the filter circuit. This removes the requirement to alter component values, as is necessary in a typical active filter circuit when there is variability in the resonant frequency of test devices.

To simulate a change in mass of the sensor, it will be possible to independently reduce the effective spring constant of the resonant system by applying a DC bias voltage to a free comb capacitor. Single-channel readout instead of differential readout is required to achieve this. To minimise the impact upon the performance of the system, the bias voltage applied to the moving structure was reduced from 0V to -5V to increase the effective driving and readout bias voltages. Using these bias conditions, the sensor was tested in a vacuum to assess the frequency stability of the system when the natural Q was 270. This corresponds to a sensible value for when the effective Q is increased at atmospheric pressure. Results show that the uncertainty in frequency is 67mHz rms. This value forms a benchmark for comparison with the performance of the system when the resonator operates at atmospheric pressure with and without Q-control.

Chapter 6

Tracking system characterisation

6.1 Introduction

In the previous chapter, the design of a system for monitoring the resonant frequency of a MEMS resonator was described. A programmable waveform generator has been used as the VCO in the phase-locked loop that forms the tracking system. This means that the system that has been developed is compatible with resonators that have a wide range of resonant frequencies. Another key functional block in the system is a switched capacitor bandpass filter which is used to process the velocity signal produced by the readout electronics. The frequency response of this filter can be tuned which means that it is possible to ensure that the phase shift incurred by the velocity signal is always zero degrees. The performance of the prototype measurement system was characterised, when a resonator was operating in a moderate vacuum level, by recording the noise in the observed driving frequency.

In this chapter, the experiments performed to characterise the performance of the system when the resonator operates at atmospheric pressure are described. In addition, results of tests conducted to investigate the possible benefit of implementing Q-enhancement are also presented. For the tests, both with and without Q-control, a variable DC bias voltage was used to change the resonant frequency of the system. This voltage was applied to the free readout comb capacitance available when a single readout channel is used. Finally, the accuracy of the observed change in driving frequency in response to a known change in resonant frequency has been studied and the results of this investigation are also presented in this chapter.

6.2 Resonant frequency monitoring

6.2.1 Native Q

In the previous chapter, the construction of a PLL-based system for monitoring the resonant frequency of MEMS resonators was described. The system was used to monitor the resonant frequency of a test structure operating in a vacuum when the natural Q was 270. The noise in the observed frequency was 67mHz rms. This section contains results showing the performance of the system when the resonator is operated at the natural Q at atmospheric pressure.

When the resonator was operated in a vacuum, resonance was observed at 15.48kHz. However when the resonator is operated in air, the magnitude of the AC driving component is significantly greater ($10V_{pp}$). A consequence of this is that resonance is expected to occur at 15.45kHz. Figure 6.1 shows the observed frequency of the system as a function of time when the resonator was operated at atmospheric pressure. The figure shows that the PLL tracking

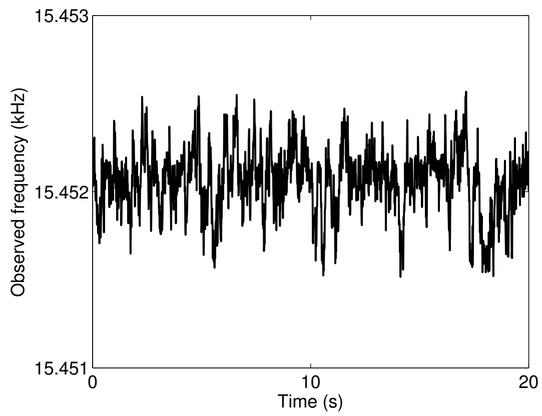

Figure 6.1: Phase-locked loop frequency as a function of time when the resonator is operated at a pressure of 100kPa.

system stabilises at a frequency of 15452.016Hz and that variation in frequency is 200mHz rms. This compares to 67mHz rms when the resonator was in a moderate vacuum and the Q was approximately 50 times larger. The observed difference in frequency noise is because the low Q at atmospheric pressure has caused an increase in phase noise [45]. In turn, this leads to noise in the frequency control voltage at the output of the loop filter and hence an increase in frequency noise.

To further assess this result, recall that in section 1.6.4 a study by Tamayo into the noise present in a resonant system was described. In the study, Tamayo showed that when a resonant system operates at its natural damping level, any phase noise present is proportional to $1/Q^{1/2}$ or $1/Q$. This depends upon if the dominant noise source is either thermal vibrations of the resonator or noise in the motion sensor, respectively. Tamayo also showed that after taking any variation in the driving force between measurements into account, that phase noise is proportional to either $1/(F_0Q^{1/2})$ or $1/(F_0Q)$, where F_0 is the magnitude of the primary driving force.

When the resonator was operated at atmospheric pressure as shown in Figure 6.1, the primary driving force was a factor of 25 greater than when the system was characterised with the resonator operating in a moderate vacuum (Figure 5.7). This factor of 25 difference in driving force between the measurements at each pressure level has been taken into account. As a result, when the pressure increases from 100Pa to atmospheric pressure, phase noise is expected to decrease by a factor of three if the noise is dominated by thermal vibrations. Alternatively, if the primary source of noise is the motion sensor and readout electronics, phase noise is expected to rise by a factor of 2.5. In this system measurements have shown that noise has increased by a factor of three. This suggests the system behaves in a similar fashion to when the dominant noise source is the detection electronics and not thermal vibrations of the moving structure.

6.2.2 Enhanced Q

Experiments were performed to investigate if increasing the effective Q by velocity feedback reduces the variation in frequency to the level observed when the resonator operates at 100Pa. The tracking system was tested using Q-control at two feedback levels. The effective quality factor ($\hat{Q}$) was approximately 40 and then 200, corresponding to an increase by a factor of 10 and 40 respectively. Figure 6.2 shows the observed tracking frequency as a function of time for each value of $\hat{Q}$.

When the effective Q was increased using velocity feedback by a factor of 10, the uncertainty in the observed frequency was 390mHz rms. The frequency variation increased to approximately 1.1Hz rms when the effective Q was increased by a factor of 40. The critical result of these tests is that increasing the effective Q using velocity feedback does not reduce the apparent frequency noise to the levels observed in a vacuum. In fact, the effect of increasing the effective Q was to degrade the performance of the system.

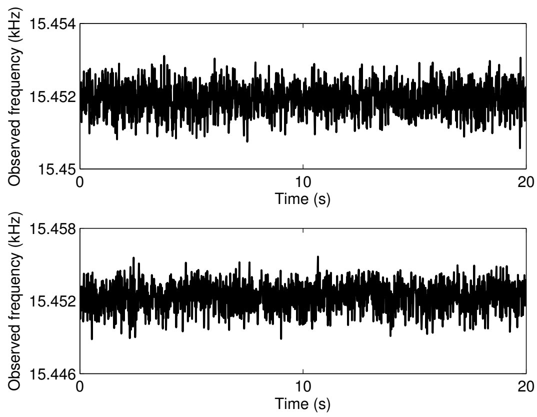

Figure 6.2: Phase-locked loop frequency as a function of time when the resonator is operated at a pressure of 100kPa under the action of Q-control, when $\frac{\hat{Q}}{Q} = 10$ (above) and $\frac{\hat{Q}}{Q} = 40$ (below).

6.2.3 Effect of noise on measurement system

The noise in the readout voltage, which is proportional to the velocity of the resonator, was measured with and without velocity feedback. As predicted by Tamayo [45], the increase in the effective Q of the system by a factor of 40 (obtained using velocity feedback), is accompanied by an increase in the rms noise observed in the velocity signal by a factor of approximately 40. Although the measured resonant frequency is obtained from this velocity-dependent readout voltage, the relevant noise is the resulting variation in the observed resonant frequency. The results in Figures 6.1 and 6.2 have shown that when Q-enhancement is implemented, the noise in the measured resonant frequency determined by the measurement system only increases by a factor of approximately five, despite the 40-fold increase in the noise in the readout voltage. This is because the frequency noise is measured at the output of the low pass filter after the digital phase detector and the digital system acts to reject some of the noise in the analogue velocity-dependent readout voltage at its input.

6.3 Resonant frequency tracking

Experiments have been conducted to demonstrate the response of the tracking system to a small change in resonant frequency. To simulate a small increase in mass of the resonator, the resonant frequency control voltage (V_e) was stepped up from its initial value of 4V by a small amount. This was achieved by programming an external Power Supply Unit (PSU) used to generate the control voltage. The resulting change in resonant frequency was then recorded and data has been post-filtered in MATLAB by a 100-tap moving average filter, giving a time constant of approximately one second.

Experiments have shown that the resulting change in frequency is a similar magnitude to the observed frequency noise when a small step in voltage of 100mV is applied. Figure 6.3 shows the response of the tracking system to this step change in bias voltage after five seconds. The system has tried to follow the change in resonant frequency, however the added noise with

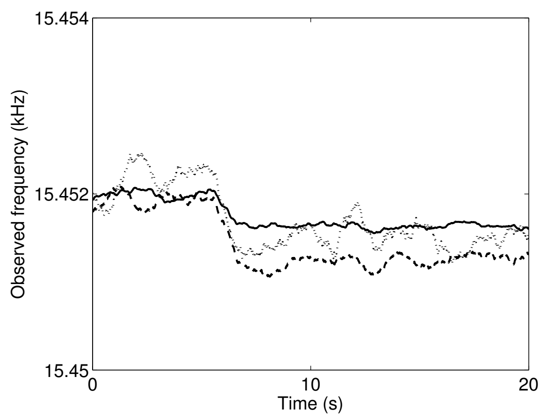

Figure 6.3: Phase-locked loop response to a small change in resonant frequency, when the resonator is operated at the natural Q (solid) and under the action of Q-control, $\frac{\hat{Q}}{Q} = 10$ (dashed) and $\frac{\hat{Q}}{Q} = 40$ (dotted).

Q-enhancement makes this change more difficult to detect. Even when Q-enhancement is not employed a significant problem with the frequency tracking system is that the observed change in resonant frequency of 0.5Hz is not the same as the expected change of 2Hz caused by the 100mV increase in resonant frequency control voltage. This suggests that the tracking system does not accurately follow changes in resonant frequency.

6.4 System accuracy

Results in the previous section show that when the resonant frequency of the resonator changes, the system can detect the change. This means that it could be used to detect the presence of a target substance if the resonators were functionalised. However, the observed change in driving frequency produced by the PLL tracking system is lower than expected which means that the change won't be accurately quantified. This error occurs both with and without Q-control. The PLL tracking system will always stabilise at a frequency where the total phase change in the phase-locked loop is zero degrees and in this section the PLL is modelled in order to explain the observed behaviour of the tracking system.

Consider when the resonator operates without Q-control with the tunable filter set to the initial resonant frequency of the MEMS resonator (ω_{01}). The phase of the signal at the input to the phase detector is determined by the combined phase of the resonator's velocity and also the phase change caused by the readout and filter electronics. Using Equations (1.9) and (5.3), this is given by

$$\theta(\omega) = \frac{\pi}{2} - \arctan\left(\frac{\frac{\omega}{\omega_{01}}}{Q\left(1 - \frac{\omega^2}{\omega_{01}^2}\right)}\right) + \psi_t(\omega). \tag{6.1}$$

Because the filter has been tuned for the particular resonator and bias conditions, the phase change caused by the electronics at the resonant frequency is $\psi_t(\omega_{01}) = 0$. The frequency at which the PLL tracking system stabilises ($\theta = 0$) is therefore $\omega = \omega_{01}$, as expected. However, when the resonant frequency of the system changes (i.e. $\omega_{01} \rightarrow \omega_{02}$), the tracking system stabilises at the solution of

$$\frac{\pi}{2} - \arctan\left(\frac{\frac{\omega}{\omega_{02}}}{Q\left(1 - \frac{\omega^2}{\omega_{02}^2}\right)}\right) + \psi_t(\omega) = 0, \tag{6.2}$$

which is not at ω_{02} because $\psi_t(\omega_{02}) \neq 0$. Equation (6.2) shows that, assuming the Q-value remains constant, the frequency at which the system will settle is a function of both ψ_t and the new characteristic frequency of the sensor (ω_{02}).

To model the Q-enhanced system, consider once again the phase of the observed signal at the input to the phase detector. Using Equations (4.14) and (5.3) gives the following expression when Q-control is applied

$$\theta(\omega) = \frac{\pi}{2} - \arctan\left(\frac{\frac{\omega}{\omega_{02}}\left(1 - \frac{Q}{\omega_{02}}\Re_t(\xi)\right)}{Q\left(1 - \frac{\omega^2}{\omega_{02}^2} + \frac{\omega}{\omega_{02}^2}\Im_t(\xi)\right)}\right) + \psi_t(\omega). \tag{6.3}$$

To take into account the implementation of a single readout channel instead of differential readout, ξ has been modified to ξ_t

$$\Re(\xi_t) = \frac{2V_{DC}V_sG_{INA}RL}{m}\left(\frac{dC}{dx}\right)^2 \cos\left(\psi_t(\omega)\right) = \bar{\xi}_t \cos\left(\psi_t(\omega)\right), \tag{6.4}$$

$$\Im(\xi_t) = \frac{2V_{DC}V_sG_{INA}RL}{m}\left(\frac{dC}{dx}\right)^2 \sin\left(\psi_t(\omega)\right) = \bar{\xi}_t \sin\left(\psi_t(\omega)\right). \tag{6.5}$$

This means that the frequency at which the PLL tracking system stabilises at is given by the solution of

$$\frac{\pi}{2} - \arctan\left(\frac{\frac{\omega}{\omega_{02}}\left(1 - \frac{Q}{\omega_{02}}\bar{\xi}_t\cos\left(\psi_t(\omega)\right)\right)}{Q\left(1 - \frac{\omega^2}{\omega_{02}^2} + \frac{\omega}{\omega_{02}^2}\bar{\xi}_t\sin\left(\psi_t(\omega)\right)\right)}\right) + \psi_t(\omega) = 0. \tag{6.6}$$

The solution of Equation (6.6) is valid for any PLL-based system designed to locate the resonant frequency of a mass-spring-damper system by monitoring the velocity of the mass and when the effective Q is increased by a feedback system that introduces a frequency-dependent phase shift to the measured velocity signal.

Equations (6.2) and (6.6) can be solved to predict the frequency at which the tracking system will stabilise with and without Q-enhancement respectively. When these equations are solved numerically, both solutions are always identical which explains why the change in frequency generated by the phase-locked loop in response to a change in resonant frequency appears to be independent of the effective Q. To prove that Equation (6.6) has the same solution as Equation (6.2), Equation (6.6) was rearranged to give

$$\tan\left(\frac{\pi}{2} + \psi_t(\omega)\right) = \frac{\frac{\omega}{\omega_{02}}\left(1 - \frac{Q}{\omega_{02}}\bar{\xi}_t\cos\left(\psi_t(\omega)\right)\right)}{Q\left(1 - \frac{\omega^2}{\omega_{02}^2} + \frac{\omega}{\omega_{02}^2}\bar{\xi}_t\sin\left(\psi_t(\omega)\right)\right)}, \tag{6.7}$$

hence

$$-\cot\left(\psi_t(\omega)\right)=\frac{\frac{\omega}{\omega_{02}}\left(1-\frac{Q}{\omega_{02}}\bar{\xi}_t\cos\left(\psi_t(\omega)\right)\right)}{Q\left(1-\frac{\omega^2}{\omega_{02}^2}+\frac{\omega}{\omega_{02}^2}\bar{\xi}_t\sin\left(\psi_t(\omega)\right)\right)}. \tag{6.8}$$

Substituting $\frac{\cos(\psi_t(\omega))}{\sin(\psi_t(\omega))}$ for $\cot\left(\psi_t(\omega)\right)$ and cross-multiplying gives

$$\frac{\cos\left(\psi_t(\omega)\right)}{\sin\left(\psi_t(\omega)\right)}\left(1-\frac{\omega^2}{\omega_{02}^2}+\frac{\omega}{\omega_{02}^2}\bar{\xi}_t\sin\left(\psi_t(\omega)\right)\right)=\left(\frac{\omega}{\omega_{02}^2}\bar{\xi}_t\cos\left(\psi_t(\omega)\right)-\frac{\omega}{Q\omega_{02}}\right). \tag{6.9}$$

Multiplying both sides of Equation (6.9) by $\sin\left(\psi_t(\omega)\right)$ gives

$$\cos\left(\psi_t(\omega)\right)\left(1-\frac{\omega^2}{\omega_{02}^2}\right)=-\sin\left(\psi_t(\omega)\right)\frac{\omega}{Q\omega_{02}}, \tag{6.10}$$

which is equal to

$$-\cot\left(\psi_t(\omega)\right)=\frac{\frac{\omega}{\omega_{02}}}{Q\left(1-\frac{\omega^2}{\omega_{02}^2}\right)}. \tag{6.11}$$

Equation (6.11) can then be rearranged to give Equation (6.2)

$$\frac{\pi}{2}-\arctan\left(\frac{\frac{\omega}{\omega_{02}}}{Q\left(1-\frac{\omega^2}{\omega_{02}^2}\right)}\right)+\psi_t(\omega)=0.$$

This explains why the PLL output frequency measured when the resonator was tested both with and without Q-control appeared to change by the same amount. The key conclusion of this analysis is that Equation (6.2) could be used to predict the change in output frequency from the tracking system in response to a known change in resonant frequency.

6.5 Model validation

A step change in voltage (V_e) of 1V was applied to the system. Figure 6.4 shows that the observed change in driving frequency was close to 8Hz. However from Equation (3.16), the predicted change in resonant frequency due to this change in V_e is approximately 20Hz. Also shown in the figure is the solution of Equation (6.2) which shows that the model of the tracking system that has been developed predicts a 7Hz change in driving frequency in response to the

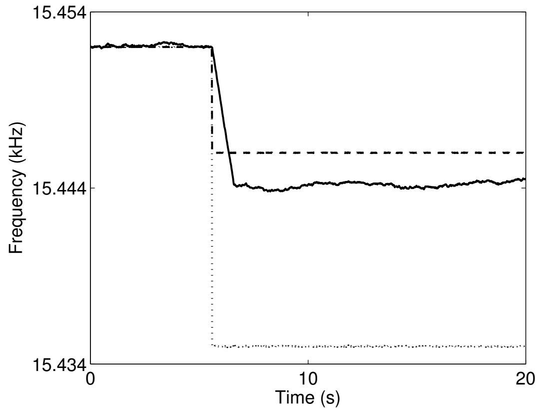

Figure 6.4: Observed phase-locked loop tracking behaviour (solid), simulated (dashed) and also the expected behaviour (dotted).

1V change in the frequency tuning voltage. This is in reasonable agreement with the 8Hz change in frequency that was measured when the system was tested. The small discrepancy between the observed change in frequency and that predicted by Equation (6.2) is due to the dependence of the system upon the exact values of the extracted coefficients in the polynomial defining ψ_t (Equation (5.3)).

Despite using the tunable filter to eliminate phase change in the readout electronics at the initial resonant frequency of the system, this phase change still causes undesirable behaviour. This is because in response to a change in resonant frequency, the driving frequency of the system moves from the initial resonant frequency, where $\psi_t = 0$. The resulting effect of this is that the PLL does not stabilise at the new resonant frequency. Instead the system stabilises at the frequency where the total phase change in the electronics and the phase response of the resonator at the natural Q sum to zero. The significance of this result is that when the phase change with respect to frequency in the readout electronics is larger or comparable to the resonator's native phase response, a phase-locked loop tracking system will not always closely follow the resonant frequency of the system.

6.6 Summary

The performance of the hardware designed for monitoring the resonant frequency of MEMS resonators has been characterised. Results of these experiments have been described in this chapter. Initially, a prototype resonator was operated at atmospheric pressure without the use of Q-control. Measurements showed that the observed frequency noise was a factor of three greater than when the resonator operated at a pressure of 100Pa. After accounting for the increase in driving force required at atmospheric pressure, this result suggests that noise present in the system is dominated by noise in the readout electronics and not thermal vibrations of the MEMS structure.

The tracking system was subsequently operated in air at atmospheric pressure under the action of Q-control. When the effective Q was a factor of 40 greater than the native value, as expected the increase in noise in the velocity signal also increased by a factor of 40. The corresponding frequency variation at the output of the digital phase detector was observed to increase by a factor of five. When a PLL is used to monitor a resonant system, the magnitude of this variation determines minimum change in resonant frequency that can be detected and hence the resolution of the sensor. This means that the key conclusion of these experiments is that increasing the effective Q by force feedback does not improve the ability of this system to locate the resonant frequency of the structure.

When the tracking system responds to a change in resonant frequency by altering its output frequency, the observed adjustment in the driving frequency produced by the PLL is different to the predicted change. This discrepancy occurs both when the system is operating with and without Q-control. A model has been developed that explains this undesirable behaviour. The model that has been developed shows that the frequency at which the system stabilises depends critically on the phase response of the resonator at its natural Q and also the phase response of the readout electronics. This means that the tracking system will not stabilise at the most recent resonant frequency of the system. The reason for this is because the rate of change of phase with respect to frequency in the readout electronics is not insignificant in comparison with the phase response of this resonant system at its native Q.

Chapter 7

Fixed frequency systems

7.1 Introduction

In the previous chapter, the performance of the hardware for monitoring the resonant frequency of MEMS resonators was investigated. The key result of these experiments is that when the effective Q of the resonant system is increased by velocity feedback, the performance of the PLL tracking system is degraded. This is because the effect of Q-enhancement is to increase noise, without increasing the signal that is measured. Further experiments also showed that the observed change in driving frequency in response to a known change in resonant frequency is incorrect. This problem occurs both with and without Q-control and is independent of the particular feedback level. Analysis has shown that this error in the tracking frequency can be explained by taking into account the phase change in the feedback loop introduced when the driving frequency attempts to follow a change in resonant frequency.

In this chapter, a system for measurement of the phase of a MEMS resonant system is described. The key benefit of this approach is that since the rate of change of phase with respect to frequency increases with quality factor, Q-enhancement increases the signal that is measured. Furthermore, by working at a fixed frequency it is possible to avoid phase shifts in the readout electronics. An alternative technique that is also immune to the effects of phase change in the readout electronics is also described in this chapter. This technique is based upon automatically tuning the resonant frequency of a resonator to its original resonant frequency in response to a change in characteristic frequency of the resonant system.

7.2 Fixed frequency tracking

When the tracking system described in chapter 5 is used to monitor the resonant frequency of a MEMS structure, the observed change in driving frequency in response to a shift in resonant frequency is a function of the phase response of the readout electronics. This problem occurs despite using the tunable filter to eliminate phase change in the readout electronics at the initial resonant frequency of the system. As a result, the ability to easily quantify a change in resonant frequency is lost. To avoid the complications arising from operating at a driving frequency where the phase change caused by the readout electronics is non-zero, the simplest solution is to always operate at the initial resonant frequency of a resonator. Consequently, the possibility of performing tests at a fixed frequency has been investigated.

When the bandpass filter used to process the velocity signal is tuned to the resonant frequency of a test structure, the PLL tracking system that has been built can be used to easily locate this frequency. However, instead of automatically altering the driving frequency in response to a change in resonant frequency, the key feature of the techniques described in this chapter is that the frequency control word produced by the FPGA controller will be kept constant. The effect of this will be to maintain a fixed driving frequency at the resonant frequency of the MEMS device, where the phase change in the readout electronics is zero. Any ensuing change in resonant frequency causes the phase of the velocity signal to alter and the observed change will be solely due to the mismatch between the driving frequency and the new resonant frequency of the MEMS system. Any observed change in phase can then be used to quantify the change in resonant frequency. An alternative approach, however, is to create a closed-loop system in which the resonant frequency will be automatically returned to the original resonant frequency of the system. By measuring the amount of tuning required to do this, it will be possible to quantify the change in resonant frequency that occurred. In this chapter the performance of these two approaches is compared.

7.3 Phase measurement electronic hardware

To build a system designed to operate at a fixed frequency, used either to measure a change in the resonator's phase or in a closed-loop system to automatically return the resonant frequency of the system to its original frequency, a method of measuring the absolute phase of the resonator's velocity is required. An EXOR gate followed by a low pass filter is a convenient method of obtaining a voltage which is directly proportional to the phase difference between two signals. However, the range of the output voltage from an EXOR gate phase detector corresponds to a phase difference of between 0° and 180°. This means that it is necessary to shift the velocity signal by 90° to ensure that the output voltage is in the middle of the measurement range when the system operates at its resonant frequency.

The obvious solution to change the phase of the velocity signal by 90° is either by integration or differentiation of the signal using standard op-amp circuits. The key benefit of this approach is that the phase change in each of these circuits is $\pm 90°$ over the whole frequency range, which is not possible with a simple first-order filter circuit, for example. However, practical considerations reduce the appeal of using these approaches. For example, when the DC component at the input of an integrator is non-zero, the output voltage ramps and saturates at the op-amp power supply voltage. On the other hand, the key practical problem with a differentiator circuit is the large high frequency gain, which renders the circuit particularly susceptible to noise. In fact, experience shows that using a differentiator to shift the phase of the velocity signal in this system leads to the presence of a spurious signal. The frequency of this signal is at the switching frequency of the tunable switched capacitor bandpass filter.

To avoid the problems described above, it is possible to change the phase of the digital velocity signal that was previously generated from the analogue velocity signal (in section 5.4). This is feasible because the input to the EXOR gate phase detector is a digital signal. Figure 7.1 shows a circuit that can be used for generating digital signals in quadrature [73–75]. The circuit comprises two d-type flip flops packaged in a 4013B Complementary Metal-Oxide-Semiconductor (CMOS) IC. Quadrature outputs are produced at a frequency that is one fourth that of the clock. Due to this frequency division, it is necessary to multiply the input frequency by a factor of four. The simplest way to achieve this is by placing the Digital

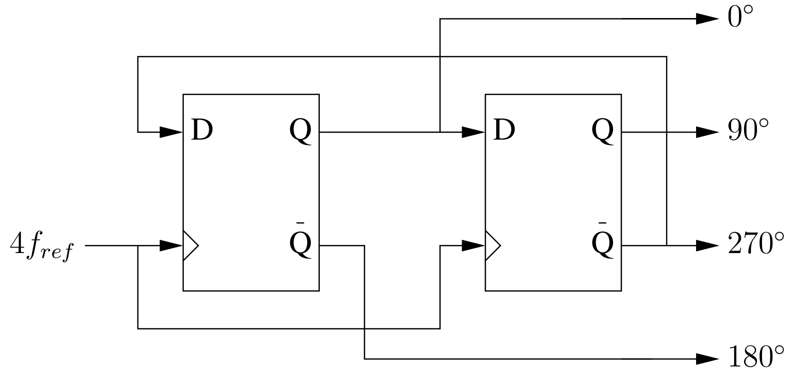

Figure 7.1: Digital quadrature generator using d-type flip flops.

Quadrature Generator (DQG) as a divide-by-four block in the feedback loop of a conventional PLL created using a standard 4046B integrated circuit. Figure 7.2 shows this arrangement. The specifications for the phase detector, loop filter and VCO shown in Figure 7.2 are as

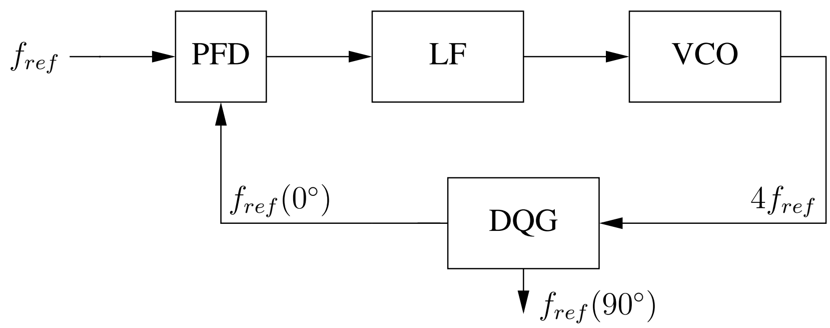

Figure 7.2: Phase locked loop for d-type flip flop circuit input frequency generation.

follows. To ensure that the output of the phase shifting circuit is exactly 90° out of phase with the incoming signal over a wide frequency range, the choice of phase detector is the phase-frequency detector. This is because the PFD reduces the phase error to zero for all input frequencies. A loop filter with a characteristic frequency of 100Hz is used to filter the output of the PFD, this is a compromise between the bandwidth and noise rejection. The internal VCO in the 4046B chip has been programmed to generate frequencies in the range of approximately 40kHz→80kHz, hence the working frequency range of the phase shifter is 10kHz→20kHz.

The output signal from the digital 90° phase shifting circuit is then connected to one input of the EXOR gate phase detector. The other input is the square-wave output from the AD9833 waveform generator. To measure the phase difference between the velocity and the primary driving force, the average value of the square-wave output from the EXOR gate phase detector must be calculated. To do this, the output of the EXOR gate is low-pass filtered using an RC network with a characteristic frequency of 100Hz. In this way, the DC level at the output of the filter covers the range -90° $\leq \phi \leq$+90°.

The phase signal that is produced using the hardware described in this section must be sampled and processed in the FPGA controller. The AD7367 ADC used in the PLL tracking system is a 2-channel device and only one of these channels has been used. Consequently it is possible to sample the voltage representing the phase of the resonator, without the addition of any further hardware. To maximise the resolution, first the voltage is amplified by a factor of eight such that the full scale input to the ADC corresponds to -22.5° $\leq \phi \leq$+22.5°. As the ADC has 14-bit resolution, this corresponds to a theoretical minimum detectable change in phase of 3m°.

7.4 Phase response

7.4.1 Phase noise characterisation

The previous section contains a description of the hardware that has been built to automatically measure the phase difference between the resonator's velocity and the primary driving force. The resulting digital word representing the phase can be used to monitor the system and the performance of this technique will be determined by the amount of noise present in the measured phase signal. Consequently noise present in the measured phase has been characterised and results of this are given in this section.

The switched capacitor filter was tuned to ensure that there was no change in phase at the resonant frequency of a test resonator. Following this initial tuning process, the PLL tracking system described in chapter 5 was used to locate the resonant frequency of the MEMS structure. After stabilisation of the PLL, the driving frequency was subsequently fixed by halting the frequency-update algorithm in the FPGA. In the absence of a stimulus, any observed phase signal produced by the phase measurement system that has been built will be attributed to noise. This means that phase noise can be measured at the both the natural Q and at a high effective Q.

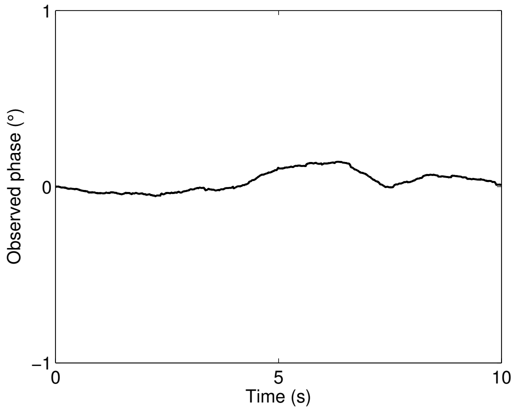

Figure 7.3: Measured phase of the resonant system with respect to the primary driving force without Q-control, as a function of time.

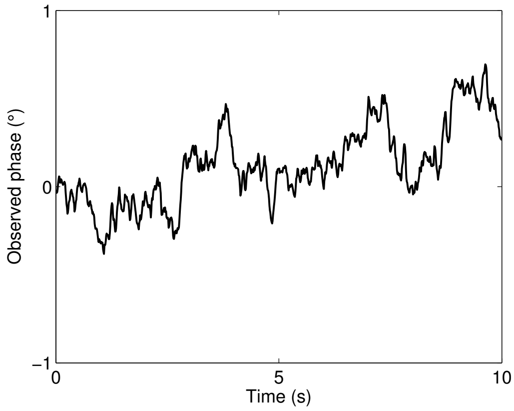

Figure 7.4: Measured phase of the resonant system with respect to the primary driving force with Q-control ($\frac{\hat{Q}}{Q}$ =40), as a function of time.

Figures 7.3 and 7.4 show the measured phase of the MEMS structure with respect to the primary driving frequency as a function of time. The resonator was exposed to air at atmospheric pressure and in Figure 7.3 and the system operated at its native Q. Conversely in Figure 7.4 the effective Q was increased by a factor of 40. Data was post-filtered in MATLAB by a 100-tap moving average filter, giving a time constant of approximately one second. When the resonator was operating at its natural Q, the magnitude of the measured phase noise was approximately 0.2°. This increased to 1° when the effective Q of the resonant system was increased by a factor of 40. This increase in phase noise is similar to the results in section 6.2.2 showing that the frequency noise rises by a factor of five when the tracking system is used to monitor the resonant frequency of the Q-enhanced system.

7.4.2 Detection resolution

When the driving frequency is fixed at the resonant frequency of the system corresponding to the current bias voltages (ω_{0_1}), from Equation (1.9) the rate of change of phase with respect to resonant frequency is given by

$$\frac{d\phi}{d\omega_0} \approx \frac{2Q\omega_{0_1}}{\omega_0^2}. \tag{7.1}$$

Integrating to find the change in phase after a small change in resonant frequency, $\Delta\omega_0$, gives

$$\phi \approx \frac{2Q}{1+\frac{\omega_{0_1}}{\Delta\omega_0}}. \tag{7.2}$$

Equation (7.2) shows that, as expected, for a particular change in resonant frequency the expected change in phase is greater for larger values of Q. This can be rearranged to calculate the new resonant frequency, $\omega_{0_2} = \omega_{0_1} + \Delta\omega_0$

$$\omega_{0_2} \approx \frac{\omega_{0_1}}{1-\frac{\phi}{2Q}}. \tag{7.3}$$

As $\frac{\phi}{2Q}$ <<1, this can be approximated as

$$\omega_{0_2} \approx \omega_{0_1}\left(1+\frac{\phi}{2Q}\right). \tag{7.4}$$

The uncertainty in frequency is therefore directly proportional to the level of noise in the phase measurement. Taking phase noise into account and using Equation (7.4), the uncertainty in the measured frequency ($N_{\omega_{0_2}}$) is directly proportional to the noise in the measured phase signal (ϕ_n),

$$N_{\omega_{0_2}} \approx \omega_{0_1}\frac{\phi_n}{2Q}. \tag{7.5}$$

The significance of Equation (7.5) is that if velocity feedback increases the effective Q by more than the increase in noise, this will lead to a reduction in frequency noise. Results in the previous section show that the noise in the measured phase signal produced by the phase measurement system does not rise by the same factor as does the effective Q when velocity feedback is implemented. It is therefore possible to take advantage of this to reduce the uncertainty in the detected change in resonant frequency. The result of this is that when Q-control is implemented, the noise in the calculated resonant frequency will reduce by a factor of

$$\frac{N_{\omega_{0_2}}}{\hat{N}_{\omega_{0_2}}} = \frac{\hat{Q}\phi_n}{Q\hat{\phi}_n}. \tag{7.6}$$

Results presented in sections 6.2.2 and 7.4.1 show that $\frac{\phi_n}{\hat{\phi}_n}$ =0.2 when the effective Q is equal to 40 times its native value (and the primary driving force is reduced to maintain a constant velocity signal). Therefore the conclusion of this analysis is that when velocity feedback is used to increase the effective Q by a factor of 40 ($\frac{\hat{Q}}{Q} = 40$), the detection capability will improve by approximately 20dB.

7.4.3 Response to stimulus

The electronics described in section 7.3 were used to monitor the phase of the resonant system. To test the system, the resonant frequency control voltage (V_e) was increased by 500mV both at the natural Q-value and also when the effective Q was increased by a factor of 40. Equation (3.16) shows that this causes an expected change in resonant frequency of approximately 10Hz. From Equation (7.2), this corresponds to an expected change in phase of 0.32° at the natural Q and 13° when the effective Q is increased by a factor of 40. Figure 7.5 shows that the phase changes by approximately 0.4° at the natural Q and by 15° when Q-control is used. In the figure, the phase changes under the two different conditions are on different axes

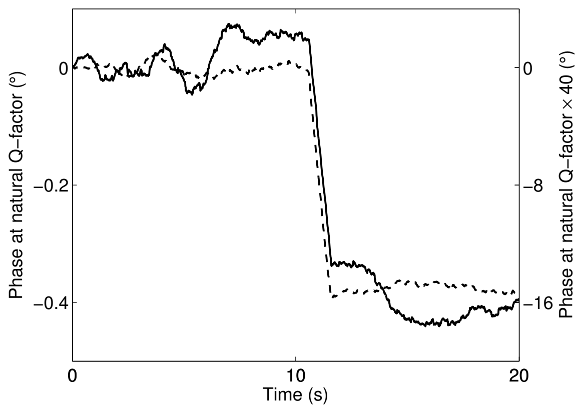

Figure 7.5: Phase change due to a 10Hz change in resonant frequency, without Q-control (solid) and with Q-control (dashed, $\frac{\hat{Q}}{Q}$ =40).

to show that the responses are very similar but that, as expected, Q-enhancement has led to a larger change in phase. Figure 7.5 also shows that when Q-control is used, identification of the change in phase of the resonator is relatively straightforward due to the large SNR. When the system operates at the natural Q, it is more difficult to determine the exact change in phase.

To demonstrate the benefit of using Q-enhancement in combination with a measurement of the phase of the resonator, the resonant frequency of the sensor was subsequently changed by 2.5Hz. For this smaller change in resonant frequency, the expected change in phase is 3.5° when Q-enhancement is used and approximately 0.1° at the natural Q. Figure 7.6 shows the measured phase, at the natural Q and when Q-enhancement is used. Results such as these show that at the natural Q it has become difficult to reliably distinguish between the induced change in phase and random variations caused by noise. Consequently it is very difficult to determine the exact change in phase. In contrast when Q-enhancement is employed, it is still easy to distinguish between the response of the system to the induced change in resonant frequency and any random variations.

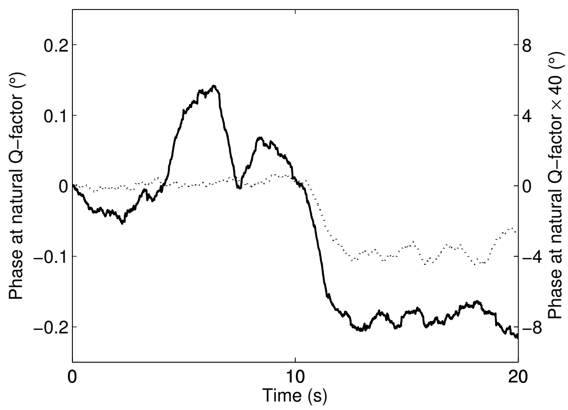

Figure 7.6: Phase change due to a 2.5Hz change in resonant frequency, without Q-control (solid) and with Q-control (dotted, $\frac{\hat{Q}}{Q}$ =40).

It is theoretically possible to improve the sensitivity of the system further by increasing the effective Q of the resonator even more. However, if the effects of damping are reduced further then the result can be a large amplitude response and damage to the resonator. At these relatively low levels of Q-enhancement the possible dangers of damaging the resonator are avoided by reducing the amplitude of the driving signal. However, the effectiveness of this strategy is limited by noise in the drive signal which limits the minimum amplitude that can be used and hence the maximum level of Q-enhancement. Despite the limit to the amount of Q-enhancement that can be employed safely, the results in Figure 7.5 and Figure 7.6 show that an improvement in the signal to noise ratio of approximately 20dB is achieved when velocity feedback is used to increase the effective Q of the MEMS resonator by a factor of 40.

7.4.4 Detection range

Since the detection range of the system that has been built is limited, a potential disadvantage of measuring the phase of the system occurs when a large change in phase is expected. This will be a problem if the sensor is to be used to detect cumulative small changes in mass, for example. To illustrate this, recall Equation (7.2) which describes the relationship between phase, Q and resonant frequency

$$\phi \approx \frac{2Q}{1 + \frac{\omega_{0_1}}{\Delta\omega_0}}.$$

Equation (7.2) has been solved to find the change in resonant frequency required to saturate the measured phase signal at -22.5°. For this system, when the effective Q is artificially increased by a factor of 40 to approximately 200, the maximum measurable change in resonant frequency is 15Hz. However, Equation (7.2) does not take into account the limited linear region of phase change with respect to resonant frequency. Therefore another disadvantage of this system is that the predicted maximum measurable change in resonant frequency is an overestimate. This effectively further limits the magnitude of any change in resonant frequency that can be accurately measured.

7.5 Voltage controlled resonant frequency

7.5.1 Concept

In this section, an alternative approach to making measurements of the phase of the resonator is described. A benefit of this system over phase measurement is that the system can accurately measure both small and large changes in resonant frequency. The method is based upon the hardware used to measure the phase of the resonator, the design of which is discussed in section 7.3. However to implement this technique, in response to an observed change in phase of the system, the resonant frequency will be returned to its initial value by varying a DC bias voltage (V_e). Therefore a key requirement for this technique is a Digital-to-Analogue Converter (DAC) which can be programmed by the FPGA controller to control the resonant frequency of the resonator.

A convenient method for tuning the resonant frequency of a test sample is by varying the DC bias voltage (V_e) which is applied to the free comb capacitance available when single-ended readout is used. However, for characterising the prototype system, this comb capacitor is already used to stimulate the system. This means that in the prototype system a summing amplifier is required to create the DC bias voltage from two parts. The first part is a stimulus voltage and the second part is a feedback voltage. The latter is generated from a digital output from the FPGA controller using a DAC. In response to a change in the stimulus voltage, the feedback voltage will be automatically varied by the FPGA controller. The effect of this will be to return the resonant frequency of the system to its original value. Tests can be performed to check that the change in the feedback voltage cancels the induced change in the stimulus voltage.

The key component in the system that has been proposed is a DAC. Figure 7.7 shows a schematic diagram of the DAC used in this system, which is a simple DAC (AD7530) formed from an R-2R ladder. No timing signals are required and the settling time is 1μs which means that by addressing the parallel data word input using the FPGA controller, the output of the DAC can be updated at up to 1MHz. The output of the circuit can be programmed in the range 0V$\rightarrow$-4V, hence after inversion the DAC output voltage can be used as the feedback voltage component applied to the free comb capacitance.

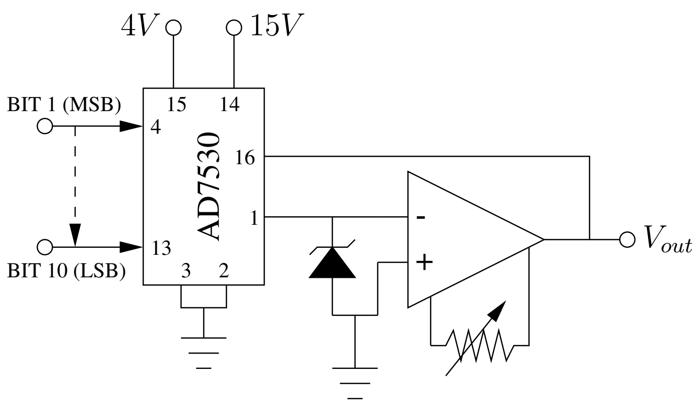

Figure 7.7: DAC for generating the resonant frequency control voltage.

7.5.2 Frequency tuning algorithm

To control the resonant frequency of the MEMS structure in response to an externally applied change in system parameters, the algorithm in the FPGA controller operates as follows. The algorithm averages the digital word representing the phase of the velocity signal, over numerous samples. This provides a digital reference word representing the initial resonant frequency of the system ($\phi = 0$, nominally the mid-rail of the ADC, 5V). The algorithm subsequently enters a tracking mode, during which the phase of the resonator is periodically tested and compared to the reference word.

If the measured phase leads or lags the reference phase, the control word to the DAC is updated in order to alter V_e in such a way that the resonant frequency returns to the initial value. For example, a step change in the stimulus voltage of 1V from the external PSU changes V_e from 4V to 5V and causes a change in the resonant frequency of the system. In response to the corresponding change in phase, the FPGA program reduces the tunable component of V_e until the measured phase is restored to the reference value. This occurs when the tunable component in V_e is equal to 3V, which means that V_e has been restored to the initial value of 4V. To quantify the change in resonant frequency, the change in control word to the DAC is monitored. This is then mapped to a voltage and hence a frequency using Equation (3.16).

7.5.3 Detection capability

The resolution of this system is determined by the stability of the frequency tuning voltage which is used to calculate the change in resonant frequency of the system. Since this is governed by noise present in the measured phase signal to which the system responds, Q-control will degrade the performance of the system without increasing the signal that is measured. This is because this technique responds to the sign and not the magnitude of the measured phase. Therefore no benefit is expected from the implementation of Q-control. To test the automatic tuning technique, the resonant frequency of the structure was located using the PLL tracking system. After stabilisation, tracking was halted and the frequency tuning algorithm was implemented. The performance of the system that has been built was then tested both with and without Q-control.

Figure 7.8 shows that in response to an applied stimulus acting to increase V_e by 1V, the DAC voltage reduces by exactly 1V in order to return the resonant frequency of the device to its original frequency. The solid and dashed lines show that the system responds accurately to the stimulus when the system is operated both with and without Q-control. However, as expected, the added noise with Q-enhancement will make smaller changes more difficult to detect. The

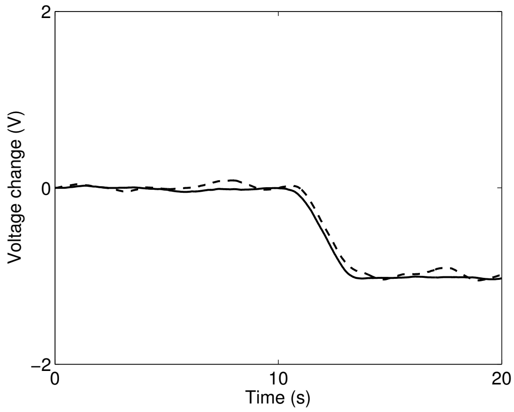

Figure 7.8: Change in tunable component of V_e in response to a 1V stimulus at the native Q (solid) and with Q-control, $\frac{\hat{Q}}{Q}$ =40 (dashed).

change in resonant frequency caused by the 1V change in stimulus voltage corresponds to a detected change in resonant frequency of 20Hz, from Equation (3.16). Due to the high SNR, it is apparent that is possible to detect a smaller change in resonant frequency than 20Hz. Figure 7.9 shows the response of the system at its native Q to a change in resonant frequency of 2Hz. The figure shows that the measured noise in the feedback voltage is approximately $50mV_{pp}$. The LSB of the digital word used to control the resonant frequency represents a change in the

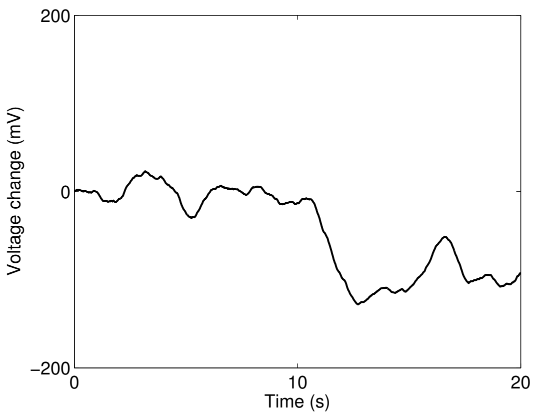

Figure 7.9: Change in tunable component of V_e in response to a 100mV stimulus.

feedback voltage of 15mV. This means that the resolution of the system is approaching the theoretical limit imposed by the hardware. From Equation (3.16), the uncertainty in frequency is approximately 1Hz, which is similar to when the phase of the system was directly measured in conjunction with Q-control, however for this technique Q-control is not required.

The detection range of the system was considered to estimate the maximum cumulative change in resonant frequency that can be tolerated. This range is determined by the amount by which the frequency control feedback voltage can be reduced in response to a change in resonant frequency. To calculate this range, Equation (3.16) was rearranged to find the change in resonant frequency when the feedback voltage is the minimum possible value. This maximum possible change in resonant frequency is given by

$$\Delta\omega_0 = \omega_0 - \sqrt{\omega_{0_1}^2 + k_e[2(V_{DCb} - V_{res})^2 + V_{AC}^2 + (V_s - V_{res})^2]}, \tag{7.7}$$

where V_{res} is the resonator bias voltage, which is -5V. Solving Equation (7.7) shows that the maximum possible change in characteristic frequency of the resonant system is 80Hz. To increase the range of the system, it is theoretically possible to use a larger initial tuning voltage (V_e), or to reduce the bias voltage of the resonator.

In this section, results show that in response to an applied stimulus voltage, the frequency tuning system responds to the change in resonant frequency by varying the tunable control voltage by the expected amount. As noise present in the tuning voltage is determined by the presence of phase noise and also because the detection resolution is not improved by increasing the rate of change of phase with respect to frequency, there is no benefit in using Q-control. Results show that the uncertainty in the detected resonant frequency is approximately 1Hz, which is similar to when the phase of the system was directly measured. The range of this system is determined by the initial value of the tuning voltage and also the bias voltage applied to the moving structure. For typical voltages, a maximum change in frequency of 80Hz can be detected without incurring any error in the measured change.

7.6 Comparison of techniques

7.6.1 Resolution

An important measure of the performance of the two techniques that have been described in this chapter is the resolution that was obtainable. When the phase of the system was measured, the best frequency resolution was achieved when quality factor control was implemented. Results show that when the effective Q is enhanced by a factor of 40, the uncertainty in any detected change in resonant frequency is approximately 1Hz. This is approximately one order of magnitude smaller than when the system operates at its natural Q. This is because the increase in the measured signal is larger than the rise in noise present when Q-control is used. Improving the detection resolution by further increasing the quality factor using Q-control is challenging, due to the complexity of controlling the feedback fraction when $\lambda \rightarrow 1$.

Alternatively, when the resonant frequency of the system is automatically returned to its original value in response to a change in system parameters, it is necessary to operate at the native Q in order to achieve the best possible detection resolution. This is because this architecture does not benefit from a large rate of change of phase with respect to resonant frequency and also due to the rise in phase noise when Q-control is used, which acts to degrade the performance of the system. Measurements show that the undesirable apparent variation in resonant frequency observed when using this approach is approximately 1Hz.

The two measurement techniques that have been implemented offer a similar detection resolution. However when the phase of the system is measured, Q-control must be used to achieve this resolution. When each system operates at the natural Q, automatically tuning the resonant frequency using a feedback voltage to change the effective spring constant of the resonator offers a better detection resolution than when the phase of the system at the natural Q is measured. The reason for this is because when the resonant frequency is automatically returned to its original frequency, the effect of this negative feedback is to reject noise and to damp the system [67, 76]. In practice, the amount of noise rejection will depend upon the bandwidth of the feedback loop, which was chosen to give a compromise between the noise and the speed of response of the system to a change in resonant frequency.

7.6.2 Range

Another difference between the two measurement architectures is the maximum cumulative change in resonant frequency that can be accurately resolved. When the phase of the system is monitored, the maximum change in resonance that can be tolerated is 15Hz. However, this is an approximate value which overestimates the tolerance range. In contrast, the maximum allowable change in resonance when the resonant frequency of the system is automatically returned to its original value is 80Hz. This range is determined by the magnitude of the initial frequency tuning voltage (V_e) relative to the bias voltage applied to the moving resonator structure. As the initial value for V_e of 4V is arbitrary, it is possible to increase the range of the system further by increasing V_e, without affecting any other system parameters. Furthermore, the change in resonant frequency determined using this technique is accurate over the entire range of the system. For these reasons, with respect to the measurement range, automatically tuning the resonant frequency is preferred over phase measurement.

7.6.3 Hardware

Both techniques for determining a change in resonant frequency when the driving frequency is fixed require the ability to measure the phase of the resonator with respect to the primary driving frequency. Consequently, the hardware required for each technique must generate a voltage proportional to the phase of the resonator relative to the primary driving force. This voltage must then be sampled into the FPGA controller and processed according to the particular measurement architecture.

When frequency tuning is used, a DAC which can be programmed by the FPGA controller to generate the feedback voltage is required. In contrast, for phase measurement no additional hardware is required in theory. Despite this, since superior detection capability is obtained when Q-control is used in conjunction with phase measurement, op-amp circuits are required to process the measured velocity signal to generate the feedback voltage for Q-control. Practical experience shows that due to the challenge of controlling the feedback fraction to maintain a stable system at a high effective Q, the most simple architecture to implement is a DAC used to generate a voltage for automatically tuning the resonant frequency of the system.

7.6.4 Recommendation

In the previous sections, advantages and disadvantages of the two detection schemes described in this chapter have been discussed. To determine which technique is most suitable for monitoring the resonant frequency when the driving frequency is fixed, the resolution, range and complexity of the hardware required to implement each technique were all considered. Taking each factor into consideration, the technique offering the best performance, flexibility and reliability is frequency tuning.

There are a number of significant reasons why automatically returning the resonant frequency to its original value is beneficial. For example, both systems that have been considered will benefit from having a high natural Q, however a high Q limits the measurement range when the phase of the system is measured. However, this is not a problem when automatic frequency tuning is implemented. Another problem that only affects the phase measurement technique is that even when the maximum possible range is not exceeded, large changes in resonant frequency will not be resolved accurately. Finally, whilst the hardware required for both techniques is similar, phase measurement requires Q-control to maximise the detection resolution. Practical experience has shown that it can be difficult to control the effective Q of the system when the feedback fraction approaches unity.

7.7 Summary

In this chapter, two methods for calculating the change in resonant frequency in response to a change in system parameters, have been described. The key feature of both techniques is that the resonator is always driven at its resonant frequency, where the phase change in the readout electronics is zero degrees. This is achieved by tuning the centre frequency of the bandpass filter used to process the measured velocity signal. The benefit of operating at a fixed frequency is that the system can not be affected by undesirable phase change that can be introduced by the readout electronics. Both techniques require the ability to measure the phase of the resonator with respect to the primary driving force. To do this, the electronic hardware for generating a digital word representing the phase of the resonator has been built.

Measurements of the phase signal show that when Q-control is implemented, noise in the signal rises by a factor of five when the quality factor is increased by a factor of 40. By taking advantage of the relatively large change in the phase signal after a change in resonant frequency when Q-control is used, an improved detection capability is achievable. An increase in detection resolution of approximately one order of magnitude was possible with this system. However, undesirable aspects of this detection scheme include the limited detection range and also the requirement for Q-control, which poses practical challenges in controlling the feedback fraction.

A more practical method for measuring a change in resonant frequency, which avoids the problems outlined above has also been implemented. For this technique, the resonance of the system is automatically returned to the system's original frequency in response to a change in the resonant frequency. The detection capability is similar to the best possible resolution when direct phase measurement was performed at high effective Q. However, analysis and practical experience suggest that frequency tuning offers the best combination of performance, reliability, range and accuracy.

Chapter 8

Conclusion

8.1 Summary

MEMS devices are mechanical structures with feature sizes ranging from a millimetre down to a micrometre in size and are typically fabricated using techniques compatible with those used in the IC industry. Because of their small size, there has recently been increasing interest in the use of MEMS technology for the detection of small quantities of various chemicals, biochemicals or relative humidity, for example. To detect such a change in the sensor's environment, a method is required to monitor any corresponding change in resonant frequency of the system. Consequently there is a desire to combine MEMS devices with measurement and control electronics in a single package to create a fully integrated and low-cost sensor.

The aim of this study was to investigate various techniques that can be used to quantify a change in the resonant frequency of a prototype MEMS device. A test structure, based upon interdigitated micro-mechanical combs, was designed for this purpose and fabricated at QinetiQ as part of the Europractice Foundry Access Program. Various architectures for detecting a change in resonant frequency have been implemented using discrete electronic components. This is because of the high-cost incurred when fabricating prototype systems using microelectronics. However, as the actuation, measurement and control electronics can all be translated into a microelectronic design, this system could eventually be integrated.

Characterisation of the prototype MEMS resonator has been described. In particular, the observed relationship between the bias voltages applied to the comb capacitances and the resonant frequency was explained. Electrostatic phenomena such as this are relatively common in MEMS systems, however when an interdigitated comb is used as the key component in the movable structure, the system is in theory immune from such effects. Despite this, analysis and simulation have shown that the drive and readout capacitances are non-ideal and cause the observed behaviour. The drive and readout capacitances in the resonator that has been manufactured are non-ideal because of the relatively short comb fingers and also due to the presence of undesirable back-to-back parallel plate capacitors in the design. The resulting relationship between the bias voltages applied to the resonator and the resonant frequency has been exploited in order to test the various measurement architectures by simulating an increase in mass of the resonant system.

A further ramification of the non-ideal drive and readout comb capacitances in the fabricated structure, is the presence of a spring-softening Duffing-like non-linearity. This is also a relatively common effect in micro-mechanical systems with electrostatic actuation and readout. When monitoring the frequency content of the velocity of a typical Duffing resonator, power is expected at primarily the first and third harmonic frequencies. However, results show that for the fabricated resonator at a large displacement, the significant frequencies are the first and second harmonic frequencies. Analysis shows that this behaviour is due to the non-ideal readout comb capacitance and not the Duffing non-linearity. This result demonstrates that analysis of the frequency content of the resonator velocity, to characterise a Duffing non-linearity, should take into account the effect of any displacement dependent terms present in the readout capacitance.

A popular technique for increasing the signal obtained from a resonant system in response to a change in resonant frequency, is to control the quality factor of the system. The most common method used to achieve this is by the generation of a feedback force which is proportional to the instantaneous velocity of the moving structure. This force directly cancels part of the force caused by air damping, resulting in an increase in the effective Q and a greater change in phase with respect to frequency. In a system designed to measure the velocity of the moving structure, Q-control can be implemented with the addition of only simple electronic amplifier circuits.

In practice, the effect of a large feedthrough signal from drive to readout ports causes undesirable behaviour when Q-control is implemented. A model for this behaviour has been developed. To significantly reduce this feedthrough signal and hence remove the undesirable behaviour, a dummy capacitance was used to generate a current which acts to cancel the instantaneous current due to capacitive feedthrough. With this compensation in place, Q-control has been used to increase the quality factor of the resonant system by two orders of magnitude when the prototype sensor is exposed to air at atmospheric pressure. However, due to the phase change present in the readout electronics, primarily associated with a bandpass filter in the feedback loop which is used to process the velocity signal, the resonant frequency of the system is still affected by the feedback force.

To solve this problem, a tunable bandpass filter was incorporated into a digital phase-locked loop system designed to monitor the characteristic frequency of the prototype resonator. The centre frequency of the filter can be tuned in order to ensure that at the resonant frequency of the particular test sample, there is no phase change in the readout electronics. The digital system was tested both with and without Q-control and due to an increase in phase noise, Q-control degraded the performance of the system. This result is in agreement with a previous study conducted by Tamayo into the noise present in systems under the action of Q-control.

When the resonant frequency of a test sample changes, the driving frequency from the digital system alters in order to locate the new resonant frequency. Results show that the system that has been built detects the small change in resonant frequency. However, even when the characteristic frequency of the bandpass filter is tuned to match the resonant frequency of the test sample, the tracking system stabilises at an incorrect frequency. This is because the rate of change of phase with respect to driving frequency in the readout electronics is similar to the rate of change of phase of the resonator velocity with respect to the primary driving force. A model for the behaviour of the tracking system has been developed which can be used to predict the intermediate frequency at which the system stabilises.

To avoid the problems caused by phase change in the readout electronics when the driving frequency alters from the tuned frequency, it is sensible to operate at a fixed frequency. Two techniques for quantifying a change in resonant frequency when the driving frequency is fixed have been assessed. The most simple technique is direct measurement of the phase of the resonator with respect to the primary driving frequency. Since this approach delivers a large signal when the quality factor is large, the existence of any benefit obtained by implementing Q-control was investigated. Experiments show that when Q-control is implemented, noise in the measured phase signal rises by less than the increase in signal. An overall improvement in SNR of approximately one order of magnitude was obtained. However, a number of factors reduce the appeal of this measurement technique. In particular, the measurement range of this approach reduces with increasing effective Q and at large changes of resonant frequency, the calculated change in frequency is overestimated.

A new technique for determining the magnitude of a change in resonant frequency when the driving frequency of the system is fixed has been developed. To do this, the driving frequency of the digital is system is set to the resonant frequency of the particular test sample using the PLL tracking system. The algorithm in the FPGA controller subsequently enters a frequency tuning state. In this mode of operation, a feedback voltage is used to ensure that the resonant frequency of the system remains constant. In response to a decrease in resonant frequency, the FPGA is programmed to respond to the observed phase signal by decreasing the feedback voltage, which returns the resonant frequency to the original value. The change in the feedback voltage is then used to calculate the change in characteristic frequency that occurred. The stability of this system is determined by the amount of noise present in the measured phase signal and since this rises with Q-control and also because the system does benefit from the large phase signal observed when the quality factor is high, Q-enhancement does not offer any benefit. However, the technique that has been developed will benefit from operating in conjunction with a resonant system with a high natural quality factor. This is because noise in the measured phase will be low when the natural Q is high, reducing noise in the feedback voltage which is used to monitor the system.

Other than optimising the design of the movable structure to naturally increase the Q of the system, the only other method for improving the detection resolution is by increasing the time constant of the filter controlling the feedback voltage, or the filter used to process data from the FPGA. The effect of using a filter with a lower characteristic frequency is to further reject noise and hence reduce uncertainty in the detected resonant frequency. The necessary trade-off required to implement this is in the speed of the response of the system to any change in resonant frequency. In practice, the bandwidth that can be tolerated is determined by the specifications of the particular application.

The system has been built using only discrete electronic components and no additional test and measurement equipment is required. The significance of this is that the proposed architecture could be translated into a microelectronic design and optimised for compatibility with a small sensor to create a fully integrated mass detector. Since the mass of the resonator used in the prototype system is relatively large (4μg), the prototype system would be capable of detecting a change in mass of 1ng if the resonator were to be functionalised. However, the results from this prototype system are sufficiently promising to suggest that the electronics should be integrated into a single substrate that can be combined in a single package with a MEMS resonator. In addition to reducing size and cost, another advantage of integrating the electronics into a single substrate will be that it creates an opportunity to employ a fully integrated transimpedance amplifier with a gain of over $1\text{G}\Omega$ [77], instead of the discrete transimpedance amplifier. The resulting increase of three orders of magnitude in the transimpedance would allow the system to be used with a resonator that is significantly smaller than the one used in the prototype system. Therefore the resulting system would be significantly more sensitive to changes in mass than the prototype.

8.2 Future work

8.2.1 FPGA controller algorithm

A fully integrated system designed for use as a mass sensor should ideally function without the requirement for user input, calibration or interpretation of the output signal. In chapter 7, a method for calculating the magnitude of a change in resonant frequency by automatically tuning the system using a feedback voltage has been described. In the system that has been implemented, the algorithm programmed into the FPGA controller does not meet all of the above criteria. In this section, areas of further work that are required in order to meet these specifications are discussed.

A key component in the system that has been developed is a switched capacitor bandpass filter which is used to recover the velocity signal from background noise. The clock signal used to tune the characteristic frequency of this filter is a fixed frequency. Furthermore, the frequency of this clock signal is a function of the particular resonant frequency of the resonator under test. Consequently, to tune the characteristic frequency of the filter requires prior knowledge of the resonant frequency. Currently this is achieved by initially characterising the resonator to identify its resonant frequency. However, this is an expensive process step to implement during mass production of a full sensor. To avoid this undesirable step, an algorithm must eventually be implemented in the FPGA controller to automatically characterise a previously untested resonator.

When the system that has been developed is operating, to detect a change in resonant frequency the controller monitors the feedback voltage which is used to vary the effective spring constant of the resonant system. Currently, this voltage is digitised and a shift in resonant frequency is calculated using Equation (3.16) to map an observed change in feedback voltage to a change in resonant frequency. Once again, characterisation of the resonator is initially required to identify the mechanical resonant frequency and hence solve Equation (3.16). However, once an algorithm has been developed for automatically characterising the resonant system, the FPGA controller will be able to perform this calculation.

Another problem with the system that has been implemented is that data from the FPGA controller is streamed to MATLAB where it is filtered. However, in a low-cost sensor application, it will not be possible to use MATLAB to process data. In the future, further filtering can be performed in the FPGA controller to avoid the requirement for post-processing using a PC. The control algorithm could then be modified to output a digital word or an analogue voltage representing the instantaneous percentage change in resonant frequency, or mass, of the sensor. Alternatively, the percentage change in resonant frequency could be compared to a predefined threshold and a logic output generated. In this way, the requirement for a user input or interpretation of the output signal from the system could be eliminated.

8.2.2 Further applications of Q-control

In this investigation, unexpected characteristics of the prototype test resonator have been observed and explained. The cause of these phenomena has been identified as non-ideal drive and readout comb capacitances. One of the effects of these non-ideal comb capacitances is the existence of a relationship between the bias voltages applied to the comb capacitances and the resulting resonant frequency of the resonators. This relationship is exploitable and the ability to control the effective spring constant was used in order to simulate an increase in mass of the structure.

The other key unexpected feature of the behaviour of the prototype resonator is the presence of a spring-softening Duffing-like non-linearity when the structure is excited with a large amplitude. Experiments and simulation showed that the presence of a discontinuity in both the velocity and phase responses could be controlled by varying the vacuum level to control the natural Q of the resonant system. It is therefore possible, in theory, to use Q-enhancement to control the presence of this discontinuity in the response of the system. Further, in a system designed with a mechanical spring-hardening, Q-control could be used in the same way. Consequently, future work will investigate the role of Q-enhanced non-linear resonant systems in the implementation of integrated low-cost mass sensors.

Appendix A

Quality factor estimate

Initially the Q due to slide film damping is considered as this is expected to be the dominant source of damping for a laterally oscillating microstructure [52]. An equation describing the quality factor of a resonant system in terms of the dissipation of energy is [78],

$$Q = 2\pi \times \frac{\text{Energy in system at start of cycle}}{\text{Energy lost during cycle}}, \tag{A.1}$$

hence

$$Q = \frac{2\pi E_s}{A_d E_d}, \tag{A.2}$$

where E_s is the stored energy, E_d is energy lost per unit area per cycle of oscillation and A_d is the area of the damping plate. An expression for the stored energy is

$$E_s = \frac{1}{2}kX^2 = \frac{\dot{X}^2\sqrt{mk}}{2\omega}. \tag{A.3}$$

When a laterally moving oscillator moves in the vicinity of a stationary plate, the energy lost per cycle due to slide film damping is given by

$$E_d = \frac{\pi \dot{X}^2 \mu_0}{\omega g_d}, \tag{A.4}$$

where μ_0 is the dynamic viscosity and g_d is the damping gap. However, when the oscillator moves near an open surface, E_d is then

$$E_d = \frac{\pi \dot{X}^2 \mu_0}{\omega \delta}, \tag{A.5}$$

where $\delta = \sqrt{2\nu_0/\omega}$ is the distance over which the velocity has decreased to $\frac{1}{e}$ of its original value and ν_0 is the kinematic viscosity.

Slide film damping in the vicinity of a stationary plate on the bottom and the sides of the resonator and also the sides of the comb fingers. Slide film damping near an open surface occurs on the top of the resonator, hence

$$E_{d-bottom} = \frac{\pi \dot{X}^2 \mu_0}{\omega g_{d1}}, \tag{A.6}$$

$$E_{d-side} = \frac{\pi \dot{X}^2 \mu_0}{\omega g_{d2}}, \tag{A.7}$$

$$E_{d-comb} = \frac{\pi \dot{X}^2 \mu_0}{\omega g_{d3}}, \tag{A.8}$$

$$E_{d-top} = \frac{\pi \dot{X}^2 \mu_0}{\omega \delta}. \tag{A.9}$$

The quality factor due to each of these damping mechanisms is then

$$Q_{bottom} = \frac{\sqrt{mk}\, g_{d1}}{\mu_0 A_{d-bottom}}, \tag{A.10}$$

$$Q_{side} = \frac{\sqrt{mk}\, g_{d2}}{\mu_0 A_{d-side}}, \tag{A.11}$$

$$Q_{comb} = \frac{\sqrt{mk}\, g_{d3}}{\mu_0 A_{d-comb}}, \tag{A.12}$$

$$Q_{top} = \frac{\sqrt{mk}\, \delta}{\mu_0 A_{d-top}}. \tag{A.13}$$

Table A.1: Parameter values to estimate the resonator quality factor due to slide film damping at atmospheric pressure.

Parameter	Value	Units
$A_{d-top,bottom}$	7×10^{-8}	m^2
A_{d-side}	2×10^{-8}	m^2
A_{d-comb}	8×10^{-8}	m^2
g_{d1}	2	$\mu\mathrm{m}$
g_{d2}	5	$\mu\mathrm{m}$
g_{d3}	3	$\mu\mathrm{m}$
μ_0	2×10^{-5}	$\mathrm{kgm^{-1}s^{-1}}$
ν_0	1.6×10^{-5}	$\mathrm{kgm^{-1}s^{-1}}$
m	3.6	$\mu\mathrm{g}$
k	25.4	$\mathrm{Nm^{-1}}$

The overall quality factor due to slide film damping is then

$$\frac{1}{Q_{slide}} = \frac{1}{Q_{bottom}} + \frac{1}{Q_{side}} + \frac{1}{Q_{comb}} + \frac{1}{Q_{top}}, \tag{A.14}$$

$$= \frac{\mu_0}{\sqrt{mk}} \left(\frac{A_{d-bottom}}{g_{d1}} + \frac{A_{d-side}}{g_{d2}} + \frac{A_{d-comb}}{g_{d3}} + \frac{A_{d-top}}{\delta} \right). \tag{A.15}$$

To evaluate the quality factor due to slide film damping, the relevant parameters are given in Table A.1, giving Q_{slide} ~200.

To investigate if squeeze film damping is significant in this design, the quality factor due to squeeze film damping is considered. The damping constant due to squeeze film damping in the absence of a substrate is

$$c = \frac{\mu_0 w t_h^3}{g_d^3}, \tag{A.16}$$

where w is the width of the structure forming the squeeze film damper [53]. When the presence of the substrate is taken into account, the damping constant is related to the gap between the moving structure and the substrate. When the gap is small, the damping level is four times greater than when there is no substrate present, however for this design (with a finite gap under the moving structure) the factor is approximated to be three.

There are two significant squeeze film dampers in the design, due to the finger ends and the opposing comb recesses, and also the small gap between the backs of opposing comb arms. The expression above models the squeeze film damper between the backs of opposing comb arms, however care is required when considering the damper due to the end of a comb finger. When $w = t_h$, the cross section is a square and gas escapes from all sides equally [54]. The damping constant in this case is

$$c = 0.422\frac{\mu_0 t_h^4}{g_d^3}. \tag{A.17}$$

However, in this design for the comb fingers $w < t_h$, suggesting that gas preferentially escapes from the side of the squeeze film damper and not the top, however the gap at the side is also small (as the damper is formed in a comb recess) restricting this effect and forcing gas out of the top. Consequently, to model damping due to a comb finger, Equation (A.16) is used with a compensation factor of 0.5 to take into account the small lateral distance ($w < t_h$). Hence

$$c_{fingers} = \frac{3}{2} \times n_f \times \frac{\mu_0 w_{finger} t_h^3}{g_{d4}^3}, \tag{A.18}$$

$$c_{backs} = 3 \times n_b \times \frac{\mu_0 w_{back} t_h^3}{g_{d5}^3}, \tag{A.19}$$

where n_b is the number of opposing comb arms forming squeeze film dampers. The overall quality factor is then

$$\frac{1}{Q_{squeeze}} = \frac{1}{Q_{fingers}} + \frac{1}{Q_{backs}}, \tag{A.20}$$

hence from Equation (1.3)

$$\frac{1}{Q_{squeeze}} = \frac{1}{\sqrt{mk}}(c_{fingers} + c_{backs}). \tag{A.21}$$

To evaluate the quality factor, parameters are given in Table A.2, giving $Q_{squeeze}$ ~10.

Table A.2: Parameter values to estimate the resonator quality factor due to squeeze film damping at atmospheric pressure.

Parameter	Value	Units
w_{finger}	5	μm
w_{back}	200	μm
t_h	20	μm
g_{d4}	5	μm
g_{d5}	5	μm
μ_0	2×10^{-5}	$\mathrm{kgm^{-1}s^{-1}}$
m	3.6	μg
k	25.4	$\mathrm{Nm^{-1}}$

Appendix B

Frequency spectrum of current

Full analysis of the frequency content of the current delivered from a readout port (when $\frac{dC}{dx}$ contains displacement-dependent terms), for a Duffing-like oscillator with first and third harmonic frequencies in the velocity and displacement,

$$x = X\sin(\omega t) + X_3\sin(3\omega t). \tag{B.1}$$

The current generated at the readout port is described by Equation (3.21),

$$i(t) = V_s\dot{x}\left(C_0' + C_1'x + C_3'x^3\right).$$

Hence

$$\begin{aligned} i(t) \quad = \quad & V_s\left(\omega X\cos(\omega t) + 3\omega X_3\cos(3\omega t)\right)\times \\ & [C_0' + C_1'(X\sin(\omega t) + X_3\sin(3\omega t)) + \\ & C_3'(X^3\sin^3(\omega t) + 3XX_3^2\sin(\omega t)\sin^2(3\omega t) + \\ & 3X^2X_3\sin^2(\omega t)\sin(3\omega t) + X_3^3\sin^3(3\omega t))]. \end{aligned} \tag{B.2}$$

Multiplying terms gives

$$\begin{aligned}
i(t) \;=\;& V_s\omega C_0'(X\cos(\omega t) + 3X_3\cos(3\omega t)) + \\
& V_s\omega C_1'[X^2\sin(\omega t)\cos(\omega t) + XX_3\sin(3\omega t)\cos(\omega t) + \\
& 3XX_3\sin(\omega t)\cos(3\omega t) + 3X_3^2\sin(3\omega t)\cos(3\omega t)] + \\
& V_s\omega C_3'[X^4\sin^3(\omega t)\cos(\omega t) + 3X^2X_3^2\sin(\omega t)\cos(\omega t)\sin^2(3\omega t) + \\
& 3X^3X_3\sin^2(\omega t)\cos(\omega t)\sin(3\omega t) + XX_3^3\sin^3(3\omega t)\cos(\omega t) + \\
& 3X^3X_3\sin^3(\omega t)\cos(3\omega t) + 9XX_3^3\sin(\omega t)\sin^2(3\omega t)\cos(3\omega t) + \\
& 9X^2X_3^2\sin^2(\omega t)\sin(3\omega t)\cos(3\omega t) + 3X_3^4\sin^3(3\omega t)\cos(3\omega t)].
\end{aligned} \tag{B.3}$$

Simplifying and collecting terms ($\leq 4\omega$) gives

$$\begin{aligned}
i(t) \;=\;& V_s\omega C_0'X\cos(\omega t) + \\
& V_s\omega C_0'3X_3\cos(3\omega t) + \\
& V_s\omega\sin(2\omega t)\left[(X^2 - 2XX_3)\frac{C_1'}{2} + (X^4 + 3X^2X_3^2 + 3X^3X_3 - 3XX_3^3)\frac{C_3'}{4}\right] + \\
& V_s\omega\sin(4\omega t)\left[2XX_3C_1' + (-X^4 - 6X^2X_3^2 + 6X^3X_3 + 12XX_3^3)\frac{C_3'}{8}\right].
\end{aligned} \tag{B.4}$$

Appendix C

MATLAB code

Transient simulations were performed using the `ode45` solver, which integrates a system of differential equations $y' = f(t, y)$. A model file returns a column vector corresponding to $f(t, y)$. The simulation control file (`Q5_cubic_main.m`) and the corresponding model file (`Q5_cubic_fucntion.m`) are given below.

```
%Simulation of non-linear dC/dx terms for comb driven microresonator
%Ross Turnbull, 08/01/10, Oxford University
%Q5_cubic_main.m

function Q5_cubic_main(Avalue)
close all;

%Polynomial describing dC/dx
if Avalue==1;                           %Extracted A value
    A=16.2e-9;
    B=10.1e-3;
    C=-91.2;
    D=1.91e9;
elseif Avalue==0;
    A=14.7e-9;                          %Simulated A value
    B=10.1e-3;
    C=-91.2;
    D=1.91e9;
end;
m=4e-9;
f0=16787;

%Define test conditions for resonator testing
Vs=8;                                   %Differential readout voltage
R=1e6;                                  %Current to voltage conversion
INAGAIN=10;                             %AD620 gain = 10
f=16350:5:16850;                        %Sweep range (Hz)
pressure1=1.3e1;
pressure2=1.7e2;
Vac1=4;                                 %Drive voltage at pressure 1
```

```
Vac2=8;
Q1=4.3e3*pressure1^(-0.6);              %Q-factor from pressure
Q2=4.3e3*pressure2^(-0.6);

%Set up simulation parameters for ode45 solver
tstep=1e-6;
fs=1/tstep;
tstop=200e-3;
TSPAN=0:tstep:tstop;
Y0=zeros(4,1);
[¬,points]=size(f);
pars=[Vs,Vac1,Vac2,Q1,Q2,f0,m,A,B,C,D];
SteadyStateV1=zeros(points,1);          %Preallocation for speed
SteadyStateV2=zeros(points,1);
Phase1=zeros(points,1);
Phase2=zeros(points,1);

%For fft phase extraction
N=tstop/tstep;
f_fft=(0:N)*fs/N;                       %Frequency bins
ind=find(f_fft>f(1),1,'first')-1;       %Index of first frequency bin

%Run simulation loop
for i=1:points
    f_cur=f(i);
    fprintf('Current frequency simulating is :%d\n',f_cur);
    [TOUT,YOUT]=ode45('Q5_cubic_function',TSPAN,Y0,[],f_cur,pars);
    bottom=round(.9*tstop/tstep);       %To eliminate transient effects
    top=round(tstop/tstep);
    x1=YOUT(:,1);
    xdot1=YOUT(:,2);
    x2=YOUT(:,3);
    xdot2=YOUT(:,4);
    Vo1a=INAGAIN*R*Vs*xdot1.*(A +B*x1 +C*x1.^2 +D*x1.^3);
    Vo1b=INAGAIN*R*Vs*-xdot1.*(A -B*x1 +C*x1.^2 -D*x1.^3);
    Vina1=Vo1a-Vo1b;
    Vo2a=INAGAIN*R*Vs*xdot2.*(A +B*x2 +C*x2.^2 +D*x2.^3);
    Vo2b=INAGAIN*R*Vs*-xdot2.*(A -B*x2 +C*x2.^2 -D*x2.^3);
    Vina2=Vo2a-Vo2b;
    SteadyStateV1(i,1)=max(abs(Vina1(bottom:top,1)));
    SteadyStateV2(i,1)=max(abs(Vina2(bottom:top,1)));
    Phaseprofile1=unwrap(angle(fft(Vina1)))*180/pi;
    Phaseprofile2=unwrap(angle(fft(Vina2)))*180/pi;
    Phase1(i,1)=Phaseprofile1(ind+i-1);
    Phase2(i,1)=Phaseprofile2(ind+i-1);
    if f_cur==16605                     %Effective resonance
        Vinatrans1=Vo1a;
        Vinatrans2=Vo2a;
    end
end

%Save data
data_array(:,1)=f;
data_array(:,2)=SteadyStateV1;
data_array(:,3)=SteadyStateV2;
data_array2(:,1)=TOUT;
data_array2(:,2)=Vinatrans1;
data_array2(:,3)=Vinatrans2;
data_array3(:,1)=f;
data_array3(:,2)=Phase1;
```

```
data_array3(:,3)=Phase2;
if Avalue==1;
    csvwrite('Q5_f_spectrum.csv',data_array);
    csvwrite('Q5_transient.csv',data_array2);
    csvwrite('Q5_phase_spectrum.csv',data_array3);
elseif Avalue==0;
    csvwrite('Q5_f_spectrum_SIMA.csv',data_array);
    csvwrite('Q5_transient_SIMA.csv',data_array2);
    csvwrite('Q5_phase_spectrum_SIMA.csv',data_array3);
end;
```

```
%Simulation of non-linear dC/dx terms for comb driven microresonator
%Ross Turnbull, 08/01/10, Oxford University
%Q5_cubic_function.m

function dy = Q5_cubic_function(t,y,¬,f_cur,pars)

%Extract parameters
Vs=pars(1);
Vac1=pars(2);
Vac2=pars(3);
Q1=pars(4);
Q2=pars(5);
f0=pars(6);
m=pars(7);
A=pars(8);
B=pars(9);
C=pars(10);
D=pars(11);

w0=f0*2*pi;

%Define driving forces
F1=0.5*(Vac1*cos(pi*f_cur*t))^2*(A +B*y(1) +C*y(1)^2 +D*y(1)^3);
F2=0.5*(Vac2*cos(pi*f_cur*t))^2*(A +B*y(3) +C*y(3)^2 +D*y(3)^3);

%Equations of motion (differential readout)
dy(1,1)=y(2);
dy(2,1)=-w0^2*y(1) -(w0/Q1)*y(2) +F1/m +Vs^2*(B*y(1) +D*y(1)^3)/m;
dy(3,1)=y(4);
dy(4,1)=-w0^2*y(3) -(w0/Q2)*y(4) +F2/m +Vs^2*(B*y(3) +D*y(3)^3)/m;
```

Bibliography

[1] C. Anthony, R. Turnbull, M. Ward, and S. Collins. A mems resonator with linear differential drive. *Proceedings of the 19th Micro-Mechanics Europe Workshop (MME 2008)*, 2008.

[2] R. Turnbull, M. Ward, S. Collins, and C. Anthony. A simple technique to increase the quality factor of micro-mechanical resonators. *Micro- and Nanotechnology Sensors, Systems, and Applications*, 7318(1):73181G, 2009.

[3] C. Anthony, R. Turnbull, X. Wei, M. Ward, and S. Collins. Fabrication and quality factor control of a microelectromechanical system resonator with linear differential drive. *IET Science, Measurement & Technology*, pages 206–213, 2010.

[4] C. Deng, R. Turnbull, C. Anthony, M. Ward, and S. Collins. A non-linear resonator for sensing applications. *Proceedings of Eurosensors XXIV*, 2010.

[5] B. Choubey, C. Anthony, N. Saad, M. Ward, R. Turnbull, and S. Collins. Characterization of coupled micro/nano resonators using inverse eigenvalue analysis. *Applied Physics Letters*, 2010.

[6] B. Choubey, M. Ward, C. Anthony, R. Turnbull, and S. Collins. On inverse eigenvalue analysis and characterisation of coupled micro/nano resonators. *The 9th Annual IEEE Conference on Sensors*, 2010.

[7] R. Turnbull, M. Ward, C. Anthony, and S. Collins. Detection of changes in the resonant frequency of a mems resonator using a dds-based system. *IET Science, Measurement & Technology*, 2010.

[8] N. Saad, X. Wei, C. Anthony, H. Ostadi, R. Al-Dadah, and M. Ward. Impact of manufacturing variation on the performance of coupled micro resonator array for mass detection sensor. *Procedia Chemistry*, 1(1):831–834, 2009.

[9] X. Wei, M. Ward, C. Anthony, and D. Lowe. A preliminary study of a nonlinear micro vibro-impact system impact. *35th International Conference on Micro & Nano Engineering (MNE)*, 2010.

[10] R. Feynman. There's plenty of room at the bottom. *Journal of Microelectromechanical Systems*, 1(1):60–66, 1992.

[11] M. Gad el Hak. *MEMS Design and Fabrication*. CRC Press, 2006.

[12] M. Ventra, S. Evoy, and J. Heflin. *Introduction to Nanoscale Science and Technology*. Kluwer Academic Publishers, 2004.

[13] H. Nathanson, W. Newell, R. Wickstrom, and J. Davis Jr. The resonant gate transistor. *IEEE Transactions on Electron Deives*, ed-14(3):117–133, 1967.

[14] R. Muller. Mems: Quo vadis in century xxi? *Microelectronic Engineering*, 53(1–4):47–54, 2000.

[15] J. Bryzek. Impact on mems technology on society. *Sensors and Actuators A: Physical*, 56(1–2):1–9, 1996.

[16] J. Bryzek, K. Peterson, and W. McCulley. Micromachines on the march. *IEEE Spectrum*, 31:20–31, 1994.

[17] J. Judy. Microelectromechanical systems (mems): fabrication, design and applications. *Smart Materials and Structures*, 10:1115–1134, 2001.

[18] E. Wachter and T. Thundat. Micromechanical sensors for chemical and physical measurements. *Review of Scientific Instruments*, 66(6):3662–3667, 1995.

[19] T. Burg, M. Godin, S. Knudsen, W. Shen, G. Carlson, J. Foster, K. Babcock, and S. Manalis. Weighing of biomolecules, single cells and single nanoparticles in fluid. *Nature*, 446:1066–1069, 2007.

[20] T. Burg, A. Mirza, N. Milovic, C. Tsau, G. Popescu, J. Foster, and S. Manalis. Vacuum-packaged suspended microchannel resonant mass sensor for biomolecular detection. *Journal of Microelectromechanical Systems*, 15(6):1466–1476, 2006.

[21] A. French. *Vibrations and Waves*. Chapman and Hall, 1971.

[22] A. McEwan and S. Collins. Direct digital-frequency synthesis by analogue interpolation. *IEEE Transactions on Circuits and Systems II: Express Briefs*, 53(11), 2006.

[23] A. McEwan and S. Collins. Analogue interpolation based direct frequency synthesis. *IEEE International Symposium on Circuits and Systems*, 2003.

[24] V. Kroupa. *Direct Digital Frequency Synthesizers*. IEEE Press, 1998.

[25] J. Comtois, M. Michalicek, and C. Barron. Fabricating micro-instruments in surface-micromachined polycrystalline silicon. *Proceedings of the 43rd International Instrumentation Symposium*, 1997.

[26] D. Niarchos. Magnetic mems: key issues and some applications. *Sensors and Actuators A: Physcial*, 109:116–173, 2003.

[27] J. Comtois and V. Bright. Applications for surface-micromachined polysilicon thermal actuators and arrays. *Sensors and Actuators A: Physcial*, 58:19–25, 1997.

[28] J. Mertz, O. Marti, and J. Mlynek. Regulation of a microcantilever response by force feedback. *Applied Physics Letters*, 62(19):2344–2346, 1993.

[29] G. Klaasse, R. Puers, and H. Tilmans. Piezoelectric versus electrostatic actuation for a capacitive rf-mems switch. *Proceedings of Semiconductor Sensor and Actuator Technology (SeSens)*, pages 631–634, 2000.

[30] F. Laermer and A. Schilp. Method of anisotropically etching silicon. U.S. Patent 5,501,893, 1996.

[31] F. Laermer, A. Schilp, K. Funk, and M. Offenberg. Bosch deep silicon etching: improving uniformity and etch rate for advanced mems applications. *Micro Electro Mechanical Systems, 1999. MEMS '99. Twelfth IEEE International Conference on*.

[32] A. Rickard and M. McNie. Characterisation and optimisation of deep dry etching for mems applications. *SPIE International Conference on 'Microelectronic & MEMS Technologies'*, 2001.

[33] M. McNie, R. Davies, N. Price, D. King, and K. Brunson. Advanced micromechanical prototyping in polysilicon and soi. *Demonstrated Micromachining Technologies for Industry (Ref. No. 2000/032), IEE Seminar on*, pages 8/1–8/4, 2000.

[34] M. McNie, D. King, C. Vizard, A. Holmes, and K. Lee. High aspect ratio micromachining (harm) technologies for microinertial devices. *Microsystem Technologies*, 6(5):184–188, 2000.

[35] D. King and M. Ward. Polysilicon micromachining and industry. *Recent Advances in Micromachining Techniques (Digest No: 1997/081), IEE Colloquium*, pages 1/1–1/2, 1997.

[36] M. Martin, C. Williams, and H. Wickramasinghe. Atomic force microscope-force mapping and profiling on a sub 100-Å scale. *Journal of Applied Physics*, 61(10):4723–4729, 1987.

[37] W-Y. Chang, P-H. Sung, C-H. Chu, C-J. Shih, and Y-C. Lin. Phase detection of the two-port fpw sensor for biosensing. *IEEE Sensors Jounal*, 8(5):501–507, 2008.

[38] M. Christen. Air and gas damping of quartz tuning forks. *Sensors and Actuators*, 4:555–564, 1983.

[39] W. Newell. Miniaturization of tuning forks. *Science*, 161:1320–1326, 1968.

[40] J. Tamayo, A. Humphris, A. Malloy, and M. Miles. Chemical sensors and biosensors in liquid enviroment based on microcantilevers with amplified quality factor. *Ultramicroscopy*, 86:167–173, 2001.

[41] J. Tamayo, A. Humphris, and M. Miles. Piconewton regime dynamic force microscopy in liquid. *Applied Physics Letters*, 77(4):582–584, 2000.

[42] J. Tamayo, M. Alvarez, and L. Lechuga. Digital tuning of the quality factor of micromechanical resonant biological detectors. *Sensors and Actuators B: Chemical*, 89(1–2):33–39, 2003.

[43] C. Nguyen and R. Howe. An integrated cmos micromechanical resonator high-q oscillator. *IEEE Journal of Solid-State Circuits*, 34(4):440–455, 1999.

[44] C. Nguyen and R. Howe. Quality factor control for micromechanical resonators. *Electron Devices Meeting, 1992. Technical Digest., International*, pages 505–508, 1992.

[45] J. Tamayo. Study of the noise of micromechanical oscillators under quality factor enhancement via driving force control. *Journal of Applied Physics*, 97:044903–044903–10, 2005.

[46] W. Tang, T. Nguyen, M. Judy, and R. Howe. Electrostatic-comb drive of lateral polysilicon resonators. *Sensors and Actuators A: Physical*, 21:328–331, 1990.

[47] W. Tang, T. Nguyen, and R. Howe. Laterally driven polysilicon resonant microstructures. *Sensors and Actuators*, 20:53–59, 1989.

[48] F. Ghavanini and H. Rödjegård. An easy-to-implement method for evaluation of capacitive resonant sensors. *Journal of Micromechanics and Microengineering*, 16:S156–S160, 2006.

[49] L. Baxter. *Capacitive Sensors*. IEEE Press, 1997.

[50] X. Zhang and W. Tang. Viscous air damping in laterally driven microresonators. *Micro Electro Mechanical Systems, 1994, MEMS '94, Proceedings, IEEE Workshop on*, pages 199–204, 1994.

[51] P. Bruschi, A. Nannini, and F. Pieri. Electrical measurements of the quality factor of microresonators and its dependence on the pressure. *Sensors and Actuators A: Physical*, 114:21–29, 2004.

[52] Y-H. Cho, A. Pisano, and R. Howe. Viscous damping model for laterally oscillating microstructures. *Journal of Microelectromechanical Systems*, 3(2):81–87, 1994.

[53] A. Berny. Substrate effects in squeeze film damping of lateral parallel-plate sensing mems structures. http://robotics.eecs.berkeley.edu/˜pister/245/project/Berny.pdf.

[54] S. Vemuri. Behavioral modeling of viscous damping in mems. Master's thesis, Carnegie Mellon University, 2000.

[55] C-M. Ho and Y-C. Tai. Micro-electro-mechanical-systems (mems) and fluid flows. *Annual Review of Fluid Mechanics*, 30:579–612, 1998.

[56] W-M. Zhang and G. Meng. Nonlinear dynamic analysis of electrostatically actuated resonant mems sensors under parametric excitation. *IEEE Sensors Jounal*, 7(3):370–380, 2007.

[57] S. De and N. Aluru. Full-lagrangian schemes for dynamic analysis of electrostatic mems. *Journal of Microelectromechanical Systems*, 13(5):737–758, 2004.

[58] J. Rhoads, S. Shaw, and K. Turner. Nonlinear dynamics and its applications in micro- and nanoresonators. *Proceedings of DSCC2008 ASME Dynamic Systems and Control Conference*, 2008.

[59] J. Zhao, G. Bridges, and D. Thomson. Direct evidence of "spring softening" nonlinearity in micromachined mechanical resonator using optical beam deflection technique. *Journal of Vacuum Science and Technology A*, 24(3):732–736, 2006.

[60] H-M. Jeong and S. Ha. Dynamic analysis of a resonant comb-drive micro-actuator in linear and nonlinear regions. *Sensors and Actuators A: Physical*, 125:59–68, 2005.

[61] L. Shao, M. Palaniapan, and W. Tan. The nonlinearity cancellation phenomenon in micromechanical resonators. *Journal of Micromechanics and Microengineering*, 18, 2008.

[62] M. Agarwal, S. Chandorkar, R. Candler, B. Kim, M. Hopcroft, R. Melamud, C. Jha, T. Kenny, and B. Murmann. Optimal drive condition for nonlinearity reduction in electrostatic microresonators. *Applied Physics Letters*, 89, 2006.

[63] P. Holmes and D. Rand. The bifurcations of duffing's equation: An application of catastrophe theory. *Journal of Sound and Vibration*, 44(2):237–253, 1976.

[64] S. Timoshenko, D. H. Young, and W. Weaver. *Vibration problems in engineering*. Wiley, 1974.

[65] W. Thompson. *Theory of vibration with applications*. Prentice-Hall, 1981.

[66] J. Thomsen. *Vibrations and stability*. McGraw-Hill, 1997.

[67] P. Horowitz and W. Hill. *The Art of Electonics*. Cambridge University Press, 1980.

[68] W-K. Chen. *The circuits and filters handbook*. CRC Press, 1995.

[69] J. Lee, Y. Zhu, and A. Seshia. A bulk acoustic mode single-crystal silicon microresonator with a high-quality factor. *Journal of Micromechanics and Microengineering*, 18(6):064001 (6pp), 2008.

[70] J. Lee and A. Seshia. Parasitic feedthrough cancellation techniques for enhanced electrical characterization of electrostatic microresonators. *Sensors and Actuators A: Physical*, 156(1):36–42, 2009.

[71] R. Best. *Phase-locked loops : design, simulation, and applications*. McGraw-Hill, 1997.

[72] K. Schoepf. Tcmo^{TM}: A versatile mems oscillator timing platform. *41st Annual Precise Time and Time Interval (PTTI) Meeting*, 2009.

[73] T. Lee. *The design of CMOS radio-frequency integrated cicuits*. Cambridge University Press, 2004.

[74] L. Oliveira, J. Fernandes, I. Filanovsky, C. Verhoeven, and M. Silva. *Analysis and design of quadrature oscillators*. Springer, 2008.

[75] B. Razavi. *RF microelectronics*. Prentice-Hall, 1998.

[76] R. Dorf and R. Bishop. *Modern Control Systems*. Prentice-Hall, 2008.

[77] G. Cui, H. Yang, and S. Xia. A highly stable cmos transimpedance amplifier for compact integration. *Solid-State and Integrated Circuit Technology. ICSICT '06. 8th International Conference on*, 2006.

[78] W. Gough, J. Richards, and R. Williams. *Vibrations and Waves*. Ellis Horwood Limited, 1983.